# Oncology and Translational Medicine

Volume 3 • Number 2 • April 2017

**Breast ultrasound elastography**
Xinwu Cui, Youbin Deng 47

**Ultrasonographic features of breast ductal carcinoma in situ**
Liping Wang, Youbin Deng, Xinwu Cui 49

**Quantitative differential diagnosis of breast tumors using shear wave velocity and different probe orientations**
Yuan Huang, Youbin Deng, Liping Wang, Xinwu Cui 52

**Ultrasound-guided percutaneous microwave ablation for small liver cancers adjacent to large vessels: long-term outcomes and strategies**
Ruobing Liu, Kaiyan Li, Hongchang Luo, Wei Zhang, Tingting Zhang, Meng Gao, Wenhui Zha, Xinwu Cui, Youbin Deng 57

**Selective partial salivary glands sparing during intensity-modulated radiation therapy for nasopharyngeal carcinoma**
Guangjin Yuan, Qianwen Li (Co-first author), Shixian Chen, Chengwei Zheng, Jiang Tang, Jiang Hu, Ximing Xu 65

Oncology and Translational Medicine Volume 3 • Number 2 • April 2017 pp 47-90

ISSN 2095-9621
CN 42-1865/R

# Oncology and Translational Medicine

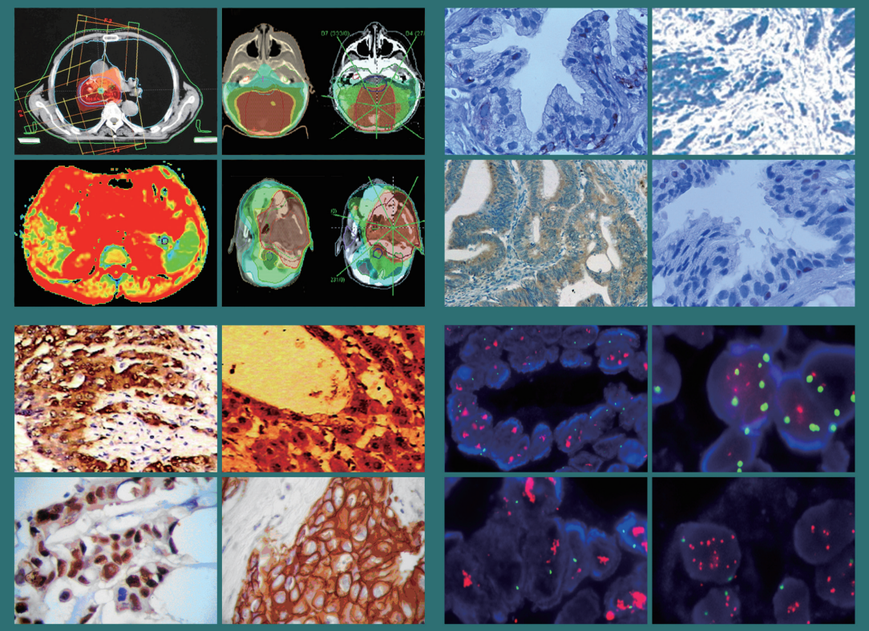



邮发代号：38-121
ISSN 2095-9621

GENERAL INFORMATION
≫otm.tjh.com.cn

Volume 3
Number 2
April 2017

# Oncology and Translational Medicine

**Oncology and Translational Medicine**
*April 2017 Volume 3 Number 2*

## Contents

Breast ultrasound elastography
*Xinwu Cui, Youbin Deng 47*

Ultrasonographic features of breast ductal carcinoma in situ
*Liping Wang, Youbin Deng, Xinwu Cui 49*

Quantitative differential diagnosis of breast tumors using shear wave velocity and different probe orientations
*Yuan Huang, Youbin Deng, Liping Wang, Xinwu Cui 52*

Ultrasound-guided percutaneous microwave ablation for small liver cancers adjacent to large vessels: long-term outcomes and strategies
*Ruobing Liu, Kaiyan Li, Hongchang Luo, Wei Zhang, Tingting Zhang, Meng Gao, Wenhui Zha, Xinwu Cui, Youbin Deng 57*

Selective partial salivary glands sparing during intensity-modulated radiation therapy for nasopharyngeal carcinoma
*Guangjin Yuan, Qianwen Li (Co-first author), Shixian Chen, Chengwei Zheng, Jiang Tang, Jiang Hu, Ximing Xu 65*

BRAF V600E/TERT promoter mutations and NIS/TSHR expression in differentiated thyroid carcinoma and their clinical significance
*Xiaoting Ru, Qinjiang Liu, Haihong Zhou, Rong Yang, Lie Bao 71*

Comparison of the effects of two types of multileaf collimators on tumor control probability in radiotherapy for breast cancer after conservative surgery based on the EUD model
*Fuli Zhang, Yadi Wang, Weidong Xu, Huayong Jiang, Junmao Gao, Qingzhi Liu, Na Lu, Diandian Chen, Bo Yao, Jun Hou, Heliang He, Jianping Chen 77*

Differential expression of nucleolin in colon adenoma and adenocarcinoma
*Guozhao Meng, Junlei Yi, Ming Xie 82*

Epidermal growth factor enhances chemosensitivity of colon cancer by inducing cancer stem cells to enter the cell cycle
*You Zou, Xiaolan Li, Deding Tao, Junbo Hu, Jianping Gong 86*

Oncology and Translational Medicine
DOI 10.1007/s10330-017-0220-0
April 2017, Vol. 3, No. 2, P47–P48

EDITORIAL

# Breast ultrasound elastography

**Xinwu Cui, Youbin Deng (✉)**

Department of Medical Ultrasound, Tongji Hospital, Tongji Medical College, Huazhong University of Science and Technology, Wuhan 430030, China

**Youbin Deng** Professor of Medical Ultrasound, Doctoral Supervisor, Director of the Department of Medical Ultrasound, Tongji Hospital, Tongji Medical College of HUST, China. He obtained his bachelor degree of medicine in 1983 and Master degree of Medicine in 1986 from Tongji Medical University. He obtained PhD in 1996 from Kanazawa Medical University in Japan. Dr. Deng worked as a research fellow in The Second Department of Internal Medicine in University of Tokyo from April 1988 to March 1989, in UCSD Medical Center from August 1991 to May 1992 and in Kanazawa Medical University from August 1993 to March 1998. He served as member of standing committee of Medical Ultrasound Society of Chinese Medical Association beginning in 2005 until now, Chairman of Medical Ultrasound Society of Hubei Province Medical Association from 2004 to 2009 and Chairman of Medical Ultrasound Society of Wuhan City Medical Association from 2011 to 2015. His major research interest is cardiovascular ultrasound diagnosis. He published more than 100 papers in international peer-reviewed academic journals including Circulation, J Am Coll Cardiol, Am Heart J, Am J Cardiol, Radiology and Ultrasound in Med and Biol.

Breast cancer is one of the most common malignant diseases among women worldwide. In China, the morbidity and mortality rate from breast cancer has increased significantly in recent years. Early diagnosis is crucial to ensure the best possible prognosis. Biopsy is an invasive technique and not recommended for screening. Palpation on the other hand, can detect superficial masses, but may miss small masses or masses deep beneath the skin. Mammography is the most frequently used screening method for detecting breast cancer; however, it has poor specificity, and its efficacy is limited in patients with dense breast tissue. Ultrasonography may overcome these limitations, and it has become the most important adjunct tool for breast cancer screening. It is also routinely used for guidance in breast mass biopsy.

Ultrasound elastography is the most amazing new ultrasound technique for screening breast lesions in recent years [1]. Normal breast tissue is softer than cancerous tissue, and this feature is often used to differentiate benign and malignant breast masses. According to the recently published World Federation for Ultrasound in Medicine and Biology (WFUMB) guidelines and recommendations on the clinical use of ultrasound elastography [1], elastographic techniques used in breast cancer diagnosis can be classified into three groups: strain imaging, acoustic radiation force impulse (ARFI) displacement, and shear wave speed (SWS) measurement and imaging. Strain imaging is based on the principle that hard tissue is not as easily compressed as soft tissue. Strain imaging measures the strain response of tissue to manual compression. The stiffness of the tissue is demonstrated by its strain response, which is displayed as a color map overlaying the grey scale image [2]. Cancerous tissue, which is harder than normal tissue, will show a lower strain response. Both ARFI and SWS imaging are shear wave based techniques. Shear wave travels faster through hard tissue than it does through soft tissue. New advanced ultrasound systems can measure the speed, and display it as a color map or a definite value of m/s or Kpa with Young's modulus, to reflect the tissue elasticity.

Strain elastography analyzes the tissue stiffness with both qualitative and semi-quantitative methods. Qualitative methods analyze the color pattern within a region of interest. Semi-quantitative methods include strain ratio (measuring the relative strain between two areas) and strain histograms (computing the strain values of elemental areas). Strain elastography using both qualitative and semi-quantitative methods is able to differentiate benign from malignant masses with a high sensitivity and specificity. Similar to strain elastography,

✉ Corresponding to: Youbin Deng. Email: ybdeng2007@hotmail.com

shear wave based elastography is also able to increase diagnostic confidence in the differential diagnosis of benign and malignant lesions. Moreover, ultrasound elastography is useful in re-grading benign appearing lesions which are hard and take biopsy into consideration, and to improve the specificity of ultrasound to rule out biopsy for lesions categorized as BI-RADS category 3 or 4A [1, 3]. Both strain elastography and shear wave based elastography yield similar performance, and there is no evidence to suggest that one technique is superior to another[1].

In conclusion, ultrasound elastography is a new technique that improves the specificity and sensitivity in differentiating malignant and benign breast lesions. Clinicians should be aware of the different types of ultrasound elastography, since it varies across different manufacturers. Elastography features, such as lesion stiffness, homogeneity and size ratios may be helpful in characterizing focal lesions seen on conventional breast ultrasound images. Ultrasound elastography has the potential to be used in the identification of malignant axillary lymph nodes and in targeting the most suspicious portions of a mass for biopsy [4].

## References

1. Barr RG, Nakashima K, Amy D, *et al*. WFUMB guidelines and recommendations for clinical use of ultrasound elastography: Part 2: breast. Ultrasound Med Biol, 2015, 41: 1148–1160.
2. Kan QC, Cui XW, Chang JM, *et al*. Strain ultrasound elastography for liver diseases. J Hepatol, 2015, 63: 534.
3. Cosgrove D, Piscaglia F, Bamber J, *et al*. EFSUMB guidelines and recommendations on the clinical use of ultrasound elastography. Part 2: Clinical applications. Ultraschall in der Medizin, 2013, 34: 238–253.
4. Cui XW, Jenssen C, Saftoiu A, *et al*. New ultrasound techniques for lymph node evaluation. World J Gastroenterol, 2013, 19: 4850–4860.

**DOI 10.1007/s10330-017-0220-0**
**Cite this article as:** Cui XW, Deng YB. Breast ultrasound elastography. Oncol Transl Med, 2017, 3: 47–48.

Oncology and Translational Medicine
DOI 10.1007/s10330-016-0196-6
April 2017, Vol. 3, No. 2, P49–P51

ORIGINAL ARTICLE

# Ultrasonographic features of breast ductal carcinoma in situ*

**Liping Wang, Youbin Deng (✉), Xinwu Cui**

Department of Medical Ultrasound, Tongji Hospital, Tongji Medical College, Huazhong University of Science and Technology, Wuhan 430030, China

## Abstract

**Objective** The aims of this study were to analyze ultrasound features of breast ductal carcinoma in situ (DCIS) and to evaluate the value of ultrasonography (US) in early diagnosis of DCIS.

**Methods** From July 2013 to March 2015, 180 patients with histologically proven DCIS were evaluated. US features recorded included the size, shape, margins, internal echogenicity, microcalcifications, posterior echogenicity, and blood supply. The data were analyzed and compared with mammographic and histologic findings.

**Results** Among 180 cases of DCIS, 168 patients had positive findings on US; the lesions were divided into 3 categories: (1) hypoechoic lesions with or without microcalcifications (n=94); (2) hypoechoic dilated ducts with or without microcalcifications (n=59); (3) microcalcifications alone without any other findings (n=15). Of the 180 lesions, microcalcifications were demonstrated by mammography in 128 (71%); among these 128 lesions, 90 were identified with microcalcifications on US. Only 80 cases (44%) manifested as masses or asymmetric densities on mammography. The diagnostic accuracy of US and mammography was 67% (120/180) and 69% (124/180), respectively, which can be improved to 80% (144/180) if US is combined with mammography.

**Conclusion** US can be used as an important tool in diagnosis of DCIS. The combination of US and mammography can improve the diagnostic accuracy of breast DCIS.

Received: 4 August 2016
Revised: 4 September 2016
Accepted: 25 October 2016

**Key words:** ultrasound; breast cancer; ductal carcinoma in situ; diagnosis

## Introduction

Ductal carcinoma in situ (DCIS) of the breast is defined as proliferation of malignant epithelial cells within ducts without evidence of invasion or infiltration through the basement membrane into the surrounding stroma, and has a much better prognosis than invasive cancers [1]. DCIS itself does not result in death, and breast cancer-specific mortality among women with DCIS is extremely low, with 1.0% to 2.6% mortality from invasive breast cancer (IBC) 8 to 10 years after a diagnosis of DCIS [2]. Therefore, early detection of DCIS is essential for improving the prognosis of breast cancer. The development of ultrasonography (US) has made it possible to detect almost any early and small lesions in the breast.

In this study, we retrospectively evaluated the value of US examination for the diagnosis of DCIS. We also summarize and illustrate the US features of DCIS and compare it with mammographic and histologic findings.

## Patients and methods

### Patients

From July 2013 to March 2015, 180 cases of DCIS were diagnosed at our hospital; all patients underwent surgical treatment and had pure DCIS on pathological examination (no invasion or microinvasion). The median age was 53 years (range, 35–80 years); US and mammography were performed in all cases before excision.

✉ Correspondence to: Youbin Deng. Email: ybdeng2007@hotmail.com
* Supported by a grant from the National Natural Sciences Foundation of China (No. 81571695).

### US examination techniques and methods

GE LogiqE9 (GE Medical Systems, USA) and Siemens Acuson S3000 (Siemens, Germany) US systems were used with a high-frequency linear transducer (8–13 MHz). Whole breasts were routinely scanned, and transverse, longitudinal, and radial views of each lesion were obtained. Lesions were described in terms of size, shape, margin, internal echogenicity, ductal extension, posterior echogenicity, and microcalcifications, as well as blood supply. Images were retrospectively reviewed by three sonographers with 3, 5, and 8 years of clinical experience, respectively, and the US features were recorded with reference to the mammographic and clinic findings. US findings were divided into mass, ductal change, and pure microcalcifications. A mass was examined in two different planes. When the lesion did not exactly correspond to the definition of a mass, but rather to echo-filled distended ducts, we defined the lesion as a ductal change. When the lesion appeared as microcalcifications without any other local findings, we defined the lesion as pure microcalcifications. When mammography revealed microcalcifications not found by US, we repeated the US according to the location found by mammography.

## Results

There were 12 false negatives on US among all 180 cases, and a total of 168 lesions were found on US. The US findings in these lesions were as follows: (1) hypoechoic masses with or without microcalcifications ($n$ = 94). The shape was irregular and the margin was indistinct (Fig. 1). (2) Hypoechoic dilated ducts with or without microcalcifications ($n$ = 59). The distended duct appeared as a flat hypoechoic nodule on US (Fig. 2). (3) Only microcalcifications without any other local findings ($n$ = 15). Clustered or scattered microcalcifications were detected with the background of normal breast tissue, and there were no local masses or dilated ducts (Fig. 3).

Of 180 cases, 120 masses were diagnosed as malignant by US, with a diagnostic accuracy of 67% (120/180), including 84 masses, 26 cases of distended ducts, and 10 pure microcalcifications.

Of 180 lesions, microcalcifications were demonstrated by mammography in 128 (71%), and only 80 cases (44%) manifested as masses or asymmetric densities on mammography; the diagnostic accuracy of mammography was 69% (124/180). In those lesions ($n$ = 128) with microcalcifications proven by mammography, 90 cases were identified with microcalcifications by US; the US detection rate of microcalcifications was 70%. The diagnostic accuracy was improved to 80% (144/180) when US was combined with mammography.

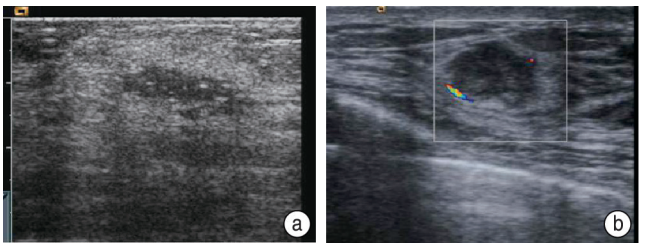


**Fig. 1** DCIS of the breast on US. (a) An irregular hypoechoic mass with microcalcifications; (b) A hypoechoic mass without microcalcifications

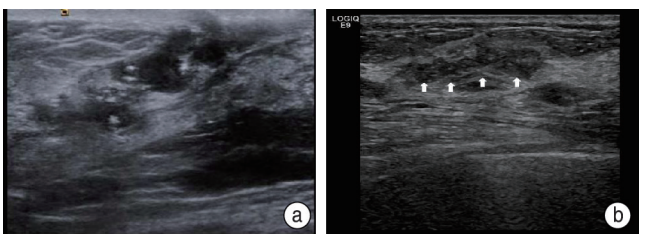


**Fig. 2** DCIS of the breast. US showed a hypoechoic dilated duct (white arrows) with microcalcifications (a) and without microcalcifications (b)

## Discussion

Mammography is regarded as the gold standard for the detection and characterization of microcalcifications, the most reliable mammographic feature of detected DCIS [3–4]. Owing to the wide use of mammography, the frequency of DCIS detection is increasing [5]. US generally has not been considered a diagnostic technique for DCIS because it is less sensitive than mammography for the identification of calcifications. However, the marked improvement of current high-frequency transducer technology has yield a high spatial resolution, allowing better and more frequent visualization of breast microcalcifications [6–7]. In our studies, the detection rate of microcalcifications with US was 70% (90/128); US can detect microcalcifications in most DCIS. When US can detect microcalcifications in lesions, US-guided procedures are preferred by patients over a mammography-guided procedure because patients are more comfortable, the breast is not compressed, and the procedure is quicker [8–9]. Furthermore, US has no ionizing radiation, and the needle can be observed in real time.

In our studies, apart from the finding of microcalcifications, DCIS appears most frequently as a solid, irregular mass with indistinct margins or as a hypoechoic mass with dilated breast ducts (153/180, 85%). Enlargement of ducts in DCIS can be attributed to tumor cells or necrosis within the duct lumen, periductal lymphocytic reaction, or periductal desmoplasia [10]. According to US features of the lesions' sharp margins, ductal extension, posterior echogenicity, and blood supply, we can easily differentiate benign from malignant

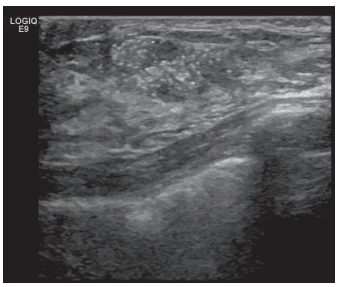


**Fig. 3** DCIS of the breast. US showed pure microcalcifications without any other findings

lesions. Furthermore, calcifications that occur within masses are easily seen on US; this is partly because most malignant solid tumors provide a very hypoechoic background, which enhances the US demonstration of the bright punctate calcification [11]. Therefore, for detecting DCIS, the advantage of US examination is the high sensitivity to find the hypoechoic masses and nodules of the breast. However, mammographic detection of DCIS lesions without microcalcifications may be quite difficult, especially in dense breasts. In our study, only 44% cases manifested as masses or asymmetric densities on mammography.

It is thought to be more difficult to identify isolated microcalcifications within normal breast tissue by using US, as normal breasts comprise much hyperechoic and heterogeneous fibrous tissue. Only 15 cases were found with clustered or scattered microcalcifications under the background of normal breast tissues in our study. This is mainly due to a lack of contrast between normal parenchyma with hyperechoic heterogeneous fibrous structures and the microcalcifications [11]. Thus, the microcalcifications associated with DCIS are not easily visualized on US unless a mass is formed. In these patients, we performed US carefully at the location that was revealed by mammography in order to increase the US detection rate of microcalcifications.

DCIS is the early stage of breast cancer; therefore, early detection of DCIS is essential for improving the prognosis of breast cancer. In our study, the diagnostic accuracy of US and mammography was 67% and 69%, respectively, but when combining US and mammography, the diagnostic accuracy can be improved to 80%.

However, we only analyzed the ultrasound features of DCIS in this study, not including DCIS with microinvasion; therefore, the method for differentiating DCIS from DCIS with microinvasion has not been discussed.

In conclusion, our results show various US features of breast DCIS. US plays an important role in detecting DCIS with or without calcifications and in evaluating disease in women with dense breasts. US examination is an effective non-invasive method for identifying and localizing breast microcalcifications. US with a high-frequency transducer can be used along with mammography in detecting and evaluating DCIS of the breast.

### Conflicts of interest

The authors indicated no potential conflicts of interest.

## References

1. Jia-Min B Pang, Kylie L Gorringe, Stephen B Fox, *et al*. Ductal carcinoma in situ – update on risk assessment and management. Histopathology, 2016, 68: 96–109.
2. Mardekian SK, Bombonati A, Palazzo JP. Ductal carcinoma in situ of the breast: the importance of morphologic and molecular interactions. Hum Pathol, 2016, 49: 114–123.
3. Weigel S, Decker T, Korsching E, *et al*. Calcifications in digital mammographic screening: improvement of early detection of invasive breast cancers? Radiology, 2010, 255 : 738–745.
4. Min Sun Bae, Woo Kyung Moon, Jung Min Chang, *et al*. Mammographic features of calcifications in DCIS: correlation with oestrogen receptor and human epidermal growth factor receptor 2 status. Eur Radiol, 2013, 23: 2072–2078.
5. Mi Young Kima, Hyeon Sook Kimb, Nami Choia, *et al*. Screening mammography-detected ductal carcinoma in situ: mammographic features based on breast cancer subtypes. Clin Imaging, 2015, 39: 983–986.
6. Wang LC, Sullivan M, Du H, *et al*. US appearance of ductal carcinoma in situ. Radiographics, 2013, 33: 213–228.
7. Hashimoto BE, Kramer DJ, Picozzi VJ. High detection rate of breast ductal carcinoma in situ calcifications on mammographically directed high-resolution US. J Ultrasound Med, 2001, 20: 501–508.
8. Bae S, Yoon JH, Moon HJ, *et al*. Breast Microcalcifications: Diagnostic Outcomes According to Image-Guided Biopsy Method. Korean J Radiol, 2015, 16: 996–1005.
9. Hahn SY, Shin JH, Han BK, *et al*. Sonographically-guided vacuum-assisted biopsy with digital mammography-guided skin marking of suspicious breast microcalcifications: comparison of outcomes with stereotactic biopsy in Asian women. Acta Radiol, 2011, 52: 29–34.
10. Cho KR, Seo BK, Kim CH, *et al*. Non-calcified ductal carcinoma in situ: ultrasound and mammographic findings correlated with histological findings. Yonsei Med J, 2008, 49: 103–110.
11. Nagashima T, Hashimoto H, Oshida K, *et al*. Ultrasound Demonstration of Mammographically Detected Microcalcifications in Patients with Ductal Carcinoma in situ of the Breast. Breast Cancer, 2005, 12: 216–220.

**DOI 10.1007/s10330-016-0196-6**
**Cite this article as:** Wang LP, Deng YB, Cui XW. Ultrasonographic features of breast ductal carcinoma in situ. Oncol Transl Med, 2017, 3: 49–51.

Oncology and Translational Medicine
DOI 10.1007/s10330-016-0195-5

April 2017, Vol. 3, No. 2, P52–P56

ORIGINAL ARTICLE

# Quantitative differential diagnosis of breast tumors using shear wave velocity and different probe orientations*

**Yuan Huang, Youbin Deng (✉), Liping Wang, Xinwu Cui**

Department of Medical Ultrasound, Tongji Hospital, Tongji Medical College, Huazhong University of Science and Technology, Wuhan 430030, China

## Abstract

**Objective** The aim of this study was to evaluate the additional benefit of the difference of maximum and minimum shear wave velocity (SWV) values obtained at different probe orientations (D-value) for the differential diagnosis of breast tumors.

**Methods** SWV (m/s) was measured in 123 breast tumors (92 benign, 31 malignant) in 76 female patients with the probe placed on the transverse, longitudinal, and 45° planes. The areas under the receiver operating characteristic (AUROC) curves were compared with respect to the maximum SWV, minimum SWV, D-value, maximum SWV combined with the D-value, and minimum SWV combined with the D-value.

**Results** There was a significant difference among the values of the maximum SWV, minimum SWV, and D-value for the 3 planes ($P < 0.001$). The AUROC curves for the maximum SWV, minimum SWV, and D-values of the 3 planes were 0.751 ($P = 0.379$), 0.486 ($P = 0.863$), and 0.603 ($P = 0.204$), respectively. The cutoff value for the maximum SWV for differentiating benign tumors from malignant tumors was 2.51 m/s (sensitivity 67%, specificity 50%). The cutoff value for the minimum SWV was 1.61 m/s (sensitivity 53%, specificity 50%). Adding the D-value increased the AUROC curve for the maximum SWV from 0.571 to 0.733 and the minimum SWV from 0.486 to 0.504 ($P = 0.964$), respectively.

**Conclusion** SWV differs in different planes of breast tumors. The D-value can provide a reference for the differential diagnosis of breast tumors.

Received: 4 August 2016
Revised: 4 September 2016
Accepted: 25 September 2016

**Key words:** shear wave; elastography; velocity; D-value; breast tumor; differential diagnosis

Shear wave elastography has recently emerged as a novel method for quantitatively measuring tissue elasticity [1]. With this method, the probe produces an acoustic push pulse that induces a low-frequency shear wave that travels transverse to the axis of the probe in tissues [2]. Shear wave velocity (SWV) is positively correlated with tissue stiffness. The SWV increases as the tissue gets stiffer. This technology has been used in the differential diagnosis of benign and malignant breast lesions. By measuring the SWV of breast tumors, the properties of the breast lesions can be identified [3–4]. Past studies have shown that the SWV varies in myocardial [5–6] and skeletal muscles [7–8] with different orientations of the probe, suggesting that the cell and fiber orientations of the tissue may affect the SWV that travels through tissue. Thus, probe orientation should be considered when SWV is measured in such tissues. This study aimed to determine the impact of probe orientations on the SWV of breast tumors.

## Materials and methods

### Patients

We collected data from 76 female patients (mean age, 38 ± 14 years; range, 14–65 years) with breast lesions who were treated between May 2012 and January 2015. Ultrasonography (US) was performed among these 76 patients before Mammotome excision, and follow-up of the pathological results was performed. Overall, 123 breast tumors (size range, 0.4–14.3 cm; mean, 1.74 ± 1.39 cm) were assessed.

✉ Correspondence to: Youbin Deng. Email: ybdeng2007@hotmail.com
* Supported by a grant from the National Natural Sciences Foundation of China (No. 81571695)

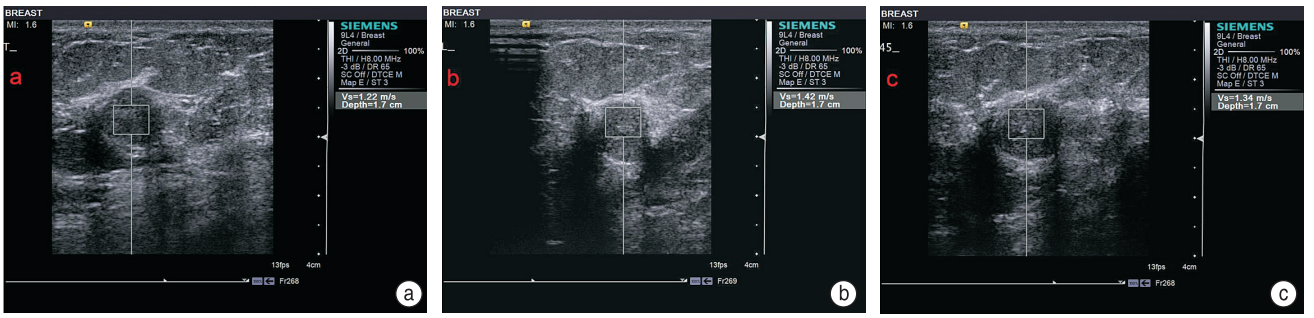


**Fig. 1** SWV in 3 planes located in the same region of a breast fibroadenoma. (a) SWV measured in the transverse plane in 1.22 m/s; (b) SWV in the longitudinal plane is 1.47 m/s; (c) SWV in the 450 plane is 1.34 m/s. For this tumor, the SWV in the transverse plane was the smallest, while the SWV in the longitudinal plane was the largest.

## Machine and methods

Breast US was performed using a Siemens S2000 ultrasound system equipped with a linear array transducer with a bandwidth of 4–9 MHz. First, conventional breast US was performed, and then quantitative implementation was used with the probe smoothly pressed at the center of the tumor. The patient was required to hold her breath, and the SWV was measured in 3 different planes (i.e., the transverse, longitudinal, and 45°; Fig. 1). For tumors in large breasts in which the region of interest (ROI) was deep in the tissue, we chose capillary vessels or tissue fiber as the reference to keep the ROI in the center of the tumor with the same depth. Measurements were repeated twice in each orientation and the mean SWV value was calculated. The mean value of the different orientations was compared, the maximum and minimum values were identified, and the difference of maximum and minimum SWV values (D-values) was calculated. We failed to obtain the SWV when it exceeded the measurable scale, the tissue in the ROI was heterogeneous, or when a liquid necrosis component was present [7], and their SWVs were displayed as X.XX m/s in Fig. 2.

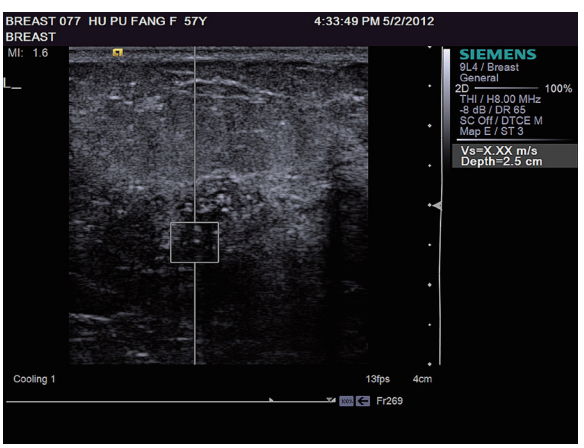


**Fig. 2** Shear wave velocity in breast invasive duct cancer displayed as x.xx m/s. Rough calcium can be seen on B-mode ultrasonography.

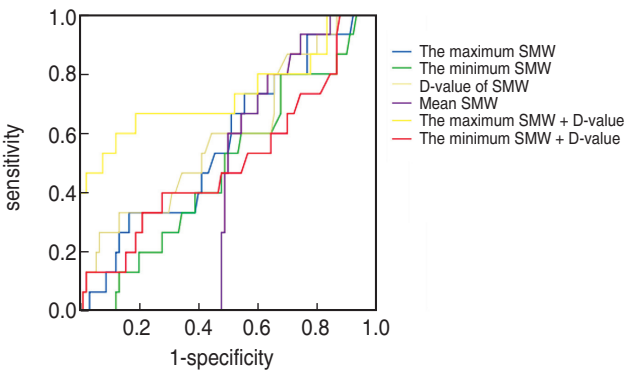


**Fig. 3** Receiver operating characteristic (ROC) curves of the maximum SWV, the minimum SWV, mean value, D-value, and these variables combined with the D-value of SWV in breast tumors in the same region.

### Statistical analysis

SPSS 17.0 software was used, and results were presented as mean ± SD. An analysis of variance was used to evaluate the differences between the maximum, medium, and minimum SWVs on different planes. Additionally, *t*-tests were used to differentiate between the different pathological types. The maximum SWV, minimum SWV, and D-value were obtained from receiver operating characteristic (ROC) curves, and the areas under the receiver operating characteristic (AUROC) curves were compared. *P*-values < 0.05 were considered significant.

## Results

A total of 123 lesions from 76 patients were examined. There were 92 benign tumors in 48 patients (18 fibroadenoma, 16 mastopathy, and 58 mastopathy with fibroadenoma, respectively). Overall, the SWVs were successfully measured in 91 lesions, but there was one case (mastopathy with fibroadenoma) in which the SWV could not be assessed. There were 31 malignant tumors in 28 patients including 26 invasive breast duct carcinomas, 2 lobar cancers, 2 breast duct carcinomas in situ, and 1

**Table 1** Comparison between the maximum and minimum SWV of the 3 planes of breast tumors (m ± s m/s)

| Pathological types of breast tumors | *n* | Maximum SMW | Minimum SMW | D-value | *P* |
|---|---|---|---|---|---|
| Benign | 92 (1)* | 2.49 ± 0.73 | 2.09 ± 0.72 | 0.68 ± 0.47 | < 0.001 |
| Malignant | 31 (16)* | 2.67 ± 0.71 | 1.74 ± 0.54 | 0.93 ± 0.63 | < 0.001 |
| *P* | 30 | 0.700 | 0.458 | 0.065 | |

mucoid cancer. Among the 31 malignant tumors, the SWVs in 15 breast tumors were measured, while those in 16 tumors (14 invasive breast duct carcinomas, 1 mucoid tumor, and 1 lobar tumor) were displayed as X.XX m/s.

Of the 106 successfully measured lesions, the maximum and minimum SWV values on the 3 planes were (2.51 ± 0.73) m/s and (1.79 ± 0.61) m/s, respectively. A *t*-test showed a significant difference between the maximum and minimum SWV, with a D-value of (0.72 ± 0.50) m/s ($P < 0.001$). For the 91 benign tumors, the maximum SWV, minimum SWV, and D-value were (2.49 ± 0.73) m/s, (2.09 ± 0.72) m/s, and (0.68 ± 0.47) m/s, respectively ($P < 0.001$). For the 15 malignant tumors, the maximum SWV, minimum SWV, and D-value were (2.67 ± 0.71) m/s, (1.74 ± 0.54) m/s, and (0.93 ± 0.63) m/s, respectively ($P < 0.001$), and the D-values of the SWV for benign and malignant tumors were (0.68 ±0.47) m/s and (0.93 ± 0.63) m/s, respectively ($P = 0.056$; Table 1). The AUROC curves of the maximum SWV, minimum SWV, and D-value were 0.571 ($P = 0.379$), 0.486 ($P = 0.863$), and 0.603 ($P = 0.204$), respectively (Fig. 3 and Table 2). The cutoff of the maximum SWV for the differential diagnosis of benign and malignant lesions was 2.51 m/s (sensitivity 67%, specificity 50%). The cutoff of the minimum SWV was 1.61 m/s (sensitivity 53%, specificity 50%). The cutoff of the D-value was 0.64 m/s (sensitivity 60%, specificity 56%). The maximum SWV and the D-value had similar AUROC curves, with no significant differences ($Z = 0.29$, $P = 0.38$). With the addition of the D-value, the AUROC curves of the maximum and minimum SWV increased from 0.571 to 0.733 ($P = 0.004$) and from 0.486 to 0.504 ($P = 0.964$), respectively (Table 2). The maximum SWV was

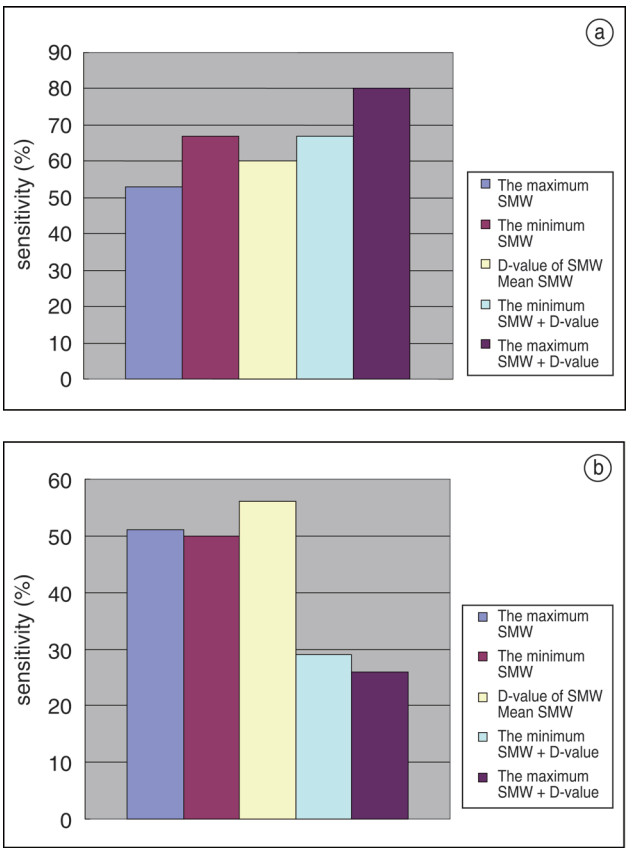


**Fig. 4** Sensitivity and specificity of the minimum SWV, maximum SWV, and D-value and these variables combined with the D-value.

associated with the maximum AUROC curve after being combined with the D-value (Fig. 3 and 4).

## Discussion

The shear wave is produced by a normal linear array probe inducing regional movement that travels transverse across the tissue, vertically to the axis of the probe. An acoustic push pulse causes tissue movement and produces a shear wave, the velocity of which can reflect tissue stiffness. By measuring the SWV of the tissue, the stiffness

**Table 2** Comparison of the maximum SWV, the minimum SWV, the D-value, and these combined with the D-value of SWV

| Variable | Area | 95% CI | | Cutoff | Sensitivity (%) | Specificity (%) |
|---|---|---|---|---|---|---|
| | | Down | Up | | | |
| The maximum SWV | 0.571 | 0.421 | 0.721 | 2.51 (m/s) | 67 | 50 |
| The minimum SWV | 0.486 | 0.337 | 0.635 | 1.61 (m/s) | 53 | 51 |
| Mean SWV | 0.437 | 0.327 | 0.544 | 2.13 (m/s) | 60 | 50 |
| D-value of SWV | 0.603 | 0.445 | 0.760 | 0.64 (m/s) | 60 | 56 |
| The maximum SWV + D-value | 0.733 | 0.562 | 0.904 | 0.501 | 80 | 40 |
| The minimum SWV + D-value | 0.504 | 0.336 | 0.671 | 0.611 | 67 | 30 |

of the tissue in an ROI can be quantitatively assessed [9]. The shear modulus is a variable that reflects the tissue elasticity and can be calculated by the equation $\mu = \rho c2$, in which $\mu$ represents the shear modulus (i.e., the property of stiffness); shear wave has a velocity range of 1–10 m/s. According to the equation, SWV increases with regional stiffness [10].

It could be assumed that the shear wave travels in homogeneous tissue, SWV correlates with tissue elasticity, and that these should be constant in different orientations. Shear wave elastography has now been clinically used in breast tissue and other organs, such as the liver [11] and muscle [12]. In homogeneous tissues like liver, the SWV has high accuracy and repeatability [13]. However, the SWV varies as the fiber orientation of the muscle changes. Deffieux *et al*. investigated the biceps and found that the shear wave that is parallel to the fiber orientation of the muscle travels the fastest [7]. In striated muscle of healthy volunteers, the SWV tends to decrease as the angle across the muscle fiber orientation and the probe orientation increases [8]. Our previous study also showed that the shear modulus of different myocardial fiber layers changed when the probe was placed in different orientations [5]. This finding suggests that, in myocardial fiber, a shear wave travels faster in an orientation parallel to the fiber orientation.

This study showed that the value for the regional SWV of breast tumors changed as the probe orientation changed. It can be inferred that when the angle varies between the probe and fiber orientation in different planes, the probe orientation across the breast tumor will induce differences in the SWV on these different planes. The SWV was compared and analyzed in both benign and malignant tumors, and the value differed depending on the specific pathology. This difference may have been partly caused by the pathological tissue composition that varies at different orientations. Thus, the D-value of SWV should be considered when using SWV for quantitative differential diagnosis [14]. The AUROCs of the maximum SWV, minimum SWV, and D-value were investigated, and the results showed that the D-value between the maximum and the minimum SWV had a bigger area than did the SWV in a single plane, which suggested that the D-value of SWV can provide a reference for the differential diagnosis between benign and malignant tumors. Furthermore, after being combined with the D-value and the maximum SWV, the diagnostic utility of the minimum SWV improved and the AUROC curve increased. Some researchers insist that the maximum value rather than the average value should be chosen for the quantification of shear modulus in the differential diagnosis of breast lesions [15]. In our opinion, as a diagnostic reference, the maximum SWV is more suitable than the minimum SWV, and the D-value considerably valuable for diagnosis. We can choose a maximum SWV and a D-value in tumors to improve the identification of benign or malignant breast tumors. Scanning through multiple planes of a tumor can help improve the specificity of diagnosis in breast tumors.

Our study had some limitations. Most malignant breast tumors were excluded because the SWV could not be measured with shear wave elastography. With this system, numerical values of the SWV were too high or could not be obtained in some benign tumors that contained calcium or fibrosis composite. For such hard tissues, the ROI was set around the fibrotic region to make data analysis of the breast tumors feasible. Mucoid cancer with a soft pathological composite should have shown a low SWV value; however, when the SWV transversed through interfaces such as liquid necrotic tissues that cause faint vibration, it could not be detected [7]. In our study, one case of mucoid cancer was discovered in which SWV could not be measured. Now, shear wave elastography has been used to characterize breast tumors as well as fat and breast tissue glands. However, the malignant cases and pathological types in this study are limited, and many more samples are needed to verify the conclusion of the study. To date, shear wave elastography has been used in the diagnosis of many diseases, including breast tumors [16]. However, adding the D-value of different planes to the SWV may optimize the differential diagnosis of breast lesions.

In conclusion, the difference of the maximum and minimum SWV on different planes can provide a reference for the differential diagnosis of breast tumors.

### Conflicts of interest

The authors indicated no potential conflicts of interest.

## References

1. Youk JH, Son EJ, Gweon HM, *et al*. Comparison of strain and wave elastography for the differentiation of benign from malignant breast lesions, combined with B-mode ultrasoundgraphy: quantitative and quantitative assessments. Ultrasound Med Biol, 2014, 40: 2336–2344.
2. Tanter M, Bercoff J, Athanasiou A *et al*. Quantitative assessment of breast lesion viscoelasticity: initial clinical results using supersonic shear imaging. Ultrasound Med Biol, 2008, 34: 1373–1386.
3. Evans A, Whelehan P, Thomson K, *et al*. Invasive breast cancer: relationship between shear-wave and elastographic findings and histologic prognostic factors. Radiology, 2012, 263: 673–677.
4. Athanasiou A, Tardivon A, Tanter M *et al*. Breast lesions: quantitative elastography with supersonic shear imaging–preliminary results. Radiology, 2010, 256: 297–303.
5. Tang QY, Deng YB, Liu K, . Quantification of shear modulus in vitro porcine myocardium using real-time shear wave elastography. Chinese J Ultrasonogr (Chinese), 2012, 8: 708–710.
6. Sengupta PP, Krishnamoorthyet VK, Narula J, *et al*. Left ventricular

form and function revisited applied translational science to cardiovascular ultrasound imaging. J Am Soc Echocardiogr, 2007, 20: 539–551.
7. Deffieux T, Montaldo G, Tanter M, *et al*. Shear wave spectroscopy for in vivo quantification of human soft tissues visco-elasticity. IEEE Trans Med Imaging, 2009, 28: 313–322.
8. Zhang J, Deng YB, Huang Y *et al*. Impact of the angle between probe scanning palne and musle fiber orentation on SWV. Chin J Med Imaging Technol, 2013, 9: 1497–1499.
9. Gallotti A, D'Onofrio M, Pozzi Mucelli R. Acoustic Radiation Force Impulse (ARFI) technique in ultrasound with Virtual Touch tissue quantification of the upper abdomen. Radiol med, 2010, 115: 889–897.
10. Pernot M, Couade M, Mateo P, *et al*. Real-Time assessment of myocardial contractility using shear wave elastography. J Am Coll Cardiol, 2011, 58: 65–72.
11. Friedrich-Rust M, Wunder K, Kriener S, *et al*. Liver fibrosis in viral hepatitis: noninvasive assessment with acoustic radiation force impulse imaging versus transient elastography. Radiology, 2009, 252: 595–604.
12. Shinohara M, Sabra K, Gennisson JL, *et al*. Real-time visualization of muscle stiffness distribution with ultrasound shear wave elastography during muscle contraction. Muscle Nerve, 2010, 42: 438–441.
13. Ferraioli G, Tinelli C, Zicchetti M, *et al*. Reproducibility of real-time shear wave elastography in the evaluation of liver elasticity. Eur J Radiol, 2012, 81: 3102–3106.
14. Huang Y, Deng YB, Wang LP, The impact of probe orientation on the SWV in breast tumors. Chinese J Ultrasonogr (Chinese), 2013, 5: 426–428.
15. Huang Y, Li JL, Wang ZhL, *et al*. Real time shear wave elastography in quantitative differential diagnosis of breast tumors. Chin J Med Imaging Technol (Chinese), 2011, 27: 561–563.
16. Muller M, Gennisson JL, Deffieux T, *et al*. Quantitative viscoelasticity mapping of human liver using supersonic shear imaging: preliminary *in vivo* feasibility study. Ultrasound Med Biol, 2009, 35: 219–229.

**DOI 10.1007/s10330-016-0195-5**
**Cite this article as:** Huang Y, Deng YB, Wang LP, *et al*. Quantitative differential diagnosis of breast tumors using shear wave velocity and different probe orientations. Oncol Transl Med, 2017, 3: 52–56.

Oncology and Translational Medicine
DOI 10.1007/s10330-016-0194-4

April 2017, Vol. 3, No. 2, P57–P64

ORIGINAL ARTICLE

# Ultrasound-guided percutaneous microwave ablation for small liver cancers adjacent to large vessels: long-term outcomes and strategies

**Ruobing Liu, Kaiyan Li (✉), Hongchang Luo, Wei Zhang, Tingting Zhang, Meng Gao, Wenhui Zha, Xinwu Cui, Youbin Deng**

Department of Medical Ultrasound, Tongji Hospital, Tongji Medical College, Huazhong University of Science and Technology, Wuhan 430030, China

## Abstract

**Objective** The aim of the study was to evaluate the long-term efficacy and safety of percutaneous microwave ablation (MWA) for small hepatic cancers adjacent to large vessels and to investigate the treatment strategies.

**Methods** From March 2009 to July 2015, a total of 86 patients with 94 tumors underwent ultrasound (US)-guided percutaneous MWA, with pathologically proven or clinically diagnosed liver cancers measuring ≤ 3 cm in diameter and located ≤ 10 mm from a major vessel ($n$ = 94). Regular follow-up after MWA was performed to assess treatment efficacy and perioperative complications.

**Results** The complete ablation rate at 1 month after MWA was 93.3% (84/90). The 6-, 9-, 12-, 24-, 36-, 48-, 60-, 72-, and 84-month local recurrence rates were 2.4%, 2.4%, 3.7%, 6.6%, 8.4%, 8.4%, 8.4%, 8.4%, and 8.4%, respectively. There were no major complications. The perioperative special complication rate was 5.32% (5/94), including 3 cases of moderate liver function damage and 2 cases of limited sub-capsular hematoma.

**Conclusion** Percutaneous MWA for small hepatic cancers adjacent to large vessels is feasible, effective, and safe with an acceptable rate of complications. The key point is to strictly follow operative indications and adopt proper treatment strategies.

**Key words:** ultrasound (US); liver cancer; percutaneous microwave ablation (MWA)

Received: 9 October 2016
Revised: 4 December 2016
Accepted: 9 February 2017

Hepatocellular carcinoma (HCC) is the sixth most common malignancy in the world in terms of numbers of cases (626 000 or 5.7% of new cancer cases) and causes more than 500 000 deaths every year [1]. In addition, the liver is also a common site of metastasis from invasive solid tumors, such as colon cancer, breast cancer, neuroendocrine tumors, and sarcomas. The majority of patients with hepatic malignancies are not suitable for potentially curative resection due to inadequate hepatic reserve, advanced tumor stage, or other contraindications. The rate of surgical resection has been reported to be less than 30% of primary liver cancers and 10%–20% of liver metastasis [2]. Recently, ultrasound (US)-guided percutaneous microwave ablation (MWA) as a minimally invasive therapy has been developed and has been widely used in the clinical treatment of liver cancer.

Clinical evidence has confirmed the efficacy and safety of percutaneous MWA and radiofrequency ablation (RFA) for the treatment of HCC, especially for small HCCs measuring ≤ 3 cm [3–4]. However, for cases in which the tumors are adjacent to large vessels, some previous studies have defined this as a treatment contraindication because of the higher rate of complications and incomplete necrosis [5]. With the developments in technology and the accumulation of clinical experience, more studies have been published in this field. Some studies had shown that the rate of complete ablation and local tumor progression of local thermal ablation compared favorably with those far away from the large blood vessels [6–7]. Other researchers express the opinion that a lesion located in

✉ Correspondence to: Kaiyan Li. Email: Liky20006@126.com

the area adjacent to large vessels is an independent risk factor that significantly affects the outcome of RFA [5].

Thus, researchers' viewpoints are variable on this issue and the most research has focused on percutaneous RFA, not MWA, which is also an important and popular modality for small liver cancers in eastern countries, such as China and Japan. Moreover, a fact we cannot ignore is that lesions are often found in this special area abutting large vessels and MWA is different from RFA in many ways. The long-term efficacy and safety of percutaneous MWA for small liver cancers adjacent to large vessels has not been studied sufficiently. More attention needs to be given to the liver lesions in this special and high-risk region.

In the authors' institution, we have successfully performed many cases of MWA for tumors located adjacent to large vessel. To confirm the feasibility, safety, and efficiency of our approach, we evaluated complete ablation, local tumor progression, and early complications as an indicator of treatment in 86 patients with 94 lesions treated with ultrasound-guided percutaneous MWA.

## Patients and methods

### Patient selection

From March 2009 to July 2015, a total of 86 patients (66 were men, 20 women; average age 51.27 years ± 11.13 years; range 21–73 years) with 94 tumors (average diameter 2.01 cm ± 0.63 cm; range 0.8–3.0 cm) underwent ultrasound-guided percutaneous MWA at the Hepatic Surgery Center, Tongji Hospital, Tongji Medical College, Huazhong University of Science and Technology, Wuhan, China, and were enrolled in this retrospective study (Table 1).

Among these lesions, 85 lesions were diagnosed as primary HCC and 9 were liver metastasis from extrahepatic organs (2 stomach cancer, 3 colorectal carcinoma, 1 breast cancer, 1 glucagon cancer, 1 malignant interstitialoma, and 1 leiomyosarcoma). A total of 62 cases were recurrent HCC after hepatic resection and 23 cases were of primary liver carcinoma. These patients underwent percutaneous MWA because they were not suitable for hepatic resection or preferred to undergo minimally invasive therapy. All patients met the inclusion criteria and were divided into two subgroups according to tumor location. Patients were closely followed up until March 2016. Written informed consent for this procedure was obtained from all of the enrolled patients.

**Table 1** General condition of the patients (*n*)

| Characteristics | | No. of the patients |
|---|---|---|
| Patients (M/F) | | 86 (66/20) |
| Number of nodules | | 94 |
| Tumor size (cm) | Range | 0.8–3.0 |
| | mean ($\bar{\chi} \pm s$) | 2.01 ± 0.63 |
| Age (years, $\bar{\chi} \pm s$) | | 51.27 ± 11.13 |
| Hbs Ag (+) | | 65 |
| AFP (μg/L) | < 20 | 54 |
| | 20–400 | 22 |
| | > 400 | 18 |
| | mean ($\bar{\chi} \pm s$) | 598.4 ± 1868.6 |
| Indication of treatment | Primary HCC | 85 |
| | Recurrence HCC | 9 |

### Inclusion criteria

The inclusion criteria were: (1) Confirmed liver malignancy: (i) primary or metastatic liver cancer was confirmed by pathology through a tumor biopsy before ablation; (ii) HCC diagnosis: tumor markers [alpha-fetoprotein (AFP) ≥ 200 μg/L] and at least two of the following modalities confirmed the diagnosis of HCC: contrast-enhanced ultrasound (CEUS), contrast-enhanced computed tomography (CECT), or contrast-enhanced magnetic resonance imaging (CEMRI); (iii) liver metastasis diagnosis: tumors were identified on at least two modalities (CEUS, CECT, or CEMRI) that indicated liver cancer. (2) Tumors located adjacent to large vessels. (3) Accessibility of tumors via a percutaneous approach under ultrasound guidance. (4) The size of a single nodule of HCC or a metastasis was ≤ 3 cm and the number of tumors was three or fewer. (5) No portal vein embolus or extrahepatic metastases. (6) The prothrombin time was less than 25 s, the prothrombin time activity percentage was higher than 40%, and the platelet count was ≥ 40 cells × $10^9$ /L. The maximum diameter of the nodules was measured by US in more than two planes.

### Definition of the special locations

All of the lesions were located less than 5 mm from large vessels, which were defined as the main, first, or second branch of the portal vein (group A), the base of the hepatic veins, or the inferior vena cava (group B). There were 42 lesions in group A and 52 lesions in group B. The distance between the edge of the nodule and the large vessel was measured by scanning multiple planes on US, computed tomography (CT), or magnetic resonance imaging (MRI).

### Treatment strategy

Percutaneous MWA was performed using an ECO-100c microwave system (Qinghai Microwave Electronic Research Institute, Nanjing, China) with a frequency of 2450 MHz and a power output of 0–100 W. All of the patients underwent ultrasound with a 3.5-MHz microconvex probe (Aloka, Tokyo, Japan) that was matched with a biopsy guide (Aloka, Tokyo) to confirm the range and relationship with its surrounding structures including the large vessels, main duct, and others and

based on it, the puncture route, organ avoidance, and location of needle points should be well planned. First, pentazocine (50 mg; pethidine hydrochloride, Qinghai Pharmaceutical, Xining, Qinghai Province, China) was intra-muscularly injected, and then local anesthesia (10 mL of 2% lidocaine; Shanghai Fosun Industrial, Shanghai, China) was applied. After local anesthesia, a 14-gauge, 18-cm-long, internally-water-cooled MWA antenna (Qinghai Microwave Electronic Research Institute, Nanjing, China) was inserted into the center of the tumor under ultrasound guidance (Aloka ProSoundα 7 or Philips EPIQ5) and the microwave system was set at 60 W output and at a 6-min ablation cycle. The entire procedure was continuously monitored using ultrasound. The coagulation necrosis area was carefully checked after the ablation to ensure it covered the lesions' edges by more than 5 mm in cases of ablation failure [8].

### Follow up

All of the patients underwent CECT, CEUS, or CEMRI as well as blood chemistry tests, including AFP and liver function tests, at 1 month post-ablation, to evaluate the treatment results. The tumor was considered to have undergone completed necrosis on the basis of all the following findings: (1) the lack of enhancing tissue at the ablated tumor site; (2) the non-enhancing area extended beyond the tumors' borders; and (3) the margins of the ablation zone were smooth and sharp. The tumor was defined as having received incomplete ablation if enhancing tissue at the ablated tumor site was found, which needed additional treatment. US and blood chemistry was performed every month and enhanced imaging follow-up tests (CEUS, CECT, or CEMRI) were performed every 3–6 months after MWA for the first year after MWA and then every 3 months and 6–12 months during the next year.

During the follow-up period, all of the patients were observed for recurrence at the ablation zone and for new intra-hepatic distant recurrence (IDR). Local tumor progression (LTP) was defined as an enhancing nodule within or around the initial complete ablation zone, and IDR was indicated by an enhancing nodule distant from the complete ablation zone in the liver. These two different types of recurrence (LTP and IDR) were defined as intra-hepatic recurrence. LTP was described by the local tumor recurrence rate. Cases in which patients with intrahepatic multiple tumors in end-stage were excluded and the lesions ablated were covered. Major complications were defined as one that might threaten a patient's life, lead to substantial morbidity and disability, or result in a lengthy hospital stay if left untreated. Other complications were considered minor [9].

### Statistical analysis

SPSS 19.0 statistical software was used to analyze the variables. For continuous variables such as liver function, a normal test was used. The appropriate normal transform method was chosen to meet the normal distribution, and then, a paired *t*-test was used. The general data of the patients, such as the hospitalization days after treatment, age, AFP levels, tumor size, and postoperative temperature, were described as $\bar{\chi} \pm s$. For qualitative variables such as ablation rate and local recurrence rate, the $\chi^2$-test was used. The total local recurrence rates were calculated using the Kaplan-Meier method. A $P$ value < 0.05 was considered statistically significant.

## Results

### Patients' general condition post-treatment

All patients with local anesthesia felt uncomfortable during and after the treatment process, and the major toxicities included tenderness beneath the xiphoid process and shoulder pain, but they were tolerable and did not affect the success of treatment. Eight cases developed mild gastrointestinal symptoms after the operation, e.g., nausea, vomiting, and poor appetite.

The average temperature of the 94 cases was (36.93 ± 0.51) °C, 1 day after the treatment and no patient had a marked fever. The average number of hospitalization days was (3.88 ± 3.1) days after treatment. There was no significant difference between the groups considering the general condition of patients (Table 2).

### Effectiveness of percutaneous MWA treatment

Eighty-four (93.3%) of the 90 tumors exhibited a complete ablation after the MWA by contrast-enhanced imaging (CEUS/CECT/CEMRI; Fig. 1 and 2). Six tumors were confirmed to be incompletely ablated 1 month after the treatment, of which 3 received a subsequent secondary ablation. One was treated with radiotherapy and 2 underwent conservative palliative treatment. Treatment success at 1 month after the initial and secondary ablations was observed in 87 of the 89 tumors. The complete ablation rate in group A (Fig. 1) and group B (Fig. 2) was 92.7% vs. 93.9% ($P$ = 0.821) with no statistically significant difference. Moreover, 4 cases were lost to follow-up after discharge (Table 2).

### Early complications

All of the 86 patients had transiently damaged liver function, which was measured by five indicators [serum glutamic-pyruvic transaminase (GPT/ALT), glutamic-oxaloacetic transaminase (GOT/AST), albumin (ALB), total bilirubin (TBIL), and prothrombin time (PT)]. The levels of ALT, AST, and TBIL in the pre-MWA group were higher than in the post-MWA group; in addition, the level

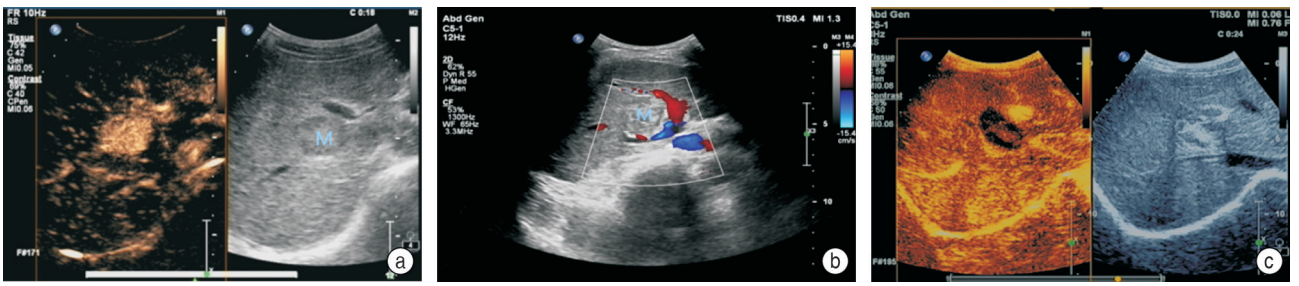

**Fig. 1** MWA for a nodule located on the porta hepatis of group A. (a and b) This patient had hypervascular HCC in segment 8 (M), between the right anterior branch of the portal vein and the base of the right hepatic vein, and near the inferior vena cava. (c) After the treatment, the nodule was completely ablated. The patient had no complications such as hemorrhage or duct injury.

**Table 3** Comparison of hepatic function before and after treatment

| Hepatic function | Pre-treatment group | Post-treatment group | Paired numbers | *t* | *P* |
|---|---|---|---|---|---|
| ALT (U/L) | 30.20 ± 18.9 | 123.9 ± 88.5 | 71 | –13.074 | < 0.001 |
| AST (U/L) | 31.84 ± 22.32 | 149.8 ± 114.3 | 69 | –13.822 | < 0.001 |
| ALB (g/L) | 40.72 ± 6.91 | 37.45 ± 6.02 | 70 | 4.485 | < 0.001 |
| TB (μmol/L) | 14.09 ± 10.1 | 17.94 ± 7.72 | 66 | –4.348 | < 0.001 |
| PT (s) | 13.71 ± 1.56 | 13.92 ± 2.94 | 42 | 1.048 | 0.31 |

Note: All five indicators did not meet the normal distribution, and we chose the appropriate normal transformation method (extraction of root) to meet it; the *P* value of the K-S normal-tests were all greater than 0.05

of ALB was lower pre-treatment than post-treatment, and the differences were statistically significant ($P < 0.001$). There was no statistically significant difference between the groups before and after treatment for PT ($P = 0.31$; Table 3).

Moderate hepatic function damage was found in 3 cases after the operation (ALT ≥ 300 U/L, TBIL 34.2–51.3 μmol/L, PT prolonged by 3–5 s, moderate ascites, blood ammonia was higher than the normal level, or more than three of the five indicators listed occurred simultaneously [10]) and minor hepatic function damage occurred in the other 91 cases. For patients who had minor hepatic damage, their hepatic function level recovered to the pre-

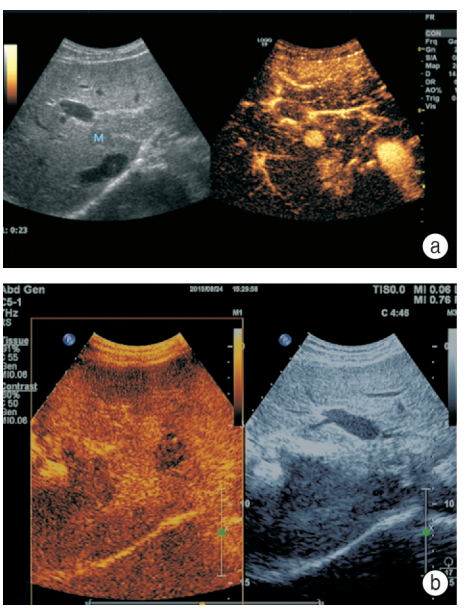

**Fig. 2** MWA for a nodule located on the porta hepatis of group B. (a) This patient had hypervascular HCC close to the inferior vena cava, and the minimum distance was 4 mm measured by ultrasound scans. (b) After the treatment, the nodule was completely ablated with a well-defined perfusion defect in the late phase. The patient had no complications such as hemorrhage or duct injury.

**Table 2** Effectiveness of MWA and patients' general condition

| Variables | | Group A | Group B | Total | $T(\chi^2)$ | *P* |
|---|---|---|---|---|---|---|
| *n* | | 41 | 49 | 90 | | |
| Hospitalization days (day, $\overline{\chi} \pm s$) | | 3.98 ± 3.33 | 3.8 ± 3.05 | 3.88 ± 3.1 | 0.555 | 0.237 |
| Temperature (°C, $\overline{\chi} \pm s$) | | 36.96 ± 0.47 | 36.9 ± 0.55 | 36.93 ± 0.51 | 0.262 | 0.692 |
| Effectiveness | Complete ablation | 38 | 46 | 84 | 0.051 | 0.821 |
| | Incomplete ablation | 3 | 3 | 6 | | |
| | Ratio (%) | 92.7 | 93.9 | 93.3 | | |
| Local recurrence | N | 35 | 43 | 78 | 0.059 | 0.808 |
| | Y | 3 | 3 | 6 | | |
| | Ratio (%) | 7.9 | 6.5 | 7.7 | | |

Note: Four cases were missing in the follow-up period. Group A: lesions adjacent to the main, first, or second branch of the portal vein; group B: lesions adjacent to the base of hepatic veins or the inferior vena cava. The *T*-test was performed for comparing temperature and hospitalization days and the $\chi^2$-test was performed for comparing local recurrence rate and effectiveness.

peration level after being treated with hepatic protection agents and measures to reduce jaundice for 3 to 7 days and they returned to a normal level after 2 months.

There were 5 cases of special complications among the 94 cases of treatment for tumors adjacent to large vessels. Two patients encountered limited sub-capsular hematomas of the liver. Ninety-four cases had hepatic function damage, including 91 cases of mild liver function damage and 3 cases of moderate liver function damage. Liver function returned to the preoperative state after 3–7 days' symptomatic treatment in patients with mild liver function damage. There were no significant differences between the two groups.

In the 3 patients with moderate impairment of liver function, five blood chemistry indicators were measured on the postoperative first and 7th day. The average levels of ALT, AST, ALB, and TBIL returned from 419 U/L, 420 U/L, 36 g/L, and 24.7 μmol/L to 134 U/L, 36.3 U/L, 32.7 g/L, and 13.3 μmol/L, respectively, and had returned to a normal level 2 months later.

Bleeding around the puncture site occurred in 2 cases, but the amount was limited. One patient was cured after 40 mL of dark red fluid was drawn off via ultrasound-guided percutaneous needle aspiration. The volume of sub-hepatic localized liquid in the other case was 3.9 cm × 1.9 cm, but the patient recovered without needing treatment.

There were no major complications. Five cases had minor complications and the mean hospital stay was 7 days. The overall postoperative morbidity rate of minor complications was 5.32% (5/94), and no deaths were directly associated with complications of MWA ablation.

## Long-term clinical outcomes

The mean follow-up period was (30.5 ± 20.0) months, and the median follow-up period was 28.0 months (range, 6.0–84.0 months) after MWA for these 90 cases. The median time to local tumor recurrence was 7.0 months (range, 6.0–86.0 months). There were 6 of 84 tumors (7.7%) that developed a local recurrence, 7.9% vs. 6.5% in groups A and B with no statistically significant difference, i.e., 3 cases per group. Of the 84 tumors that had a complete ablation, LTP was observed during the follow-up period in 6 patients with 6 lesions (Fig. 3). The respective cumulative incidence of local recurrence using Kaplan-Meier methods at 3-, 6-, 12-, 24-, 36-, 48-, 60-, 72-, and 84-months was 2.4%, 2.4%, 3.7%, 6.6%, 8.4%, 8.4%, 8.4%, 8.4%, and 8.4%, respectively (Fig. 4).

The following therapies for LTP cases were administered to these patients: 1 patient with recurrence within 2 months after ablation was treated with traditional Chinese medicine; 1 patient with recurrence after 10 months died after local radionuclide therapy; 1 patient was cured after resection again after 8 months;

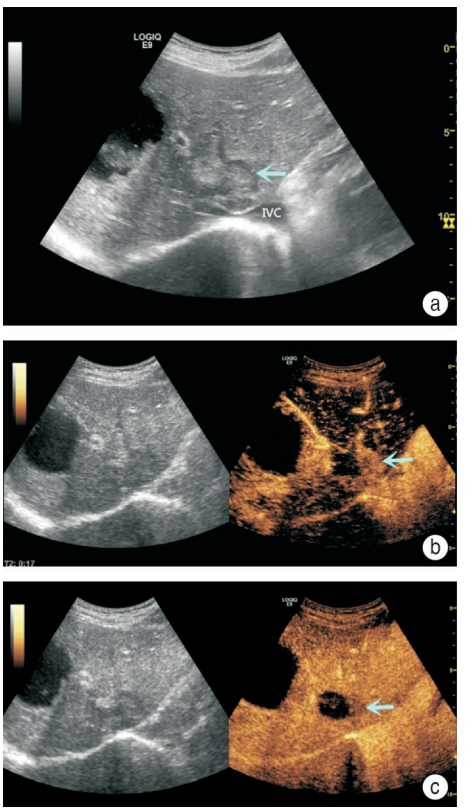


**Fig. 3** MWA for a nodule located on the porta hepatis of group B. (a) This patient underwent percutaneous MWA for hypervascular HCC in segment 4, close to the inferior vena cava. (b and c) Six months after the first treatment, a lesion of local recurrence was found (arrowheads: b: arterial phase; c: late phase).

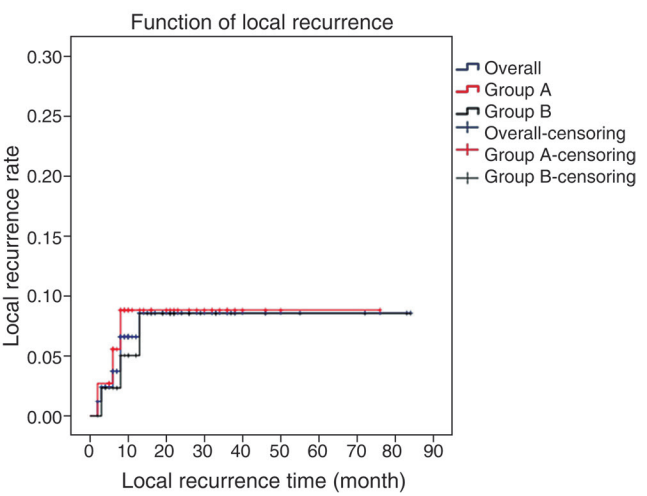


**Fig. 4** Cumulative local tumor recurrence rates after percutaneous microwave ablation for nodules close to the large vessels. The red line represents the nodules in group A, the black line represents ones in group B, and the blue line represents the overall nodules.

and 3 patients were cured in 3 months, 6 months and 19 months, respectively, after ablation with a second completed ultrasound-guided percutaneous MWA. Six cases were excluded due to tumor progression.

## Discussion

Percutaneous MWA for small liver cancers is effective and the results are comparable to surgical resection. Previous studies reported that the complete ablation rate of MWA for small HCC ranged from 95.64% to 97.6% [11–12]. Shi *et al* [13] enrolled 224 cases of primary HCC that met the standard of Milan and were divided into a surgical resection group and MWA group. The disease-free and cumulative survival was compared between the groups and the results showed that the 1-, 3-, and 5-year cumulative survival rates of the MWA group were 94.0%, 70.0%, and 52.0%, respectively, while those of the surgical resection group were 94.0%, 94.0%, and 72.0%, respectively ($P = 0.513$). The 1-, 3-, 5-years disease-free survival rates were 77%, 38%, and 18%, respectively, while those of the surgical resection group were 85%, 57%, and 31%, respectively ($P = 0.005$). For patients with a tumor diameter 3 cm or less, there were no obvious differences in cumulative survival ($P = 0.577$) or disease-free survival rates ($P = 0.140$) between the groups.

However, for patients with liver tumors adjacent to large vessels, some researchers consider them unsuitable for thermal ablation. Lu *et al* [14] reported that the rate of incompletely treated or locally recurrent tumors was 5/74 (7%) in the non-perivascular group and 15/31 (48%) in the perivascular group ($P < 0.01$). Multivariate logistic regression analysis showed that the presence or absence of a large peritumoral vessel was an independent and dominant predictor of treatment outcome. Huang *et al* [15] confirmed that the complete ablation rate was 96.3%, but local tumor progression was detected in 22 of 163 tumors (13.5%).

In the present study, the complete ablation of 90 tumors was 93.3% (84/90) and the 6-, 9-, 12-, 24-, 36-, 48-, 60-, 72-, and 84-month local recurrence rates were 2.4%, 2.4%, 3.7%, 6.6%, 8.4%, 8.4%, 8.4%, 8.4%, and 8.4%, respectively, which is in accordance with or even better than the results reported by published studies [13–15]. The difference between the two groups for different locations is not statistically significant, which suggests they can be treated equally. Compared with laparoscopic surgery and open surgery, the hospital stay and treatment cost had considerable advantages in the present study.

The main difficulty with MWA of the lesions is how to ensure the patient's safety as well as complete ablation of the tumor. In this study, early complications were rare and generally not life-threatening. No serious complications occurred during or after the treatment. Since the lesions selected for this research were located in the high-risk and special area of the liver for MWA, theoretical and operational feasibility is indispensable for obtaining satisfactory treatment and ensuring safety.

Theoretically, the wall of blood vessels is composed of smooth muscle and fibrous connective tissues in different proportions with certain elasticity and contractility. After fine needle aspiration is performed, the wall can close the pinhole through its elasticity. In addition, the liver is a parenchymatous organ and minimal bleeding may occur due to spontaneous hemostasis. In clinical practice, the following measures should be adopted to guarantee a good result: first, it is very important to strictly control the indications for patients being treated, who should have excellent hepatic and blood coagulation functions. In these cases, inner-hepatic or sub-hepatic bleeding is rare. Second, the needle insertion path should be as parallel to the blood vessel as possible, avoiding large vessels and the main bile duct and applying the principle of clinging to but not piercing the vessel wall. When the needle insertion cannot avoid all vessels along the path, the operator can choose to bypass the second order and smaller portal venous branches and distant part of the hepatic vein (distance to inferior vena cava ≥ 2 cm). In addition, for the main trunk of the portal vein and for first order branches, the inferior vena cava and near segment of the hepatic vein to the heart should definitely not be punctured because those large vessels are exposed or half-exposed outside the liver parenchyma in the area of the hepatic portal and it is difficult to control bleeding there. Third, the needle should be immediately readjusted to a location under the hepatic capsular or subcutaneous when the needle path is found to be inconsistent with the anticipated puncture path during the procedure. Then, the direction should be adjusted before inserting again. Changing the direction after the needle has pierced blood vessels or the inside of tumors is not acceptable; this can reduce potential damage to bile ducts and blood vessels and prevent seeding metastasis. Fourth, skilled and experience operators may improve the successful rate of first US-guided puncture and reduce the probability of injuries caused by repeated punctures. In our study, the treatments were done by two doctors with more than 10 years' experience in MWA (Kaiyan Li, and Hongchang Luo; see Fig. 5).

To date, many scholars have developed new technologies relying on platforms constructed by multiple disciplinary researchers. Jung *et al* [16–17] have reconstructed 3D pictures showing the relationship between tumors and important structures surrounding the liver that enable surgeons to establish and find the most appropriate needle puncture pathways through the spatial conformation. Lonardo *et al* [18] have applied a method of continuation perfusion of cold normal saline into the central bile duct of the hepatic

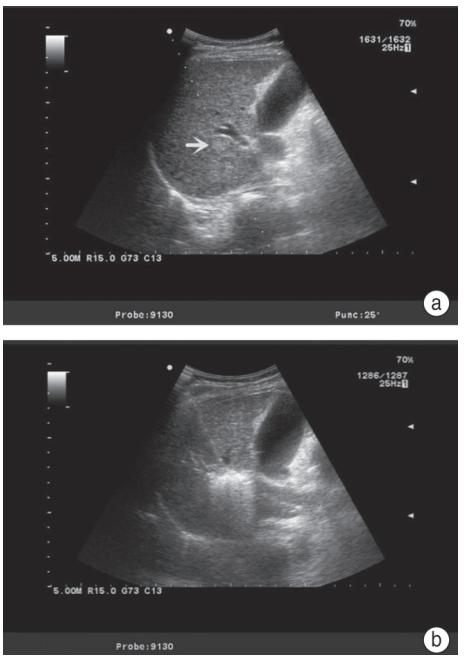


**Fig. 5** (a) The lesion lies on the visceral side of the right anterior portal branch. The puncture path inserted through the portal branch. (b) The heat distribution completely covered the original lesion area.

portal to prevent injuries to the main bile duct during the process of treating tumors with RFA.

Among the cases in this group, 6 lesions had incomplete ablation. After a careful study of post-operation CEUS, CECT, CEMRI, 2 cases had residual tumor close to great vessels and that effect might be caused by the blood flow drawing away heat during the process of treatment. Two cases were located in the periphery or original surgical scars and their borders within the scars were unclear on 2-D ultrasound images, and incorrect judgment of the scope of the lesions resulted in incomplete ablation. Residual tumors in 2 cases were found tilted to one side, which was related to the deviated needlepoint positions that did not reach accurate positions. These cases indicate that heat loss and residual tumors in the periphery of blood vessels can be reduced through moderately prolonging the MWA ablation time and combining percutaneous absolute ethanol injection (PEI) [19] and transhepatic arterial chemotherapy and embolization (TACE) [20] in areas close to great vessels. Furthermore, intraoperative enhanced ultrasound can help tumors with unclear 2-D borders attain more definite borders and scope for treatment.

## Conclusion

Percutaneous MWA for small hepatic cancers adjacent to large vessels is feasible, effective, and safe with an acceptable incidence of complications. The key point is to follow indications strictly and adopt proper strategies.

## Conflicts of interest

The authors indicated no potential conflicts of interest.

## References

1. Parkin DM, Bray F, Ferlay J, *et al*. Global cancer statistics, 2002. CA Cancer J Clin, 2005, 55: 74–108.
2. Nordlinger B, Rougier P. Nonsurgical methods for liver metastases including cryotherapy, radiofrequency ablation, and infusional treatment: what's new in 2001. Curr Opin Oncol, 2002, 14: 420–423.
3. Zhang TT, Luo HC, Cui X, *et al*. Ultrasound-guided percutaneous microwave ablation treatment of initial recurrent hepatocellular carcinoma after hepatic resection: long-term outcomes. Ultrasound Med Biol, 2015, 41: 2391–2399.
4. Zhang EL, Yang F, Wu ZB, *et al*. Therapeutic efficacy of percutaneous microwave coagulation versus liver resection for single hepatocellular carcinoma ≤ 3 cm with Child-Pugh A cirrhosis. Eur J Surg Oncol, 2016, 42: 690–697.
5. Lu DS, Raman SS, Limanond P, *et al*. Influence of large peritumoral vessels on outcome of radiofrequency ablation of liver tumors. J Vasc Interv Radiol, 2003, 14: 1267–1274.
6. Teratani T, Yoshida H, Shiina S, *et al*. Radiofrequency ablation for hepatocellular carcinoma in so-called high-risk locations. Hepatology, 2006, 43: 1101–1108.
7. Wong SN, Lin CJ, Lin CC, *et al*. Combined percutaneous radiofrequency ablation and ethanol injection for hepatocellular carcinoma in high-risk locations. AJR Am J Roentgenol, 2008, 190: W187–W195.
8. Kudo M. Radiofrequency ablation for hepatocellular carcinoma: updated review in 2010. Oncology, 2010, 78 (Suppl 1): 113–124.
9. Goldberg SN, Grassi CJ, Cardella JF, *et al*. Image-guided tumor ablation: standardization of terminology and reporting criteria. J Vasc Interv Radiol, 2009, 20 (7 Suppl): S377–S390.
10. Pan HF, Chen XP, Li KY, *et al*. Values of color doppler in predicting the safety of hepatectomy for hepatic cancer. Chin J Gene Surg (Chinese), 2000, 9: 61–63.
11. Yang W, Yan K, Wu GX, *et al*. Radiofrequency ablation of hepatocellular carcinoma in difficult locations: Strategies and long-term outcomes. World J Gastroenterol, 2015, 21: 1554–1566.
12. Dong BW, Liang P, Yu XL, *et al*. Long-term results of percutaneous sonographically-guided microwave ablation therapy of early-stage hepatocellular carcinoma. Natl Med J China (Chinese), 2006, 86: 797–800.
13. Shi J, Sun Q, Wang Y, *et al*. Comparison of microwave ablation and surgical resection for treatment of hepatocellular carcinomas conforming to Milan criteria. J Gastroenterol Hepatol, 2014, 29: 1500–1507.
14. Lu DS, Raman SS, Limanond P, *et al*. Influence of large peritumoral vessels on outcome of radiofrequency ablation of liver tumors. J Vasc Interv Radiol, 2003, 14: 1267–1274.
15. Huang S, Yu J, Liang P, *et al*. Percutaneous microwave ablation for hepatocellular carcinoma adjacent to large vessels: a long-term follow-up. Eur J Radiol, 2014, 83: 552–558.
16. Kawasoe H, Eguchi Y, Mizuta T, *et al*. Radiofrequency ablation with the real-time virtual sonography system for treating hepatocellular carcinoma difficult to detect by ultrasonography. J Clin Biochem Nutr, 2007, 40: 66–72.

17. Jung EM, Schreyer AG, Schacherer D, *et al*. New real-time image fusion technique for characterization of tumor vascularisation and tumor perfusion of liver tumors with contrast-enhanced ultrasound, spiral CT or MRI: first results. Clin Hemorheol Microcirc, 2009, 43: 57–69.
18. Lonardo MT, Cannici F, Turtulici G, *et al*. Intraoperative radiofrequency ablation: intraductal cooling of the main bile ducts for the prevention of heat damage. A case report. Hepatogastroenterlolgy, 2005, 52: 368–370.
19. Ren H, Liang P, Yu X, *et al*. Treatment of liver tumours adjacent to hepatic hilum with percutaneous microwave ablation combined with ethanol injection: a pilot study. Int J Hyperthermia, 2011, 27: 249–254.
20. Ni JY, Sun HL, Chen YT, *et al.* Prognostic factors for survival after transarterial chemoembolization combined with microwave ablation for hepatocellular carcinoma. World J Gastroenterol, 2014, 20: 17483–17490.

**DOI 10.1007/s10330-016-0194-4**
**Cite this article as:** Liu RB, Li KY, Luo HC, *et al*. Ultrasound-guided percutaneous microwave ablation for small liver cancers adjacent to large vessels: long-term outcomes and strategies. Oncol Transl Med, 2017, 3: 57–64.

Oncology and Translational Medicine
DOI 10.1007/s10330-017-0219-9

April 2017, Vol. 3, No. 2, P65–P70

ORIGINAL ARTICLE

# Selective partial salivary glands sparing during intensity-modulated radiation therapy for nasopharyngeal carcinoma*

**Guangjin Yuan[1], Qianwen Li[2] (Co-first author), Shixian Chen[1], Chengwei Zheng[1], Jiang Tang[2], Jiang Hu[3], Ximing Xu[3] (✉)**

[1] Department of Oncology, Nationality Hospital of Qianjiang, Chongqing 409000, China
[2] Cancer Center, The 82nd Hospital of the Chinese People's Liberation Army, Huai'an 223001, China
[3] Cancer Center, Renmin Hospital of Wuhan University, Wuhan 430060, China

## Abstract

**Objective** This study evaluated the dosimetric consequences of selective partial salivary gland sparing during intensity-modulated radiotherapy (IMRT) for patients with nasopharyngeal carcinoma (NPC).

**Methods** Ten patients with NPC were enrolled in the study. Two IMRT plans were produced for each patient: conventional (control) and partial salivary glands-sparing (treatment), with dose constraints to the entire parotid glands or partial salivary glands (including the parotid and submandibular glands, delineated with the adjacent distance of at least 0.5 cm between the glands and PTV, the planning target volume) in planning, respectively. Dosimetric parameters were compared between the two plans, including the $V_{110\%}$, $V_{100\%}$, $V_{95\%}$ (the volume covered by more than 110%, 100%, or 95% of the prescribed dose), $D_{min}$ (the minimum dose) of PTV, homogeneity index (HI), conformity index (CI), and the mean dose and percentage of the volume receiving 30 Gy or more ($V_{30}$) for the parotid glands and submandibular glands.

**Results** Treatment plans had significantly lower mean doses and V30 to both the entire parotid glands and partial parotid glands than those in control plans. The mean doses to the partial submandibular glands were also significantly lower in treatment plans than in control plans. The PTV coverage was comparable between the two plans, as indicated by $V_{100\%}$, $V_{95\%}$, $D_{min}$, CI, and HI. The doses to critical structures, including brainstem and spinal cord, were slightly but not significantly higher in treatment plans than in control plans.

**Conclusion** A selective partial salivary gland-sparing approach reduces the doses to parotid and submandibular glands during IMRT, which may decrease the risk of post-radiation xerostomia while not compromising target dose coverage in patients with NPC.

Received: 3 January 2017
Revised: 13 February 2017
Accepted: 18 March 2017

**Key words:** nasopharyngeal carcinoma; intensity-modulated radiotherapy; selective partial salivary gland sparing

Radiotherapy is one of the main treatments for head and neck cancers, especially nasopharyngeal cancer. During radiotherapy, the salivary glands, parts of which are commonly included in or very close to the target volume, receive a high radiation dose on both sides, which can lead to xerostomia (dry mouth). Xerostomia can produce a number of negative effects on the patient's quality of life, affecting dietary habits, speech, taste, and increasing the risk of oral infections [1]. Intensity-modulated radiotherapy (IMRT) has now become the standard modality of radiotherapy for nasopharyngeal cancer, which may reduce xerostomia by delivering tumoricidal doses to the target volume while sparing normal structures at the same time; however, severe xerostomia is still experienced by many patients (39.3%) after IMRT [2].

Currently, the management of irradiation-induced xerostomia remains largely limited to palliative therapy. Sparing damage to the salivary glands during radiotherapy may be the key to preventing radiation-induced xerostomia. The salivary glands include three pairs of major salivary glands: the parotid,

✉ Correspondence to: Ximing Xu. Email: doxtorxu120@aliyun.com
* Supported by a grant from the Science and Technology Program Project Funds of Qianjiang (No. 2014046).

submandibular, and sublingual glands, as well as numerous minor salivary glands scattered throughout the oral cavity. The parotid gland mainly secretes saliva in stimulated conditions, contributing up to 60% of the total saliva, while the submandibular gland mainly secretes saliva in non-stimulated conditions, producing up to 90% of total saliva under non-stimulated conditions, but only 20%–40% of total saliva in stimulated conditions, while the sublingual gland produce 2%–5% of the total saliva upon stimulation [3]. Both the parotid and the submandibular glands have been shown to be sensitive to radiotherapy ($TD_{50}$, the former equal to 40 Gy and the latter 39 Gy) [4–5], and the mean doses, which represent the threshold for significant salivary flow reduction, are 26 to 39 Gy [6]. Conventionally, the entire parotid glands are contoured as critical structures, and due to parts of the glands being very close to or overlapping with the target volume, the mean dose limitation of less than 26 Gy is hard to achieve in IMRT plans.

In the present study, we developed a selective partial salivary gland-sparing approach during IMRT for nasopharyngeal cancer, which was delineated with the adjacent distance of at least 0.5 cm between the glands and the planning target volume (PTV), and evaluated the dose changes in the salivary glands, target volume, and critical structures.

## Materials and methods

### Patients

From May 2015 to May 2016, 10 patients with histologically proven nasopharyngeal carcinoma treated at Renmin Hospital of Wuhan University were included in this study. All patients had good performance status (WHO 0–1) and received 9-field step-and-shoot IMRT. An informed consent for radiotherapy was signed. Patient characteristics are described in Table 1. The regimen for concurrent chemoradiotherapy was cisplatin 70 mg/m$^2$ every 3 weeks for 1 to 2 cycles.

### Pretreatment evaluation of tumor extent

A thorough pretreatment evaluation of tumor extent was performed for all patients, including a complete history and physical examination, mirror and fiberoptic examination, computerized tomography (CT) with contrast and magnetic resonance imaging (MRI) of the primary site and neck, chest X-ray, and liver sonography. Nasopharyngeal carcinoma was staged in accordance with the Chinese 2008 staging system [7].

### CT simulation and delineation of target volumes and critical structures

Patients were immobilized in a supine and hard palate vertical position with a head support and a custom thermoplastic cast from head to shoulders. A high-resolution planning CT scan (General Electric Medical Systems, USA) was taken with contiguous 5-mm thick slices from the skull vertex down to below the clavicles with the cast on and in the treatment position. The CT images were transferred to a virtual simulation workstation computer for structure delineation. The target volumes and critical structures were contoured on the axial CT slices.

The gross tumor volume (GTV) represented the visible primary tumor and/or enlarged or suspicious lymph nodes identified either clinically or radiographically with MRI and CT. The clinical target volume (CTV) encompassed GTV plus a microscopic disease margin (at least 1.0 cm, except in areas adjacent to critical structures, i.e., brainstem). $CTV_1$ covered CTV and high-risk lymphatic areas, and $CTV_2$ covered lower-risk lymphatic regions. The planning target volume (PTV), $PTV_{nx}$, $PTV_1$, and $PTV_2$, were defined as the CTV (or $CTV_1$, $CTV_2$) plus 2 to 5-mm margins (depending on proximity to critical normal structures) to account for patient setup error.

Critical structures were also contoured on axial CT slices throughout the volume of interest, including the spinal cord, brainstem, eyes, lenses, optic nerves, optic chiasm, pituitary, temporal lobes, parotid glands, temporomandibular joints, and mandible.

**Table 1** Patient characteristics

| Patient | Age (years) | Gender | TNM staging | Concurrent chemotherapy |
|---|---|---|---|---|
| 1 | 60 | Male | $T_4N_1M_0$ | No |
| 2 | 48 | Male | $T_4N_3M_0$ | Yes |
| 3 | 52 | Male | $T_2N_2M_0$ | Yes |
| 4 | 29 | Male | $T_4N_2M_0$ | Yes |
| 5 | 41 | Male | $T_3N_1M_0$ | Yes |
| 6 | 50 | Male | $T_2N_2M_0$ | Yes |
| 7 | 42 | Female | $T_1N_2M_0$ | Yes |
| 8 | 50 | Male | $T_2N_2M_0$ | Yes |
| 9 | 47 | Female | $T_2N_2M_0$ | Yes |
| 10 | 62 | Male | $T_2N_1M_0$ | Yes |

### Delineation of partial salivary glands

Salivary glands include major glands (parotid, submandibular, and sublingual glands) and minor glands (located throughout the oral cavity within the submucosa). According to the target volumes (PTV), partial salivary glands to be spared were delineated with the adjacent distance of at least 0.5 cm between the glands and PTV. Sublingual and minor salivary glands were together regarded as a critical structure "mouth cavity and floor." Fig. 1 illustrates the delineation of partial salivary glands

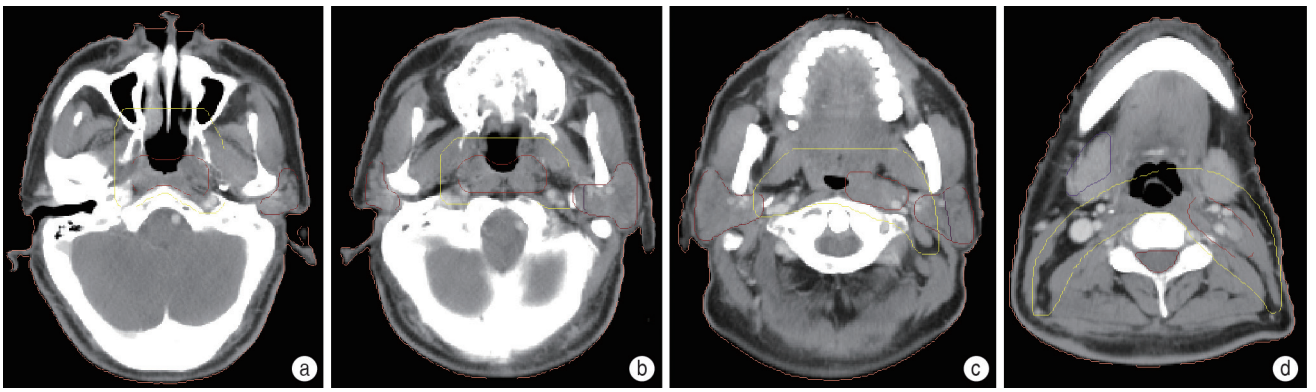


**Fig. 1** Delineation of partial parotid and submandibular glands in a patient with $T_2N_2M_0$ nasopharyngeal carcinoma. GTV, PTV, entire parotid glands, partial parotid or submandibular glands are shown from the middle to the lateral in each CT image. (a) The left partial parotid gland is overlapped with the left parotid gland; (b) The right partial parotid gland is overlapped with the right parotid gland; but the left partial parotid gland is partly overlapped with the left parotid gland; (c) The right and left partial parotid glands are partly overlapped with the right and left parotid glands, respectively; (d) The right partial submandibular gland is delineated, but not the left partial submandibular gland due to too small volume left away from the PTV

in a patient with $T_2N_2M_0$ nasopharyngeal carcinoma.

### Treatment planning

All patients underwent IMRT in 35 fractions, 1 fraction daily, 5 days per week. The following are the prescribed doses: $PTV_{nx}$ (PTV of CTV), 70 Gy; $PTV_1$ (PTV of $CTV_1$), 60 Gy; $PTV_2$ (PTV of $CTV_2$), 50 Gy. The prescription dose is the isodose that encompasses at least 95% of the PTVs. No more than 20% of any PTV will receive 110% of its prescribed dose, no more than 3% of any PTV will receive < 93% of its prescribed dose, and no more than 1% or 1 cubic centimeter of the tissue outside the PTVs will receive > 110% of the dose prescribed to the PTV.

The dose constraints to critical structures were brainstem/pituitary maximum dose 54 Gy, spinal cord maximum dose 45 Gy, optic nerve/chiasm maximum dose 54 Gy, temporal lobes maximum dose 60 Gy, temporomandibular joints maximum dose 50 Gy, mandible maximum dose 60 Gy, eyes mean dose 35 Gy, and lens maximum dose 9 Gy.

Two IMRT plans were created for each patient: conventional (control) and partial salivary gland-sparing (treatment) IMRT. In the treatment IMRT plans, partial salivary glands, including parotid and submandibular glands, were defined as organs at risk (OAR) and incorporated into the IMRT optimization process; but in the control IMRT plans, the entire parotid glands were instead defined as OAR, and submandibular glands were not considered as OAR. The dose constraints for the entire parotid glands were $V_{30}$ (percentage of the volume receiving 30 Gy or more) ≤ 50%; due to a smaller volume as compared with the entire glands and the threshold dose for the recovery potential of the glands, the dose constraints for partial parotid glands were $V_{26}$ ≤ 30%. The dose constraints for the partial submandibular glands were $V_{35}$ ≤ 50%. All the plans were created by the same physicist.

### Dosimetric comparisons

For PTV, the volume covered by more than 110%, 100%, or 95% of the prescribed dose ($V_{110\%}$, $V_{100\%}$, $V_{95\%}$), and the $D_{min}$ (the minimum dose) were compared between the control and treatment IMRT plans. The differences in the homogeneity and conformity of PTV were evaluated between the two plans. The homogeneity index (HI) was calculated with $HI = (D_{max} - D_{min})/D_{mean}$, where $D_{max}$ is the maximum dose, $D_{min}$ the minimum dose, and $D_{mean}$ the mean dose within the target volume [8]. The lower the value of HI is, the better the homogeneity will be. The conformity index (CI) of PTV was defined as the ratio between the volume covered by the prescribed dose ($V_{PD}$) and the volume of the PTV ($V_{PTV}$): $CI = V_{PD}/V_{PTV}$. The value of CI ranges from 0 to 1, and the closer to 1, the better [9].

For OAR, the mean dose and $V_{30}$ for parotid glands, the mean dose for submandibular glands, and the maximum dose ($D_{max}$) to the spinal cord, brainstem, and pituitary were also compared.

### Statistical analysis

Data were analyzed using SPSS 14.0 software, and a Wilcoxon matched-pairs test was used. A probability value of ≤ 0.05 was considered significant.

## Results

### Evaluation of dose to salivary glands

Compared with control plans, treatment plans had significantly lower mean doses and $V_{30}$ to both the entire

parotid glands and partial parotid glands ($P < 0.05$; Table 2). The mean doses to the partial submandibular glands were also significantly lower in the treatment plans than in the control plans ($P < 0.05$).

### Evaluation of dose to targets and critical structures

As shown in Table 3, the $V_{100\%}$, $V_{95\%}$, and the $D_{min}$ for the PTV ($PTV_{nx}$ or $PTV_1$) were comparable between the control and treatment plans. Furthermore, there was no significant difference in the HI and CI of the PTV between the two plans. For the hot spot, the $V_{110\%}$ of the $PTV_{nx}$ in the treatment plans was slightly higher but not significantly than that in the control plans ($P > 0.05$).

The doses to critical structures, including the brainstem and spinal cord, were slightly but not significantly increased in treatment plans as compared with control plans ($P > 0.05$).

## Discussion

The parotid and submandibular glands produce up to 90% of total saliva under stimulated or non-stimulated conditions; therefore, they are the main salivary glands to be spared to prevent xerostomia after radiotherapy. Studies have shown that a mean dose of less than 26–39 Gy to the parotid or submandibular gland can preserve their function substantially after radiotherapy [6]. The parotid and submandibular glands are parallel organs. The volume of the contralateral parotid gland receiving > 40 Gy ($V_{40}$) being less than 33% has been reported to be satisfactory for complete salivary recovery at 24 months after IMRT [10]. Furthermore, the influence of the mean doses to the contralateral submandibular and parotid glands upon the recovery of saliva output has been shown to be equivalent to that of the mean $V_{30}$ to the glands [11]. These facts suggest that if parts of the glands are sufficiently protected from irradiation-induced damage, their function can still be well preserved and xerostomia may be prevented.

During IMRT planning, the entire parotid glands are conventionally contoured as critical structures. However, parts of these glands are very close to or even overlap with the target volume, which makes it difficult to protect the glands during dose optimization. As a result, the mean dose to the parotid glands usually exceeds 32 Gy [2]. In the present study, we developed a selective partial salivary gland-sparing approach in IMRT for nasopharyngeal cancer, which was delineated with an adjacent distance of at least 0.5 cm between the glands and the target volume. The entire parotid glands or partial salivary glands were incorporated into the IMRT optimization process in

**Table 2** Doses to the salivary glands in two plans

| Variable | Control plan | Treatment plan | *P* |
|---|---|---|---|
| Right parotid | | | |
| Mean (Gy) | 37.9 ± 5.5 | 33.8 ± 5.4 | 0.01 |
| Range | 28.3–48.8 | 25.5–45.2 | |
| $V_{30}$ (%) mean | 43.7 ± 10.5 | 33.9 ± 11.4 | 0.02 |
| Range | 33.8–58.5 | 26.1–41.2 | |
| Partial right parotid | | | 0.01 |
| Mean (Gy) | 33.1 ± 5.2 | 29.1 ± 5.1 | |
| Range | 23.5–43.4 | 19.2–39.4 | |
| Left parotid | | | |
| Mean (Gy) | 36.8 ± 4.3 | 33.2 ± 5.0 | 0.01 |
| Range | 27.9–48.5 | 24.2–43.8 | |
| $V_{30}$ (%) mean | 44.1 ± 11.4 | 34.8 ± 10.6 | 0.02 |
| Range | 34.2–59.3 | 27.3–41.8 | |
| Partial left parotid | | | |
| Mean (Gy) | 33.1 ± 5.2 | 29.1 ± 5.1 | 0.01 |
| Range | 23.5–43.4 | 19.2–39.4 | |
| Partial submandibular | | | |
| Mean (Gy) | 45.6 ± 8.3 | 35.6 ± 7.5 | < 0.01 |
| Range | 39.2–55.1 | 28.8–44.1 | |

**Table 3** Dose changes in target volume and critical structures in two plans

| Variable | Control plan | Treatment plan | *P* |
|---|---|---|---|
| $PTV_{nx}$ $V_{110}$ (%) | | | |
| Mean | 2.4 ± 2.2 | 3.5 ± 4.5 | 0.09 |
| Range | 0.0–6.0 | 0.0–9.2 | |
| $PTV_{nx}$ $V_{100}$ (%) | | | |
| Mean | 98.5 ± 0.7 | 98.6 ± 0.6 | 0.20 |
| Range | 97.8–100.0 | 97.9–100.0 | |
| $PTV_{nx}$ $V_{95}$ (%) | | | |
| Mean | 99.9 ± 0.2 | 99.9 ± 0.2 | 0.20 |
| Range | 99.3–100.0 | 99.2–100.0 | |
| $PTV_1$ $D_{min}$ | | | |
| Mean | 44.6 ± 8.5 | 46.5 ± 7.4 | 0.20 |
| Range | 36.6–57.1 | 38.8–58.2 | |
| HI | | | |
| Mean | 0.15 ± 0.05 | 0.16 ± 0.06 | 0.10 |
| Range | 0.10–0.22 | 0.11–0.23 | |
| CI | | | |
| Mean | 1.20 ± 0.07 | 1.18 ± 0.08 | 0.10 |
| Range | 1.14–1.28 | 1.11–1.26 | |
| Brainstem $D_{max}$ | | | |
| Mean (Gy) | 42.8 ± 5.2 | 43.6 ± 5.3 | 0.09 |
| Range | 39.8–47.6 | 41.2–49.1 | |
| Spinal cord $D_{max}$ | | | |
| Mean (Gy) | 36.5 ± 5.2 | 38.7 ± 5.5 | 0.08 |
| Range | 34.5–43.8 | 37.6–44.2 | |
| Right lens $D_{max}$ | | | |
| Mean (Gy) | 2.4 ± 1.0 | 2.4 ± 1.1 | 0.10 |
| Range | 1.8–3.7 | 1.7–3.9 | |
| Right lens $D_{max}$ | 2.3 ± 1.0 | 2.2 ± 1.2 | 0.10 |
| Mean (Gy) | | | |
| Range | 1.7–4.1 | 1.8–4.0 | |

the control or treatment plans. The results showed that treatment plans had significantly lower mean doses and $V_{30}$ to both the entire parotid glands and partial parotid glands than those in control plans. However, the PTV coverage was comparable between the two plans, as indicated by $V_{100\%}$, $V_{95\%}$, $D_{min}$, CI, and HI. The doses to critical structures, including brainstem and spinal cord, were slightly but not significantly increased in treatment plans as compared with control plans. Zhang *et al* reported that the superficial parotid lobe (partial parotid gland)-sparing delineation approach can lower the mean dose and $V_{30}$ to both the entire parotid and superficial parotid lobe in patients with nasopharyngeal cancer without affecting dose distributions for targets [12], which is consistent with our present study. However, superficial parotid lobe-sparing delineation may exclude some parotid glands of the deep lobe, which may be sufficiently far away from the target volume to be spared in IMRT.

Submandibular glands produce up to 90% of the unstimulated saliva, which contains mucins and influences the degree of sensation of mouth dryness. Therefore, maintenance of their normal function may be useful to reduce radiotherapy xerostomia. Surgical transfer of a submandibular gland to the submental space prevents xerostomia after radiation therapy for head and neck cancers [13–14]. However, the submandibular glands are very close to the level II nodes, which are the common site of nodal metastasis in patients with nasopharyngeal cancer, making their sparing technically demanding. The mean dose to the submandibular glands usually exceeds 39 Gy [15], which is the highest threshold dose to preserve their function after radiotherapy [5].

Conventionally, the submandibular glands are given no dose constraint in the IMRT plan. In the present study, a selective partial submandibular gland-sparing approach was developed, which was delineated with the adjacent distance of at least 0.5 cm between the glands and the target volume. The results showed that the mean dose to the partial submandibular glands was significantly lower in the treatment plans than in the control plans. Restricting the dose to the submandibular glands may affect the dose distribution to PTV around the gland area. However, as stated above, the PTV coverage was not compromised in the treatment plans as compared with the control plans in the current study. Submandibular gland sparing with IMRT has been reported to be feasible in selected patients with head and neck cancer [15–16], and have a low risk of cancer recurrence in the vicinity of the spared glands [17].

In the present study, several patients with advanced T-stage ($T_3$ or $T_4$) were included. As stated above, the dosimetric parameters for PTV and critical structures (e.g., brainstem, spinal cord) in treatment plans for these patients were comparable to those in control plans, although some parameters (e.g., $V_{110\%}$ of the PTV) were slightly higher but not significantly, suggesting that the selective partial salivary gland-sparing approach is suitable for these patients with advanced T-stage. However, a similar partial salivary gland-sparing (i.e., the superficial parotid lobe sparing) approach was reported to be only indicated for patients with T1-3 NPC, arguing that T4 patients had increased $V_{110\%}$ of the PTV and dose to brainstem [12]. The reason for this discrepancy may be due to the different delineation of the spared salivary glands. In our study, the delineation of the spared salivary glands was dependent upon PTV to have an adjacent distance of at least 0.5 cm between the glands and PTV. Therefore, enough distance between the spared salivary glands and PTV can be assured to protect the glands without compromising the doses to PTV or other critical structures.

However, in the superficial parotid lobe–sparing approach, locally advanced tumor may extend close to the spared glands, which may affect the doses to PTV or other critical structures. In fact, exclusion of sparing of the deep lobe of the parotid glands (i.e., sparing the superficial lobe only) was reported to improve the dose coverage of PTV (preventing dose decreases to the lymphatic region) in IMRT for head and neck cancers, and this approach did not rule out patients with advanced T-stage [18]. In addition, in a study of recovery of salivary function after IMRT with bilateral superficial lobe parotid sparing versus contralateral parotid-sparing, patients with locally advanced head and neck cancers were enrolled, and the results showed that bilateral superficial lobe parotid-sparing reduces the risk of developing high-grade subjective xerostomia [19].

In conclusion, a selective partial salivary gland-sparing approach reduces the doses to parotid and submandibular glands during IMRT, which may decrease the risk of post-radiation xerostomia, while not compromising target dose coverage in patients with NPC. The selective partial salivary gland-sparing approach also has the potential to be applied to other head and neck cancers to achieve salivary gland sparing during IMRT.

## Conflicts of interest

The authors indicated no potential conflicts of interest.

## References

1. Dirix P, Nuyts S, Van den Bogaert W. Radiation-induced xerostomia in patients with head and neck cancer: a literature review. Cancer, 2006, 107: 2525–2534.
2. Kam MK, Leung SF, Zee B, *et al*. Prospective randomized study of intensity-modulated radiotherapy on salivary gland function in early-stage nasopharyngeal carcinoma patients. J Clin Oncol, 2007, 25: 4873–4879.
3. Cheng SC, Wu VW, Kwong DL, *et al*. Assessment of post-radiotherapy

salivary glands. Br J Radiol, 2011, 84: 393–402.
4. Dijkema T, Raaijmakers CP, Ten Haken RK, *et al*. Parotid gland function after radiotherapy: the combined michigan and utrecht experience. Int J Radiat Oncol Biol Phys, 2010, 78: 449–453.
5. Murdoch-Kinch CA, Kim HM, Vineberg KA, *et al*. Dose-effect relationships for the submandibular salivary glands and implications for their sparing by intensity modulated radiotherapy. Int J Radiat Oncol Biol Phys, 2008, 72: 373–382.
6. Vissink A, Mitchell JB, Baum BJ, *et al*. Clinical management of salivary gland hypofunction and xerostomia in head-and-neck cancer patients: successes and barriers. Int J Radiat Oncol Biol Phys, 2010, 78: 983–991.
7. Zong J, Huang Q, Guo Q, *et al*. Evolution of the Chinese staging system for nasopharyngeal carcinoma. Chin Clin Oncol, 2016, 5: 19.
8. Runxiao L, Yankun C, Lan W. A pilot study of volumetric-modulated arc therapy for malignant pleural mesothelioma. J Appl Clin Med Phys, 2016, 17: 5980.
9. Moorthy S, Murthy PN, Majumdar SKD, *et al*. Dosimetric characteristics of IMRT versus 3DCRT for intact breast irradiation with simultaneous integrated boost. Austral-Asian J of Cancer, 2012, 11: 221–230.
10. Ortholan C, Chamorey E, Benezery K, *et al*. Modeling of salivary production recovery after radiotherapy using mixed models: determination of optimal dose constraint for IMRT planning and construction of convenient tools to predict salivary function. Int J Radiat Oncol Biol Phys, 2009, 73: 178–186.
11. Wang ZH, Yan C, Zhang ZY, *et al*. Impact of salivary gland dosimetry on post-IMRT recovery of saliva output and xerostomia grade for head-and-neck cancer patients treated with or without contralateral submandibular gland sparing: a longitudinal study. Int J Radiat Oncol Biol Phys, 2011, 81: 1479–1487.
12. Zhang HB, Lu X, Huang SM, *et al*. Superficial parotid lobe-sparing delineation approach: a better method of dose optimization to protect theparotid gland in intensity-modulated radiotherapy for nasopharyngeal carcinoma. Curr Oncol, 2013, 20: e577–584.
13. Al-Qahtani K, Hier MP, Sultanum K, *et al*. The role of submandibular salivary gland transfer in preventing xerostomia in the chemoradiotherapy patient. Oral Surg Oral Med Oral Pathol Oral Radiol Endod, 2006, 101: 753–756.
14. Liu XK, Su Y, Jha N, *et al*. Submandibular salivary gland transfer for the prevention of radiation-inducedxerostomia in patients with nasopharyngeal carcinoma: 5-Year outcomes. Head Neck, 2011, 33: 389–395.
15. Huang L, Zhang W, Zhuang T, *et al*. Submandibular gland sparing in intensity-modulated radiotherapy for N0-stage nasopharyngeal carcinoma. Br J Radiol, 2014, 87: 20130651.
16. Saarilahti K, Kouri M, Collan J, *et al*. Sparing of the submandibular glands by intensity modulated radiotherapy in the treatment of head and neck cancer. Radiother Oncol, 2006, 78: 270–275.
17. Collan J, Kapanen M, Mäkitie A, *et al*. Submandibular gland-sparing intensity modulated radiotherapy in the treatment of head and neck cancer: sites of locoregional relapse and survival. Acta Oncol, 2012, 51: 735–742.
18. Cetin E, Ozturk AS, Orhun H, *et al*. Is sparing the deep lobes of parotid gland necessary on intensity modulated radiation therapy of head and neck cancers? Int J Hematol Oncol, 2012, 22: 73–76.
19. Miah AB, Gulliford SL, Morden J, *et al*. Recovery of Salivary Function: Contralateral Parotid-sparing Intensity-modulated Radiotherapy versus Bilateral Superficial Lobe Parotid-sparing Intensity-modulated Radiotherapy. Clin Oncol (R Coll Radiol), 2016, 28: e69–76.

**DOI 10.1007/s10330-017-0219-9**
**Cite this article as:** Yuan GJ, Li QW, Chen SX, *et al*. Selective partial salivary glands sparing during intensity-modulated radiation therapy for nasopharyngeal carcinoma. Oncol Transl Med, 2017, 3: 65–70.

Oncology and Translational Medicine
DOI 10.1007/s10330-016-0200-0

April 2017, Vol. 3, No. 2, P71–P76

ORIGINAL ARTICLE

# BRAF V600E/TERT promoter mutations and NIS/TSHR expression in differentiated thyroid carcinoma and their clinical significance*

**Xiaoting Ru[1], Qinjiang Liu[2] (✉), Haihong Zhou[3], Rong Yang[4], Lie Bao[1]**

[1] College of Life Sciences, Lanzhou University, Lanzhou 730000, China
[2] Department of Head and Neck Surgery, Gansu Province Tumor Hospital, Lanzhou 730050, China
[3] Translational Medicine Research Center, Gansu Province Tumor Hospital, Lanzhou 730050, China
[4] Department of Pathology, Gansu Province Tumor Hospital, Lanzhou 730050, China

## Abstract

**Objective** Telomerase reverse transcriptase (TERT) promoter mutations have recently been described in thyroid carcinoma. The purpose of this study was to investigate the clinical significance of (v-raf murine sarcoma viral oncogene homolog B1) BRAF V600E and TERT promoter mutations in differentiated thyroid carcinoma (DTC). The relationship between the two mutations and NIS/TSHR expression was also analyzed.

**Methods** We have detected BRAF V600E and TERT promoter mutations by direct sequencing and NIS/TSHR expression by immunohistochemistry in 229 cases of DTC, 52 cases of benign nodular goiter, and 31 cases of normal thyroid tissue.

**Results** The BRAF V600E mutation was detected in 142 (62.0%) of 229 cases of DTC [141 cases of papillary thyroid carcinoma (PTC) and 1 case of follicular thyroid carcinoma (FTC)]. TERT promoter mutations were detected in 18 (7.9%) of 229 cases of DTC (14 cases of PTC and 4 cases of FTC), including the mutations C228T (0.9%) and C250T (7.0%), which were mutually exclusive. Moreover, 11 (61.1%) cases also harbored the BRAF V600E mutation, which was not associated with gender, age, tumor size, lymph node metastasis, and recurrence risk stratification ($P$ >0.05). The rate of TERT promoter mutation was higher in males, age ≥45, and in the middle/high-risk group ($P$ <0.05), and the rate of simultaneous BRAF V600E and TERT promoter mutations were higher in the middle/high-risk group ($P$ <0.05). In addition, NIS positive rate in the concurrent BRAF V600E and TERT promoter mutation group (45.5 %) was lower than in other groups (that is, the DTC group with BRAF V600E or TERT promoter mutations (55.1%), the DTC group with no BRAF V600E or TERT promoter mutation (57.5%), the nodules and normal group (75.9%); $|r| = 0.171$, $P = 0.002$).

**Conclusion** TERT promoter mutations were lower in patients with DTC, with the C250T mutation being the most common. The detection of BRAF V600E mutation combined with TERT promoter mutations was instructive for the prognosis assessment and treatment of DTC.

Received: 17 October 2016
Revised: 15 November 2016
Accepted: 10 December 2016

**Key words:** differentiated thyroid carcinoma (DTC); BRAF V600E; TERT promoter mutations; sodium iodide symporter; thyroid stimulating hormone receptor

Thyroid cancer is a common endocrine malignancy, and differentiated thyroid carcinoma (DTC), which includes papillary thyroid carcinoma (PTC) and follicular thyroid carcinoma (FTC), is the most common. In recent years, the global incidence of thyroid cancer has gradually increased. In China, thyroid cancer has the fastest growing incidence. Surgically, radioactive $^{131}I$ and thyroid-stimulating hormone (TSH) suppression therapies have been used for the treatment of DTC, with a 10-year survival rate over 95% [1]; however, the recurrence rate of DTC is about 30% [2]. Therefore, it is necessary to control the recurrence of DTC, but there is no precise biological

✉ Correspondence to: Qinjiang Liu. Email: LIUQJ99@126.com
* Supported by a grant from the Beijing Medical Awards Foundation (No. YJHYXK YJJ-206).

indicator to monitor the recurrence of DTC.

The BRAF V600E mutation is the most important genetic alteration in DTC and plays an important role in the tumor oncogenic mechanism. With the improvement of molecular biology techniques, the BRAF V600E mutation detection rate gradually increases in DTC. However, the association between the BRAF V600E mutation and the prognosis of DTC is a controversial subject [3]. Telomerase reverse transcriptase (TERT) is the catalytic subunit of the telomerase and also its active part, and the TERT promoter is the regulatory region of TERT. TERT promoter mutations have been found in a variety of tumors [4], including thyroid carcinomas, and they have become a hot topic in the prognostic assessment of thyroid cancer. Recently, some studies suggested that the BRAF V600E mutation teams up with TERT promoter mutations to enhance the aggressiveness of DTC [5].

Radioactive $^{131}$I therapy has become an important treatment for DTC, but some patients with DTC have shown iodine resistance and poor response to radioactive $^{131}$I therapy. Some studies revealed that this might be related to the sodium iodide symporter (NIS) and TSH receptor (TSHR), which participate in iodine metabolism. Most studies have found that NIS expression in thyroid cancers is reduced or absent [6]. Moreover, irregular expression of NIS in thyroid cancer may be associated with the BRAF V600E mutation [7]. Previous studies demonstrated that TSHR is involved in the NIS expression level and transport to the cell membrane [8].

In China, the DTC incidence has gradually increased, especially in the western region with a poor environment. Therefore, we have detected BRAF V600E and TERT promoter mutations, as well as NIS and TSHR expression, in the hope of clarifying the prognosis assessment of DTC through multiple molecular markers and providing a theoretical basis for the molecular diagnosis and treatment of DTC.

## Materials and methods

### Thyroid surgical samples

We studied 229 surgically removed thyroid tumors from patients with DTC (163 females and 66 males) of 46 ± 12.8 years of age (mean ± SD), including 216 patients with PTC and 13 patients with FTC, as well as 52 patients with benign nodular goiter and 31 normal thyroid tissue. All thyroid tumors and nodular goiters were histologically verified. Based on the recurrence risk stratification standards described in 2015 American Thyroid Association Management Guidelines for Adult Patients with Thyroid Nodules and Differentiated Thyroid Cancer [9], 99 cases were assigned to the low-risk group and 130 cases to the middle/high-risk group. All surgical samples were collected from October 2014 to January 2016 at the Department of Head and Neck Surgery in Gansu Province Tumor Hospital. The Ethics Committee of Gansu Province Tumor Hospital approved this study, and all surgical sampling has received consent from the patients and their families.

### DNA extraction

Neutral formalin-fixed, paraffin-embedded specimens were cut into 5–10 μm thick slices, and submitted for routine HE staining and identification of tumor cell content by two pathologists. DNA was extracted with the FFPE DNA Kit (Omega, USA), according to the step-by-step manufacturer's instructions, and the concentration and purity of the product was measured with ultrafine spectrophotometer ND-2000, the OD260/280 ratio in the range of 1.8 to 2.0. The extracted DNA was stored in a refrigerator (–20°C).

### BRAF V600E and TERT promoter mutation analysis

PCR assays were carried out using PrimeSTAR® HS DNA Polymerase (TaKaRa, Japan). The PCR reaction system was as follows: 10 μL of 5× PrimeSTAR Buffer, 4 μL of deoxy-ribonucleoside triphosphate (dNTP) (2.5 mM), 1 μL of forward/reverse primer, < 200 ng of DNA template, 0.5 μL of polymerase, and water to 50 μL. The PCR conditions were set according to the TM value of synthetic primers, and a preliminary experiment determined the number of cycles and the annealing temperature. BRAF V600E was amplified by PCR using the following primers: 5′-ACATTTCAAGC CCCAAAAATCTT-3′, 5′-CATCTCAGGGCCAAAAATTTAATC-3′. The PCR conditions included an initial denaturation step at 95°C for 5 min, followed by 40 denaturation cycles at 95°C for 30 s, annealing at 59°C for 30 s, elongation at 72°C for 30 s, a final elongation step at 72°C for 10 min, and cooling down to 4°C . The TERT promoter was amplified by PCR using the following primers: 5′-ACCCGTCCTGCCCCTTCA-3′, 5′-GGCAGCACCTCGCGGTAGT-3′. The PCR conditions included an initial denaturation step at 95°C for 5 min, followed by 40 denaturation cycles at 95°C for 30 s, annealing at 53°C for 30 s, elongation at 72°C for 30 s, a final elongation step at 72°C for 10 min, and cooling down to 4°C. Agarose gel electrophoresis was used to detect the amplification quality of PCR products (ChemiDoc™ XRS+), and the high-quality PCR product was subjected to DNA sequencing (Jinzhiwei Biotechnology, China).

### Immunohistochemistry

Neutral formalin-fixed, paraffin-embedded specimens were cut into 4-μm thick slices, and sections were baked at 60°C overnight. Sections were deparaffinized, and antigen retrieval (high pressure) was performed by using Antigen Unmasking Solution (citrate buffer, Zhongshan

Goldbridge Biotechnology, China). After 3 washes in Phosphate buffer saline (PBS), the sections were blocked using an animal serum for 15 min, followed by sequential incubations in 1:200 rabbit anti-human NIS/TSHR antibody (Zhongshan Goldbridge Biotechnology, China) at 37°C for 2 h and further washes in PBS. Sections were then incubated with a biotinylated secondary antibody for 15 min and washed with PBS. The sections were incubated with a horseradish peroxidase complex for 15 min and washed with PBS. Finally, the peroxidase substrate diaminobenzidine (DAB) was added to stain the sections, followed by washing with tap water. A semi-quantitative analysis was used to evaluate the immunohistochemistry results [10].

### Statistical analysis

IBM SPSS Statistics 22.0 was used to analyze the data. Continuous data were summarized as mean ± SD or range. Categorical data were expressed as numbers and percentages or ratios. Pearson chi-square tests or Fisher exact test were used for the significance analysis. $P$ value <0.05 was considered to be significant, and Spearman rank correlation analysis was used to determine the positive rate of NIS/TSHR between groups, $|r| \in [0.1,1]$, $P$ <0.05.

## Results

### BRAF V600E and TERT promoter mutations in DTC

The BRAF V600E mutation was detected in 142 (62.0%) of 229 cases with DTC, including 141 cases of PTC and 1 case of FTC. TERT promoter mutations were detected in 18 (7.9%) of 229 cases of DTC (14 cases of PTC and 4 cases of FTC), with the mutation C250T in 16 cases (7.0%) vs. C228T in 2 cases (0.9%), and both mutations were mutually exclusive. Moreover, 11 (61.1%) cases also harbored the BRAF V600E mutation out of the 18 cases with TERT promoter mutation (Fig. 1). None of the 52 benign nodular goiters and 31 normal thyroid tissue harbored BRAF V600E and TERT promoter mutations.

### Relationship of BRAF V600E and TERT promoter mutations with DTC clinicopathologic features

The BRAF V600E mutation was not associated with gender ($P$ = 0.781), age ($P$ = 0.786), tumor size ($P$ = 0.461), lymph node metastasis ($P$ = 0.408), and recurrence risk stratification ($P$ = 0.123). TERT promoter mutations were associated with gender (females 15.2% vs. males 4.9%, $P$ = 0.009), age (older age 11.6% vs. younger age 3.0%, $P$ = 0.016), and recurrence risk stratification (middle/high-risk group 11.5% vs. low-risk group 3.0%, $P$ = 0.018). Concurrent BRAF V600E and TERT promoter mutations

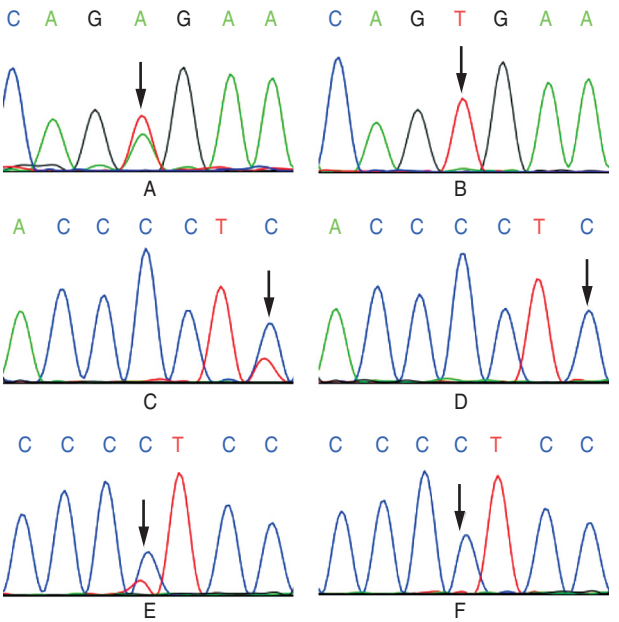


**Fig. 1** BRAF V600E and TERT promoter mutations Sequencing. (a) BRAF V600E mutation; (b) BRAF V600E Wild-Type; (c) TERT promoter C228T mutation; (d)TERT promoter C228T Wild-Type; (e) TERT promoter C250T mutation; (f) TERT promoter C250T Wild-Type

were associated with lymph node metastasis (N1 8.3% vs. N0 1.7%, $P$ = 0.018) and recurrence risk stratification (middle/high-risk group 7.7% vs. low-risk group 1.0%, $P$= 0.019; Table 1).

### Relationship of BRAF V600E and TERT C228T mutations with NIS/TSHR expression

NIS/TSHR immunohistochemical staining (in brown) was located in the cytoplasm and/or the cell membrane (Fig. 2). NIS positive rates of the DTC group with concurrent BRAF V600E and TERT promoter mutations, the DTC group with BRAF V600E or TERT promoter mutations, the DTC group with no BRAF V600E or TERT promoter mutation, the benign nodule goiter group, and the normal thyroid tissue group were 45.5%, 55.1%, 57.5%, and 75.9%, respectively. Moreover, in the concurrent BRAF V600E and TERT promoter mutation group, NIS positive rate was lower than in the other three groups ($|r|$ = 0.171, $P$ = 0.002; Table 2). However, there was no correlation between TSHR expression and the two mutations.

## Discussion

More than one gene was involved in the occurrence and development of DTC. The BRAF V600E mutation is one of the most common mutations in DTC (29%–83%), and it did not occur in benign nodules [11]. The BRAF V600E mutation was also the first genetic mutation detected in

**Table 1** Relationship of BRAF V600E and TERT promoter Mutations With Clinicopathologic features of DTC

| Features | BRAF V600E (*n*, %) | | *P* | TERT promoter (*n*, %) | | *P* | BRAF + TERT (*n*, %) | | *P* |
|---|---|---|---|---|---|---|---|---|---|
| | Mutation *n* = 142 | Wide-Type *n* = 87 | | Mutation *n* = 18 | Wide-Type *n* = 211 | | Mutation *n* = 11 | Wide-Type *n* = 218 | |
| Gender | | | 0.781 | | | 0.009* | | | 0.054 |
| Male | 40 (60.6) | 26 (39.4) | | 10 (15.2) | 56 (84.8) | | 6 (9.1) | 60 (90.9) | |
| Female | 102 (62.6) | 61 (37.4) | | 8 (4.9) | 155 (95.1) | | 5 (3.1) | 158 (96.9) | |
| Age (years) | | | 0.786 | | | 0.016* | | | 0.261 |
| <45 | 63 (63.0) | 37 (37.0) | | 3 (3.0) | 97 (97.0) | | 3 (3.0) | 97 (97.0) | |
| ≥45 | 79 (61.2) | 50 (38.8) | | 15 (11.6) | 114 (88.4) | | 8 (6.2) | 121 (93.8) | |
| Size (cm) | | | 0.461 | | | 0.546 | | | 0.790 |
| < 2 | 16 (76.2) | 5 (23.8) | | 2 (9.5) | 19 (90.5) | | 1 (4.8) | 20 (95.2) | |
| 2–4 | 62 (62.0) | 38 (38.0) | | 6 (6.0) | 94 (94.0) | | 4 (4.0) | 96 (96.0) | |
| ≥ 4 | 64 (65.3) | 34 (34.7) | | 10 (10.2) | 88 (89.8) | | 6 (6.1) | 92 (93.9) | |
| LN metastasis | | | 0.408 | | | 0.217 | | | 0.018* |
| N0 | 72 (59.5) | 49 (40.5) | | 7 (5.8) | 114 (94.2) | | 2 (1.7) | 119 (98.3) | |
| N1 | 70 (64.8) | 38 (35.2) | | 11 (10.2) | 97 (89.8) | | 9 (8.3) | 99 (91.7) | |
| Recurrence risk stratification | | | 0.123 | | | 0.018* | | | 0.019* |
| Low | 67 (67.7) | 32 (32.3) | | 3 (3.0) | 96 (97.0) | | 1 (1.0) | 98 (99.0) | |
| Middle/high | 75 (57.7) | 55 (42.3) | | 15 (11.5) | 115 (88.5) | | 10 (7.7) | 120 (92.3) | |

Note: * $P < 0.05$

**Table 2** NIS、TSHR expression in groups

| Groups | NIS (*n*, %) | | *r* | *P* | TSHR (*n*, %) | | *r* | *P* |
|---|---|---|---|---|---|---|---|---|
| | Positive | Negative | | | Positive | Negative | | |
| N | 63 (75.9) | 20 (24.1) | | | 38 (45.8) | 45 (54.2) | | |
| Mutation 0 | 46 (57.5) | 34 (42.5) | | | 22 (27.5) | 58 (72.5) | | |
| Mutation 1 | 76 (55.1) | 62 (44.9) | | | 68 (49.3) | 70 (50.7) | | |
| Mutation 2 | 5 (45.5) | 6 (54.5) | –0.171* | 0.002* | 3 (27.3) | 8 (72.3) | 0.042 | 0.462 |

Note: $|r| \in [0.1,1]$, * $P$ <0.05; N: Benign nodular goiter and Normal thyroid tissue; Mutation 0: None of BRAF V600E and TERT promoter mutation; Mutation 1: BRAF V600E or TERT promoter mutations; Mutation 2: Both BRAF V600E and TERT promoter mutations

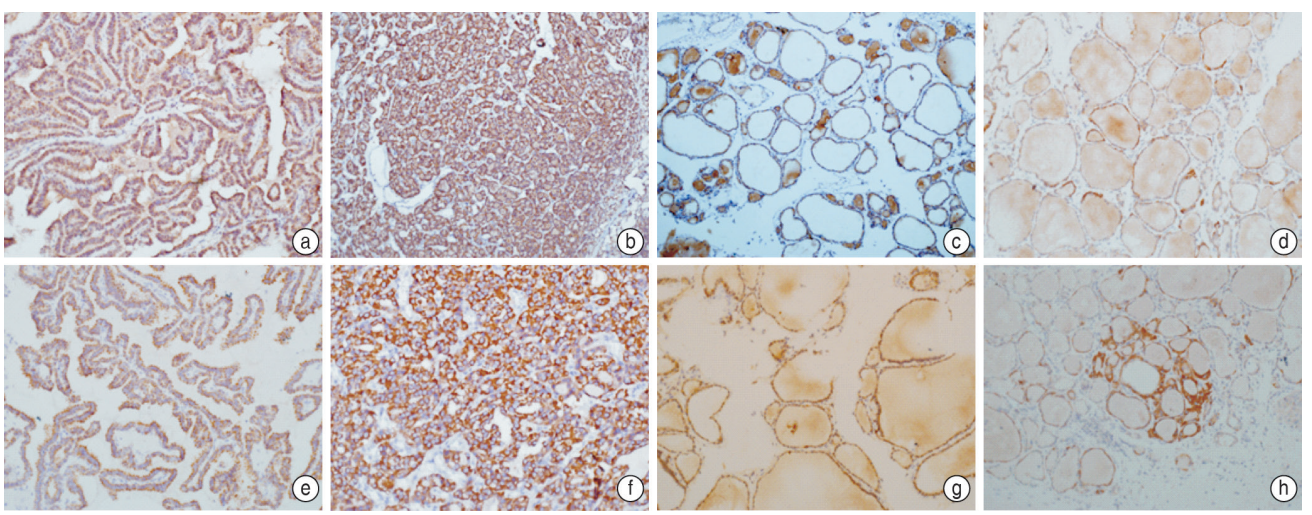


**Fig. 2** NIS, TSHR Immunohistochemistry (SP × 200). (a) PTC showing NIS immunostaining; (b) FTC showing NIS immunostaining; (c) Benign nodular goiter showing NIS immunostaining; (d) Normal thyroid tissue showing NIS immunostaining; (e) PTC showing TSHR immunostaining; (f) FTC showing TSHR immunostaining; (g) Benign nodular goiter showing TSHR immunostaining; (h) Normal thyroid tissue showing TSHR immunostaining

DTC, and most of the researchers working on the prognosis of patients with DTC. Some studies suggested that BRAF V600E mutations were associated with extrathyroidal invasion, lymph node metastasis, and other characteristics related to invasiveness [12–13]. However, recent studies suggested that BRAF V600E mutations were associated with recurrence [14]. Currently, there is still a controversy on BRAF V600E mutation and the prognosis of DTC. TERT promoter mutations have recently been reported in human cancer, are considered a new genetic mechanism, and are involved in the occurrence and development of DTC. Other studies have reported that TERT promoter mutations occurred for 10–13% of the mutations in DTC, and are associated with tumor size, vascular invasion, high TNM stage (and), recurrence, and distant metastasis [15–17]. Specifically, the coexistence of TERT promoter and BRAF V600E mutations presented a more aggressive cancer and higher recurrence rate [18]. However, Melo *at al* [19] found that the concurrence or coexistence of TERT and BRAF V600E mutations was not associated with increased aggressiveness or worse outcome in comparison with the presence of TERT mutations alone. These conflicting results might also reflect the role of the tumor microenvironment.

Our data show that BRAF V600E mutation rate was 62.0% in DTC (142/229), including 65.3% (141/216) in PTC and 7.7% (1/13) in FTC. The mutation rate of TERT promoter was 7.9% (18/229): C250T was 7.0% (16/229), and C228T was 0.9% (2/229), with both mutations mutually exclusive. Surprisingly, the C250T mutation was more common than C228T, contrary to a previous report [15]. The low frequency of TERT promoter mutations in our study might be one of the reasons behind C250T mutation prevalence. The second possible reason is the geographic/ethnic difference.

Our study found that the BRAF V600E mutation was not associated with gender, age, tumor size, lymph node metastasis, and recurrence risk stratification. Kim *et al* [20] studies have also failed to establish a relationship between BRAF V600E mutation and the prognostic of patients with DTC. However, TERT promoter mutations were associated with gender (males), age (≥45), recurrence risk stratification (middle/high-risk group), and concurrent BRAF V600E and TERT promoter mutations were associated with lymph node metastasis (N1) and recurrence risk stratification (middle/high-risk group). In addition, we found that the positive rate of NIS in the concurrent BRAF V600E and TERT promoter mutation group was lower. This might be due to the BRAF gene involvement in mitogen-activated protein kinase/extracellular signal-regulated protein kinase (MAPK/ERK) signaling pathways. The BRAF V600E gene mutation can lead to protein kinase activation and activation of ERK, and the mitotic signal is transmitted downstream of MAPK signaling pathway, resulting in the formation of tumors and further malignant transformation; TERT promoter mutations may aggravate this process by prolonging the life of cancer cells. Therefore, we speculate that DTC is more aggressive in patients with concurrent BRAF V600E and TERT promoter mutations, with a reduced degree of differentiation, increased degree of malignancy, reduced expression of some proteins (NIS), and loss of function ("nitrogen pump"). Unfortunately, we failed to find the relationship between TSHR expression and the two mutations. Perhaps, TSHR expression involved in carcinogenic mechanism differs from NIS expression in DTC.

BRAF V600E and TERT promoter mutations occur only in cancer tissue; they do not occur in benign nodular goiter and normal thyroid tissue. Detection of BRAF V600E and TERT promoter mutations will help to improve the pathological diagnosis of thyroid nodules that cannot be determined as benign or malignant by fine-needle aspiration biopsy. For DTC with a higher recurrence, it is necessary to access the prognosis (recurrence) of patients with DTC. Therefore, detecting BRAF V600E and TERT promoter mutations rather than the BRAF V600E mutation alone would help in prognosis prediction and development of individualized treatment programs. TERT promoter mutations or concurrent BRAF V600E and TERT promoter mutations were more common in the middle/high-risk group. For patients with TERT promoter mutations or concurrent BRAF V600E and TERT promoter mutations, which present an increased risk of recurrence, it will help to determine the risk of recurrence at an early stage through long-term follow-up and monitoring of patients that have been cured. In patients with concurrent BRAF V600E and TERT promoter mutations, NIS expression is also lower, when carrying out $^{131}$I radiotherapy; therefore, we may need to take other therapeutic measures. Liu *et al* [21] found that radiofrequency-mediated $^{131}$I radiotherapy shows obvious effects on DTC. Another study found that BRAF V600E mutations had an impact on NIS expression, and thyroid cancer cells increased iodine intake by silencing the BRAF gene and adding TSH [7]. However, our study has also failed to establish the specific mechanisms underlying NIS abnormal expression in DTC with concurrent BRAF V600E and TERT promoter mutations. There are maybe other unknown factors that affect NIS expression, and how to restore iodine uptake in DTC will become a major research focus in the future.

In summary, our results show that TERT promoter mutations were lower in patients with DTC, and the TERT C250T mutation was more common; the BRAF V600E mutation was not associated with gender, age, tumor size, lymph node metastasis, or recurrence risk stratification. TERT promoter mutations were associated with gender,

age, and recurrence risk stratification, and concurrent BRAF V600E and TERT promoter mutations were associated with lymph node metastasis, recurrence risk stratification, and a lower positive rate of NIS. Therefore, the detection of BRAF V600E mutation combined with TERT promoter mutation was instructive to prognosis assessment and treatment of DTC.

### Acknowledgements

We thank Translational Medicine Research Center and Department of Pathology of Gansu Province Tumor Hospital for providing experiment platform.

### Conflicts of interest

No conflict of interest exits in the submission of this manuscript, which has been approved by all authors for publication.

## References

1. Ho AS, Louise Davies L, Nixon IJ, *et al*. Increasing diagnosis of subclinical thyroid cancers leads to spurious improvements in survival rates. Cancer, 2015, 121:1793–1799.
2. Jiang LX, Chu HD, Zheng HT. B-Raf mutation and papillary thyroid carcinoma patients. Oncol Lett, 2016,11: 2699–2705.
3. Yarchoan M, Livolsi VA, Brose MS. BRAF mutation and thyroid cancer recurrence. J Clin Oncol, 2014, 33: 7–8.
4. Vinagre J, Almeida A, Pópulo H, *et al*. Frequency of TERT promoter mutations in human cancers. Nat Commun, 2013, 4: 405–415.
5. Liu X, Qu S, Liu R, *et al*. TERT promoter mutations and their association with BRAF V600E mutation and aggressive clinicopathological characteristics of thyroid cancer. J Clin Endocrinol Metab, 2014, 99: E1130–E1136.
6. Caillou B, Troalen F, Baudin E, *et al*. $Na^+/I^-$ symporter distribution in human thyroid tissues: an immunohistochemical study. J Clin Endocrinol Metab, 1998, 83: 4102–4106.
7. Kleiman D A, Buitrago D, Crowley MJ, *et al*. Thyroid stimulating hormone increases iodine uptake by thyroid cancer cells during BRAF silencing. J Surg Res, 2013, 182: 85–93.
8. Kogai T, Endo T, Saito T, *et al*. Regulation by thyroid-stimulating hormone of sodium/iodide symporter gene expression and protein levels in FRTL-5 cells. Endocrinology, 1997, 138: 2227–2232.
9. Haugen BR, Alexander EK, Bible KC, *et al*. 2015 American Thyroid Association Management Guidelines for Adult Patients with Thyroid Nodules and Differentiated Thyroid Cancer: The American Thyroid Association Guidelines Task Force on Thyroid Nodules and Differentiated Thyroid Cancer. Thyroid, 2016, 26: 1–133.
10. Brunello AG, Weissenberger J, Kappeler A, *et al*. Astrocytic alterations in interleukin-6/soluble interleukin-6 receptor alpha double-transgenic mice. Am J Pathol, 2000, 157: 1485–1493.
11. Xing M. BRAF mutation in thyroid cancer. Endocr Relat Cancer, 2005, 12: 245–262.
12. Xing M, Westra WH, Tufano RP, *et al*. BRAF mutation predicts a poorer clinical prognosis for papillary thyroid cancer. J Clin Endocrinol Metab, 2005, 90: 6373–6379.
13. Lee JH, Lee ES, Kim YS . Clinicopathologic significance of BRAF, V600E mutation in papillary carcinomas of the thyroid. Cancer, 2007, 110: 38–46.
14. Xing M, Alzahrani AS, Carson KA, *et al*. Association between BRAF V600E mutation and recurrence of papillary thyroid cancer. J Clin Oncol, 2015, 33: 42–50.
15. Alzahrani AS, Alsaadi R, Murugan AK, *et al*. TERT promoter mutations in thyroid cancer. Horm Cancer, 2016,7: 165–177.
16. Qasem E, Murugan AK, Al-Hindi H, *et al*. TERT promoter mutations in thyroid cancer: a report from a Middle Eastern population. Endocr Relat Cancer, 2015, 22: 901–908.
17. Gandolfi G, Ragazzi M, Frasoldati A, *et al*. TERT promoter mutations are associated with distant metastases in papillary thyroid carcinoma. Eur J Endocrinol, 2015, 172: 403–413.
18. Xing M, Liu R, Liu X, *et al*. BRAF V600E and TERT promoter mutations cooperatively identify the most aggressive papillary thyroid cancer with highest recurrence. J Clin Oncol, 2014, 32: 2718–2726.
19. Melo M, Da R A, Vinagre J, *et al*. TERT promoter mutations are a major indicator of poor outcome in differentiated thyroid carcinomas. J Clin Endocrinol Metab, 2014, 99: 754–765.
20. Kim YS, Kim JS, Bae JS, *et al*. Clinical implication of the BRAFV600E mutation in papillary thyroid carcinoma. World J Surg Oncol, 2013, 11: 1–5.
21. Liu QJ, Dong F, Shi-Hong MA. Radiofrequency-mediated $^{131}I$ radiotherapy in the treatment for 31 cases with differentiated thyroid cancer. J Oncol (Chinese), 2010, 16: 946–949.

**DOI 10.1007/s10330-016-0200-0**
**Cite this article as:** Ru XT, Liu QJ, Zhou HH, *et al*. BRAF V600E/TERT promoter mutations and NIS/TSHR expression in differentiated thyroid carcinoma and their clinical significance. Oncol Transl Med, 2017, 3: 71–76.

Oncology and Translational Medicine
DOI 10.1007/s10330-017-0218-8

April 2017, Vol. 3, No. 2, P77–P81

ORIGINAL ARTICLE

# Comparison of the effects of two types of multileaf collimators on tumor control probability in radiotherapy for breast cancer after conservative surgery based on the EUD model*

**Fuli Zhang, Yadi Wang (✉), Weidong Xu, Huayong Jiang, Junmao Gao, Qingzhi Liu, Na Lu, Diandian Chen, Bo Yao, Jun Hou, Heliang He, Jianping Chen**

Department of Radiation Oncology, General Hospital of Beijing Military Command, Beijing 100700, China

## Abstract

**Objective** To compute and compare the tumor control probability (TCP) of volumetric modulated arc therapy (VMAT) for breast cancer after conservative surgery based on two types of multileaf collimator (MLC) through a retrospective planning study.

**Methods** For a group of 9 patients diagnosed with left breast cancer, VMAT plan based on Agility MLC and beam modulator (BM) MLC were designed. The prescription dose was 50 Gy covering at least 95% of the planning target volume, 2 Gy per fraction. TCPs were calculated according to dose-volume histogram (DVH) analysis.

**Results** The TCP of the BM VMAT plan was slightly higher than that of the Agility VMAT plan (94.61% vs 94.23%) but was inferior with respect to delivery efficiency; the delivery time was reduced for Agility VMAT plan by 35% compared to BM VMAT plan.

**Conclusion** For breast cancer radiation therapy after conservative surgery, BM VMAT plans provide slightly higher TCP while the delivery of Agility VMAT plans is significantly faster than the BM VMAT plans.

**Key words:** tumor control probability (TCP); breast cancer; radiobiology; volumetric modulated arc therapy (VMAT)

Received: 2 January 2017
Revised: 11 February 2017
Accepted: 23 March 2017

Breast-conserving surgery (BCS) with subsequent whole breast irradiation (WBI) is an effective adjuvant treatment mode for early stage breast cancer. Some long-term clinical trials have shown comparable overall survival and disease-free survival rates for conservative surgery combined with WBI compared with postoperative mastectomy [1–3]. In recent years, volumetric modulated arc therapy (VMAT) has been introduced into clinical practice. VMAT can achieve a higher degree of intensity modulation than conventional intensity modulated radiotherapy (IMRT) by changing the gantry rotation speed, dose rate, and multileaf collimator (MLC) speed simultaneously. Many studies have shown that the VMAT technique may produce better target dose distributions as well as better organs at risk (OARs) sparing than conventional IMRT or three-dimensional conformal radiotherapy (3DCRT) [4–14].

To the best of our knowledge, no comparative studies of the radiobiological effects of different types of MLC on VMAT planning for breast cancer post conservative surgery have been conducted. This study investigated the effect of different MLCs on tumor control probability (TCP) in treating breast cancer with VMAT by comparing treatment plans for 9 patients developed using Elekta Agility and Beam Modulator (BM) (Elekta AB, Sweden).

✉ Corresponding to: Yadi Wang. Email: wangyadi@hotmail.com
* Supported by a grant from the Innovation Project of the PLA Army General Hospital of China (No. 2015-LC-18).

## Materials and methods

### EUD-based TCP radiobiological mathematical model

The equivalent uniform dose (EUD) based radiobiological mathematical model [15] is primarily based on two equations. This mathematical model has an excellent ability in fitting, for example, the Emami *et al*. normal tissue tolerance values [16]. The original definition of the EUD was derived from a mechanistic formulation using a linear quadratic cell survival model [17]. Subsequently, Niemierko *et al* [15] has suggested a phenomenological model of the form:

$$\mathrm{EUD} = \left( \sum_{i=1} (v_i D_i^a) \right)^{\frac{1}{a}}$$

Here, $a$ is a dimensionless model parameter that is specific to the tumor and $v_i$ is dimensionless and represents the i'th partial volume receiving dose $D_i$ in Gy. Since the relative volume of the whole structure of interest corresponds to 1, the sum of all partial volumes vi will be equal to 1. The choice of parameter a will determine the behavior of the EUD-based mathematical model. For example, as a increases to a large positive number, the EUD approaches the maximal dose; as a decreases to a large negative number, the EUD approaches the minimal dose; if a is equal to 1, the EUD becomes the dose average; and if a is equal to 0, the EUD is equal to the geometric mean [17]. The local control of a tumor will likely depend on the volume that received the minimum dose, since this is where the tumor cell survival should be highest. Consequently, the EUD for tumors will be close to the minimal dose, and the parameter should be a large negative number.

To calculate the TCP, EUD was calculated in the following equation:

$$TCP = \frac{1}{1 + (\frac{TCD_{50}}{EUD})^{4\lambda 50}} \quad (2)$$

Here, the $TCD_{50}$ is the tumor dose necessary to control 50% of the tumor when the tumor is homogeneously irradiated. $\gamma 50$ is a dimensionless model parameter that is specific to the tumor of interest and describes the slope of the dose response curve. In this study, the parameters for WBI of T1N0 tumors were used: $TCD_{50}$ = 30.89 Gy and $\gamma$ 50 = 1.3%/% [18].

### Patient selection and positioning

Nine patients with T1N0 left breast carcinoma treated with 3DCRT or conventional IMRT in our clinic were selected for this retrospective analysis of VMAT planning. The median age of the patients was 53 years (range: 38–63 years). The patients were simulated in the supine position with both arms raised above their head. They were scanned by computed tomography (CT) on a Philips Brilliance Big Bore simulator (Philips Medical Systems, Madison, WI) from the level of the larynx to the bottom of the lungs with a 5 mm slice thickness and slice spacing. The study was approved by the ethical committee of the General Hospital of Beijing Military Command. All patients provided written consent for storage of their medical information in the hospital database and for research use.

### Delineation of target volumes and OARs

The delineation of target and OARs for all patients was performed by a single radiation oncologist with expertise in breast cancer treatment. The clinical target volume (CTV) consisted of the lumpectomy cavity with a margin of 15 mm modified to stay within the glandular tissue apparent on the CT scan. The planning target volume (PTV) was constructed by adding a 5 mm margin to the CTV and retracting the PTV to the tissue inside 3 mm of the skin to account for dose build-up during dose calculation. OARs delineated both lungs, the heart, the contralateral breast, anld the left anterior descending artery (LAD).

### MLC specification and modeling

The Agility MLC has 80 pairs of leaves 5 mm wide at the isocenter, and the maximum field size is 40 cm × 40 cm. The maximum leaf speed is 3.5 cm $s^{-1}$, or up to 6.5 cm s-1 combined with a dynamic leaf guide (DLG). The BM MLC has 80 leaves with a leaf width of 4 mm at the isocenter, and the maximum field size is 21 cm × 16 cm. The leaf can move at a maximum speed of 3 cm $s^{-1}$. The minimum gap between opposite leaves is 5 mm. The maximum distance between leaves on the same leaf guide is 21 cm and the leaves have the ability to interdigitate. Two accelerators equipped with the two types of MLC were modeled in the Monaco treatment planning system (version 5.1, Elekta AB, Sweden).

### VMAT planning and quality assurance

VMAT plans were generated on a Monaco TPS station using 6 MV photon beams from an Elekta Axesse linac with Agility MLC and a Synergy S linac with BM, respectively.

Two VMAT plans were designed for each patient. In each plan, the couch angle was set to 0° and the collimator angle was set to 90°. Two partial arcs of 220° ranging from 170° to 310° were selected. These angles were chosen to avoid direct irradiation to the spinal cord, contralateral breast, and contralateral lung. The prescribed dose to the PTV was 50 Gy in 25 fractions. The plans were normalized to cover 95% of the PTV with 100% of the prescribed

**Table 1** Dose-volume constraints for PTV and OARs

| Structures | Volume (%) | Dose (Gy) |
|---|---|---|
| PTV | 95 | 50 |
| Heart | ≤10 | 30 |
| Contralateral breast | ≤15 | 3 |
| Contralateral lung | ≤15 | 3 |
| Ipsilateral lung | ≤70 | 5 |
| | ≤50 | 10 |
| | ≤30 | 20 |
| | ≤20 | 30 |

dose. The optimization objectives and constraints as listed in Table 1 were the same for all plans.

Plan delivery quality assurance (DQA) was performed with a Delta4 diode detector array (ScandiDos Inc., Sweden). The passing criterion with the gamma tests for DQA of the VMAT plan is 90% (3% dose difference, 3 mm distance to agreement) in our clinic.

### Statistical analysis

Student's *t* test was used to compare means after an equal check of variance and statistical analyses were conducted using SPSS software (version 18.0, SPSS Inc., USA). The confidence interval was 95% and statistical significance was assigned to a *P*-value of $< 0.05$.

## Results

### Comparison of TCP

Statistical analysis showed a significant difference between the two plans based on the two types of MLC ($P = 0.008$). BM-based VMAT plans acquired a higher TCP than Agility-based VMAT plans.

### Comparison of OARs dose-volume parameters

The dose-volume parameters of the OARs were listed in Table 2. Significant differences were observed in V5, V10, and V20 of the ipsilateral lung ($P = 0.000$, $P = 0.000$, $p = 0.004$), V3 of the contralateral breast ($P = 0.013$), V5 of the heart ($P = 0.007$), and the Dmean of LAD ($P = 0.026$). Agility-based VMAT plans spared more normal tissue when irradiating tumors.

### Plan delivery efficiency

Delivery efficiency was assessed by measuring the MUs per fraction and the beam delivery time for each plan (Table 3). There was no significant difference between the two plans in terms of MU required. However, the delivery time for VMAT will not only depend on the number of MUs, but also on dose rate, speed of MLC movement, and gantry rotation. Therefore, the MU results of our current study do not reflect the actual delivery time. The actual delivery time with Agility was 35% less than that with BM.

**Table 2** Comparison of dose and volume parameters for OARs ($\bar{\chi} \pm s$)

| OARs | Agility | BMC | t value | *p* value |
|---|---|---|---|---|
| Ipsilateral lung | | | | |
| V5 | 64.80±8.11 | 82.02±6.05 | -9.464 | 0.000 |
| V10 | 40.86±6.63 | 50.71±5.99 | -7.609 | 0.000 |
| V20 | 25.82±5.00 | 28.47±4.49 | -3.976 | 0.004 |
| V30 | 17.18±3.88 | 18.63±3.92 | -2.224 | 0.057 |
| Contralateral breast | | | | |
| V3 | 9.45±2.70 | 12.81±3.63 | -3.160 | 0.013 |
| Contralateral lung | | | | |
| V3 | 7.21±1.98 | 7.78±1.31 | -0.894 | 0.398 |
| V5 | 2.03±1.11 | 1.94±1.22 | 0.145 | 0.888 |
| Heart | | | | |
| V5 | 66.00±6.79 | 73.04±7.80 | -3.560 | 0.007 |
| V10 | 37.57±8.32 | 41.41±10.75 | -1.440 | 0.188 |
| V20 | 12.16±3.12 | 12.13±3.76 | 0.036 | 0.972 |
| V30 | 4.78±2.19 | 4.88±2.07 | -0.278 | 0.788 |
| LAD | | | | |
| Dmean | 22.10±7.11 | 23.91±7.69 | -2.732 | 0.026 |

**Table 3** Number of MUs and delivery time with each type of MLC

| Items | Agility | BM | *P* value |
|---|---|---|---|
| MUs | 1140.1 ± 154.3 | 1133.2 ± 173.9 | 0.837 |
| Delivery time (min) | 2.6 ± 0.2 | 4.0 ± 0.2 | 0.000 |

## Discussion

The MLC is very important in target shaping and OARs sparing. Many studies have investigated the effect of MLC leaf width on VMAT planning technique in several tumor sites [19–22]. In this study, we clearly showed that different MLC types have different radiobiological and, therefore, different clinical effects on breast cancer radiotherapy post conservative surgery. According to the calculation results from the EUD-based model, the BM VMAT plan may achieve a slightly higher TCP rate. Meanwhile, the Agility VMAT plan can achieve higher sparing of normal tissues.

However, it is well known that a longer treatment time will reduce cell death because prolonged treatments provide cells with an opportunity to repair DNA damage. Therefore, the faster leaf travel speed of the Agility MLC may be beneficial in decreasing DNA damage repair and improving treatment delivery efficiency.

The most important finding of this study is that VMAT can be delivered extremely efficiently with Agility and the delivery time was reduced for Agility by 35% compared with BM. The reasons may be as follows: (1)

Elekta BM was introduced into clinical work earlier, and it only supports the binned dose rate variation including five different dose rates: 600 MU/min, 300 MU/min, 150 MU/min, 75 MU/min, 37 MU/min; however, the Elekta Axesse linac utilized an upgraded integrity control system, which supported continuous variable dose rate variations with more available dose rate changes from 45 MU/min to 660 MU/min [23]. (2) The maximum leaf speed of Agility MLC is 6.5 cm $s^{-1}$, which is faster than that of BM MLC and is conducive to a reduction in time of delivery. This feature can improve the patients' comfort and reduce the intra-fraction motion of organs during radiation delivery.

Another issue demanding consideration is inter- and intra-fraction motion. The auto flash margin function embedded in the Monaco planning system can help solve the problem. Beyond that, the accuracy of the setup in VMAT can be further improved by using a breathing control device and an image guidance technique. The effect of breathing motion on plan delivery as well as calculation of EUD and TCP is currently under investigation by using four-dimensional computed tomography (4D-CT) in our department and the results will be reported in the near future.

## Conclusions

For radiation therapy after conservative surgery for breast cancer, BM VMAT plans provide slightly higher TCP, but the delivery of Agility VMAT plans are significantly faster than those of BM VMAT plans. In addition, Agility VMAT plans can spare more normal tissues and achieve higher therapeutic ratios during irradiation of tumors.

### Conflicts of interest

The authors declare that they have no competing interests.

## References


1. Fisher B, Jeong JH, Anderson S, *et al*. Twenty-five-year follow-up of a randomized trial comparing radical mastectomy, total mastectomy, and total mastectomy followed by irradiation. N Engl J Med, 2002, 347: 567–575.
2. Veronesi U, Cascinelli N, Mariani L, *et al*. Twenty-year follow-up of a randomized study comparing breast-conserving surgery with radical mastectomy for early breast cancer. N Engl J Med, 2002, 347: 1227–1232.
3. Rusthoven KE, Carter DL, Howell K, *et al*. Accelerated partial-breast intensity-modulated radiotherapy results in improved dose distribution when compared with three-dimensional treatment-planning techniques. Int J Radiat Oncol Biol Phys, 2008, 70: 296–302.
4. Lee B, Lee S, Sung J, *et al*. Radiotherapy-induced secondary cancer risk for breast cancer: 3D conformal therapy versus IMRT versus VMAT. J Radiol Prot, 2014, 34: 325–331.
5. Haertl PM, Pohl F, Weidner K, *et al*. Treatment of left sided breast cancer for a patient with funnel chest: volumetric-modulated arc therapy vs. 3D-CRT and intensity-modulated radiotherapy. Med Dosim, 2013, 38: 1–4.
6. Wang J, Li X, Deng Q, *et al*. Postoperative radiotherapy following mastectomy for patients with left-sided breast cancer: A comparative dosimetric study. Med Dosim, 2015, 40: 190–194.
7. Qi XS, Liu TX, Liu AK, *et al*. Left-sided breast cancer irradiation using rotational and fixed-field radiotherapy. Med Dosim, 2014, 39: 227–234.
8. Pasler M, Georg D, Bartelt S. Node-positive left-sided breast cancer: does VMAT improve treatment plan quality with respect to IMRT? Strahlentherapie Onkol, 2013, 189: 380–386.
9. Scorsetti M, Alongi F, Fogliata A, *et al*. Phase I-II study of hypofractionated simultaneous integrated boost using volumetric modulated arc therapy for adjuvant radiation therapy in breast cancer patients: a report of feasibility and early toxicity results in the first 50 treatments. Radiat Oncol, 2012, 7: 145.
10. Abo-Madyan Y, Aziz MH, Aly MM, *et al*. Second cancer risk after 3D-CRT, IMRT and VMAT for breast cancer. Radiother Oncol, 2014, 110: 471–476.
11. Popescu CC, Olivotto IA, Beckham WA, *et al*. Volumetric modulated arc therapy improves dosimetry and reduces treatment time compared to conventional intensity-modulated radiotherapy for locoregional radiotherapy of left-sided breast cancer and internal mammary nodes. Int J Radiat Oncol Biol Phys, 2010, 76: 287–295.
12. Essers M, Osman SO, Hol S, *et al*. Accelerated partial breast irradiation (APBI): are breath-hold and volumetric radiation therapy techniques useful? Acta Oncol, 2014, 53: 788–794.
13. Rao M, Yang W, Chen F, *et al*. Comparison of Elekta VMAT with helical tomotherapy and fixed field IMRT: plan quality, delivery efficiency and accuracy. Med Phys, 2010, 37: 1350–1359.
14. Tsai PF, Lin SM, Lee SH, *et al*. The feasibility study of using multiple partial volumetric-modulated arcs therapy in early stage left-sided breast cancer patients. J Appl Clin Med Phys, 2012,13: 3806.
15. Niemierko A. Reporting and analyzing dose distributions: a concept of equivalent uniform dose. Med Phys, 1997, 24: 103-110.
16. Emami B, Lyman J, Brown A, *et al*. Tolerance of normal tissue to therapeu-tic irradiation. Int J Radiat Oncol Biol Phys, 1991, 21: 109–122.
17. Wu Q, Mohan R, Niemierko A, *et al*. Optimization of intensity-modulated radiotherapy plans based on the equiv-alent uniform dose. Int J Radiat Oncol Biol Phys, 2002, 52: 224–235.
18. Okunieff P, Morgan D, Niemierko A, *et al*. Radiation dose-response of human tumors. Int J Radiat Oncol Biol Phys, 1995, 32:1227–1237.
19. Chae SM, Lee GW, Son SH. The effect of multileaf collimator leaf width on the radiosurgery planning for spine lesion treatment in terms of the modulated techniques and target complexity. Radiat Oncol, 2014, 9: 72.
20. Blumer N, Scherf C, Kohn J, *et al*. New possibilities for volumetric-modulated arc therapy using the Agility 160-leaf multileaf collimator. Strahlenther Onkol, 2014, 190: 1066–1074.
21. Serna A, Puchades V, Mata F, *et al*. Influence of multi-leaf collimator leaf width in radiosurgery via volumetric modulated arc therapy and 3D dynamic conformal arc therapy. Phys Med, 2015, 31: 293–296.
22. Wang S1, Ai P, Xie L, *et al*. Dosimetric comparison of different multileaf collimator leaves in treatment planning of intensity-modulatedradiotherapy for cervical cancer. Med Dosim, 2013, 38: 454–459.

23. Boylan C, McWilliam A, Johnstone E, *et al*. The impact of continuously-variable dose rate VMAT on beam stability, MLC positioning, and overall plan dosimetry. J Appl Clin Med Phys, 2012,13: 4023.

**DOI 10.1007/s10330-017-0218-8**
**Cite this article as:** Zhang FL, Wang YD, Xu WD, *et al*. Comparison of the effects of two types of multileaf collimators on tumor control probability in radiotherapy for breast cancer after conservative surgery based on the EUD model. Oncol Transl Med, 2017, 3: 77–81.

Oncology and Translational Medicine
DOI 10.1007/s10330-016-0197-7

April 2017, Vol. 3, No. 2, P82–P85

ORIGINAL ARTICLE

# Differential expression of nucleolin in colon adenoma and adenocarcinoma

**Guozhao Meng, Junlei Yi, Ming Xie (✉)**

Department of Pathology, School of Fundamental Medicine and Affiliated Hospital, Xiangnan University, Chenzhou 423000, China

## Abstract

**Objective** The aim of the study was to investigate the discrepancy in nucleolin expression between colon adenoma and colon adenocarcinoma, explore the role of nucleolin expression in the carcinogenesis of colon adenocarcinoma, and determine the correlation of the nucleolin expression level with histological grade in colon adenocarcinoma.

**Methods** In total, 80 cases of colon adenocarcinoma with cancer-adjacent colon mucosa and 60 cases of colon adenomas were examined by immunohistochemistry using an antibody against nucleolin. Nucleolin expression levels in these groups were compared. The correlation between the nucleolin expression level and grade of colon adenocarcinoma was analyzed.

**Results** Nucleolin expression is located in the nuclei of colon adenocarcinoma, colon adenoma, and cancer-adjacent colon mucosa tissues with different intensities. A semiquantitative evaluation using the Allred scoring system showed that the nucleolin immunostaining score in colon adenocarcinoma (7.8 ± 0.1) was significantly higher than those in colon adenoma (6.3 ± 0.2) and cancer-adjacent colon mucosa (5.4 ± 0.1; $P < 0.01$). The nucleolin immunostaining score in colon adenoma was significantly higher than that in cancer-adjacent colon mucosa ($P < 0.01$). Nucleolin expression levels in well-differentiated and moderately differentiated adenocarcinoma (6.8 ± 0.2) were significantly lower than those in poorly differentiated adenocarcinoma (8.0 ± 0.1; $P < 0.01$).

**Conclusion** Increased nucleolin expression may play an important role in the process of malignant transformation of colon adenocarcinoma and predicts a poor prognosis.

**Key words:** nucleolin; colon adenoma; colon adenocarcinoma

Received: 9 October 2016
Revised: 8 November 2016
Accepted: 19 February 2017

Colon adenoma is considered a precursor lesion of colon adenocarcinoma. The protein changes driving this process are complex. Understanding the mechanisms of adenoma-to-carcinoma transformation is critical to gain insight into the triggers of invasion and proliferation of the cancer.

Nucleolin is a nuclear protein with a molecular weight of 105 kD; it is abundant in the nucleolus and mainly distributed in the nucleolar organizer region [1]. Nucleolin has been implicated in many cellular processes, including the transcription, packing, and transport of ribosomal RNA, DNA replication and recombination, cell cycle progression, and apoptosis [2]. Expression of nucleolin in normal cells is limited to the nuclei, but in active cells or malignant tumor cells, it is overexpressed and translocated from the nucleus to the cytoplasm [3–5]. To date, only a few studies have examined nucleolin expression in human cancer tissues [3, 6–8], and none have examined colon adenocarcinoma as well as its precursor lesions. In the current study, alterations in nucleolin expression in colon adenoma and colon adenocarcinoma tissues as well as its prognostic impact were examined.

## Materials and methods

### Human tissues

Formalin-fixed paraffin-embedded tissue samples from 80 cases of colon adenocarcinoma with cancer-adjacent colon mucosa tissues and 60 cases of colon adenoma were retrieved from the archive files of Department of Pathology, School of Fundamental Medicine and Affiliated Hospital, Xiangnan University (China) from 2013 to 2015. No patient accepted any therapy before the operation.

✉ Correspondence to: Ming Xie. Email: hongbu@yeah.net

### Immunohistochemistry

Sections were deparaffinized, rehydrated, and washed in phosphate-buffered saline (PBS, pH 7.5) for 15 minutes. Endogenous peroxidase activity was blocked by incubation for 30 minutes in a 3% hydrogen peroxide solution. Tissue antigens were retrieved by pressure cooking at 120 °C for 8 minutes in a citrate buffer solution, pH 7.0. The specimens were washed once with PBS. Non-specific binding was blocked by incubating the slides with normal goat serum in PBS for 30 minutes at 37 °C and then incubated overnight at 4 °C with the primary antibody against nucleolin (MS-3, 1:200; Santa Cruz Biotechnology, Santa Cruz, CA, USA). After sections were washed with PBS 3 times, they were incubated with the secondary antibody for 40 minutes at 37 °C. After they were washed with PBS 3 times, the sections were immunostained with avidin-biotin complex for 40 minutes at 37 °C. Visualization of the immunoreaction was conducted with 3,3'-diaminobenzidine (DAB; Sigma, Co., St. Louis, MO, USA) for 5 minutes. Finally, sections were counterstained with hematoxylin. Positive and negative controls were used for each section.

Staining was semiquantitatively examined by 2 independent pathologists using the Allred 8-unit system [9]. The positively stained tumor cells were scored as follows: 0, none; 1, < 1/100; 2, 1/100 to 1/10; 3, 1/10 to 1/3; 4, 1/3 to 2/3; and 5, > 2/3. The staining intensity of the positive tumor cells was scored as follows: 0, none; 1, weak; 2, intermediate; and 3, strong. For each case, the staining proportion and intensity scores were determined. The differences in nucleolin expression levels among colon adenocarcinoma, colon adenoma, and cancer-adjacent colon mucosa were evaluated, and the correlation of the nucleolin expression level with the grade of colon adenocarcinoma was analyzed.

### Statistical analysis

SPSS 13.0 was used for the statistical analysis. The differences in the immunostaining score among groups were evaluated using unpooled *t*-tests. Differences in percentage were evaluated using Fisher's exact tests. A *P*-value of < 0.05 was considered statistically significant.

## Results

Immunohistochemically, the nuclei were positively stained for nucleolin in all tissues samples, with various staining intensities. In cancer-adjacent colon mucosa, the nuclei of glandular cells exhibited weak staining for nucleolin with low immunostaining scores of 5.4 ± 0.1 (Fig. 1). In colon adenoma, the nuclei of glandular cells exhibited moderate staining for nucleolin with an intermediate immunostaining score of 6.3 ± 0.2 (Fig. 2). In contrast, the colon adenocarcinoma was strongly positive for nucleolin, with a high immunostaining score of 7.8 ± 0.1 (Fig. 3 and 4). A statistical evaluation revealed that the nucleolin immunostaining score was significantly higher in colon adenocarcinoma than in colon adenoma and cancer-adjacent colon mucosa ($P$ < 0.01). The nucleolin immunostaining score in colon adenoma was significantly higher than that in cancer-adjacent colon mucosa ($P$ < 0.01). The nucleolin immunostaining scores of cancer-adjacent colon mucosa, colon adenoma, and colon adenocarcinoma were summarized in Table 1.

Moreover, when comparing the nucleolin immunostaining score in colon adenocarcinomas with different histological grades, we found that the nucleolin immunostaining score in low-grade colon adenocarcinoma (6.8 ± 0.2; Fig. 3) was significantly lower than that in high-grade colon adenocarcinoma (8.0 ± 0.1; Fig. 4; $P$ < 0.01). The immunostaining scores in colon adenocarcinoma with different grades were summarized in Table 2. These data demonstrate that the nucleolin expression level is positively correlated with the histological grade of colon adenocarcinoma.

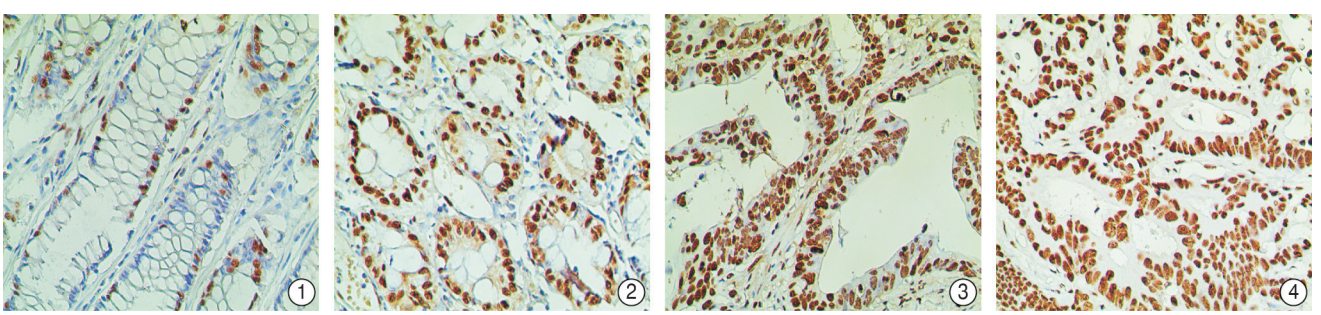


**Fig. 1** Nucleolin immunostaining in cancer-adjacent colon mucosa (SP, 400×).
**Fig. 2** Nucleolin immunostaining in colon adenoma (SP, 400×).
**Fig. 3** Nucleolin immunostaining in well-differentiated colon adenocarcinoma (SP, 400×).
**Fig. 4** Nucleolin immunostaining in poorly differentiated colon adenocarcinoma (SP, 400×).

**Table 1** Nucleolin immunostaining scores in colon adenocarcinoma and colon adenoma

| Groups | *n* | Immunostaining score ($\bar{\chi} \pm s$) |
|---|---|---|
| Colon adenocarcinoma | 80 | 7.8 ± 0.1 |
| Colon adenoma | 60 | 6.3 ± 0.2* |
| Cancer adjacent colon mucosa | 50 | 5.4 ± 0.1*# |

Note: Compared with colon adenocarcinoma, * $P < 0.01$; Compared with colon adenoma, # $P < 0.01$

**Table 2** Nucleolin immunostaining scores in colon adenocarcinomas with different grades

| Groups | *n* | Immunostaining score ($\bar{\chi} \pm s$) |
|---|---|---|
| Grades I and II | 50 | 6.8 ± 0.2 |
| Grade III | 30 | 8.0 ± 0.1* |

Note: Compared with colon adenocarcinoma Grades I and II, * $P < 0.01$

## Discussion

Nucleolin not only functions in a number of fundamental processes, but also in malignant transformation of tumor cells. The overexpression of nucleolin in proliferative and malignant cells indicates that the protein plays an important role in carcinogenesis in some cancers. Astrocytes in the normal human brain do not express nucleolin at a significant level, whereas glioblastoma cell lines and primary human astrocytoma cells exhibit considerable nucleolin expression [3]. Nucleolin expression levels in benign melanocytic lesions are lower than those in dysplastic and malignant melanocytic lesions [8]. A previous study has shown that nucleolin expression levels are significantly higher in atypical and anaplastic meningiomas than in benign meningiomas, and are positively correlated with the Ki-67 labeling index [7]. The total cellular nucleolin level is higher in B-cell chronic lymphocytic leukemia cells than in normal B cells, primarily as a result of the much higher level of cytoplasmic nucleolin in the former cell type [5]. Given its positive correlation with cell growth, the particularly high expression of nucleolin in malignant tumor cells is not surprising. In the present study, the nucleolin immunostaining score in colon adenocarcinoma was significantly higher than those in colon adenoma and cancer-adjacent colon mucosa. The nucleolin immunostaining score in colon adenoma was significantly higher than that in cancer-adjacent colon mucosa. These data indicate that the nucleolin expression level is elevated during the development of colon adenocarcinoma.

The overexpression of nucleolin is not only related to malignancy, but also to a poor clinical prognosis for certain cancer types. In prostate carcinomas, a high nucleolin expression level is correlated with a higher incidence of lymph node metastasis and a higher clinicopathological stage [10]. Cell surface-localized nucleolin expression in prostate cancer cells is elevated and acts as hepatocyte growth factor receptor during cancer progression [11]. The abnormal nucleolin staining patterns in melanoma are correlated with tumor progression and predict a worse prognosis [8]. A reduction in nucleolin expression by siRNA knockdown in a glioblastoma cell line caused a dramatic decrease in cell proliferation, induced cell cycle arrest *in vitro*, and caused a dramatic reduction in tumor size in nude mice [3]. In the current study, further analysis of nucleolin expression with respect to tumor histological grade revealed that the nucleolin immunostaining score in high-grade colon adenocarcinoma was significantly higher than that of low-grade colon adenocarcinoma. These data demonstrated that high nucleolin expression levels in colon adenocarcinoma were correlated with a worse prognosis. Accordingly, we postulate that nucleolin overexpression is an important molecular event during the carcinogenesis of colon adenocarcinoma.

The mechanism by which high nucleolin expression predicts a poor prognosis is presently unclear. It has been documented that anti-nucleolin nonantisense G-rich oligonucleotides could inhibit proliferation and induce apoptosis in cell lines derived from solid tumors and leukemias [4–5]. A previous study has shown that the knockdown of nucleolin in HeLa cells leads to cell cycle arrest and increased apoptosis [12]. Subcellular localization of nucleolin in epithelial cells is Rb-dependent and correlated with nucleolin/DNA binding activity [13]. Nucleolin contributes to the activation of c-myc gene and promotes the induction of B-cell lymphomas [14–15]. Our previous study demonstrated that the overexpression of nucleolin plays an important role during the carcinogenesis of cervical squamous cell carcinoma, and high nucleolin expression levels in cervical intraepithelial neoplasia and cervical squamous cell carcinoma are positively correlated with tumor progression [6]. In addition to nucleolin, CD133 and β-catenin expression levels in tumor cells have significant impacts on prognosis in colon cancer [16].

Taken together, we found that nucleolin expression levels differed significantly between colon adenoma and colon adenocarcinoma, and the nucleolin expression level was positively correlated with the histological grade of colon adenocarcinoma. We postulate that the increased nucleolin expression level plays an important role in the pathogenesis of colon adenocarcinoma and predicts a poor prognosis.

## Conflicts of interest

The authors indicated no potential conflicts of interest.

## References


1. Lapeyre B, Bourbon H, Amalric F. Nucleolin, the major nucleolar protein of growing eukaryotic cells: an unusual protein structure revealed by the nucleotide sequence. Proc Natl Acad Sci USA, 1987, 84: 1472–1476.
2. Ginisty H, Sicard H, Roger B, *et al*. Structure and functions of nucleolin. J Cell Sci, 1999, 112: 761–772.
3. Xu Z, Joshi N, Agarwal A, *et al*. Knocking down nucleolin expression in gliomas inhibits tumor growth and induces cell cycle arrest. J Neurooncol, 2012, 108: 59–67.
4. Mi Y, Thomas SD, Xu X, *et al*. Apoptosis in leukemia cells is accompanied by alterations in the levels and localization of nucleolin. J Biol Chem, 2003, 278: 8572–8579.
5. Otake Y, Soundararajan S, Sengupta TK, *et al*. Overexpression of nucleolin in chronic lymphocytic leukemia cells induces stabilization of bcl2 mRNA. Blood, 2007, 109: 3069–3075.
6. Meng GZ, Zi Y, Li HQ, *et al*. Nucleolin expression is correlated with carcinogenesis and progression of cervical squamous cell carcinoma. J South Med Univ (Chinese), 2015, 35: 1511–1514.
7. Ohkoudo M, Sawa H, Shiina Y, *et al*. Morphometrical analysis of nucleolin immunohistochemistry in meningiomas. Acta Neuropathol, 1996, 92: 1–7.
8. Mourmouras V, Cevenini G, Cosci E, *et al*. Nucleolin protein expression in cutaneous melanocytic lesions. J Cutan Pathol, 2009, 36: 637–646.
9. Allred DC, Clark GM, Elledge R, *et al*. Association of p53 protein expression with tumor cell proliferation rate and clinical outcome in node-negative breast cancer. J Natl Cancer Inst, 1993, 85: 200–206.
10. Semba S, Mizuuchi E, Yokozaki H. Requirement of phosphatase of regenerating liver-3 for the nucleolar localization of nucleolin during the progression of colorectal carcinoma. Cancer Sci, 2010, 101: 2254–2261.
11. Tate A, Isotani S, Bradley MJ, *et al*. Met-independent hepatocyte growth factor-mediated regulation of cell adhesion in human prostate cancer cells. BMC Cancer, 2006, 6: 197.
12. Ugrinova I, Monier K, Ivaldi C, *et al*. Inactivation of nucleolin leads to nucleolar disruption, cell cycle arrest and defects in centrosome duplication. BMC Mol Biol, 2007, 8: 66.
13. Grinstein E, Shan Y, Karawajew L, *et al*. Cell cycle-controlled interaction of nucleolin with the retinoblastoma protein and cancerous cell transformation. J Biol Chem, 2006, 281: 22223–22235.
14. Hanakahi LA, Dempsey LA, Li MJ, *et al*. Nucleolin is one component of the B cell-specific transcription factor and switch region binding protein, LR1. Proc Natl Acad Sci USA, 1997, 94: 3605–3610.
15. Brys A, Maizels N. LR1 regulates c-myc transcription in B-cell lymphomas. Proc Natl Acad Sci USA, 1994, 91: 4915–4919.
16. Abdelbary EH, Rashed HE, Ismail EI, *et al*. Prognostic value of cancer stem cell markers CD133, ALDH1 and nuclear β-catenin in colon cancer. Chinese-German J Clin Oncol, 2014, 13: 379–385.


**DOI 10.1007/s10330-016-0197-7**
**Cite this article as:** Meng GZ, Yi JL, Xie M. Differential expression of nucleolin in colon adenoma and adenocarcinoma. Oncol Transl Med, 2017, 3: 82–85.

Oncology and Translational Medicine
DOI 10.1007/s10330-015-0093-3

April 2017, Vol. 3, No. 2, P86–P90

ORIGINAL ARTICLE

# Epidermal growth factor enhances chemosensitivity of colon cancer by inducing cancer stem cells to enter the cell cycle

**You Zou, Xiaolan Li, Deding Tao, Junbo Hu, Jianping Gong (✉)**

Department of General Surgery, Tongji Hospital, Tongji Medical College, Huazhong University of Science and Technology, Wuhan 430030, China

## Abstract

**Objective** The aim of the study was to investigate whether colon cancer stem cells induced by epidermal growth factor (EGF) to enter the cell cycle enhanced the chemosensitivity of colon cancer.

**Methods** *In vitro*, EGF was used to stimulate the entry of human colon cancer HCT116 cells into the cell cycle. Before and after treatment with EGF, CD133+ HCT116 cells were collected and flow cytometry was conducted to determine the apoptosis rate based on the 5-Fu and Ki-67 expression rates. The cell cycle distribution of the two groups was also determined. *In vivo*, a subcutaneous xenograft model of HCT116 human colon cancer cell lines in nude mice was established. The nude mice were divided into two groups and treated with EGF and 5-Fu, respectively. Differences in the growth of implanted tumors revealed the efficiency of cycle-induction combined chemotherapy.

**Results** (1) After EGF stimulation, the S-G2/M proportion of CD133+ HCT116 cells and Ki67 expression were increased, indicating that more cancer stem cells entered the cell cycle and promoted proliferation; (2) After EGF stimulation, CD133+ HCT116 cells showed a higher apoptosis rate induced by 5-Fu. (3) Animal experiments showed that the group subjected to combined treatment with EGF and 5-Fu had smaller tumor sizes compared to the group treated with 5-Fu alone.

**Conclusion** EGF enhanced tumor sensitivity to chemotherapeutic drugs, likely by promoting tumor stem cells to enter the cell cycle.

**Key words:** chemosensitivity; tumor stem cell; cell cycle

Received: 30 April 2015
Revised: 27 September 2016
Accepted: 12 December 2016

Colorectal cancer is a common malignant tumor with high mortality. Solid tumors are composed of heterogeneous cell populations with different biological characteristics. A small number of cells known as cancer stem cells (CSCs) can sustain the malignant population [1–3], and the population was found to be correlated with multidrug resistance, tumor recurrence, and low patient survival [4–8]. Recent studies showed that in leukemia and in solid tumors, CSCs are particularly resistant to conventional chemo and radiation therapies compared to more differentiated cells in the non-CSC compartment, which comprise the tumor bulk. It was reported that CD34+/CD38– leukemia precursors cells have reduced sensitivity to daunorubicin, a major drug used in leukemia treatment, compared to leukemic blasts (CD34+/CD38+ counterpart) [9–10]. Furthermore, CSCs from acute and chronic myelogenous leukemia are relatively quiescent and contribute to chemotherapy resistance because the sensitivity to chemotherapeutic agents relies upon lethal cellular damage during cell cycle progression in highly proliferative cells [11–12]. Ishikawa *et al* [13] demonstrated that the bone marrow endosteal region was enriched in quiescent human acute myeloid leukemia (AML) stem cells (LSCs) and *in vivo* cytokine treatment induced their entry into the cell cycle. Using an *in vivo* treatment strategy in an NOD/SCID/IL2rynull human AML xenotransplantation model, elimination of human primary AML LSCs was significantly enhanced through *in vivo* cell cycle modification [13]. However, it was not reported whether this strategy is effective for solid tumors. In our study, by using epidermal growth factor (EGF) to induce the entry of colon cancer cells into

✉ Correspondence to: Jianping Gong. Email: jpgong@tjh.tjmu.edu.cn

the cell cycle and using CD133 as a marker of colorectal CSCs, we found that EGF enhanced tumor sensitivity to chemotherapeutic drugs, likely by promoting tumor stem cells to enter the cell cycle.

## Materials and methods

### Cell culture

The human colon cancer cell line HCT116 was obtained from the China Centre for Type Culture Collection (CCTCC; Wuhan, China) and maintained in RPMI-1640 (Hyclone, Logan, UT, USA) medium supplemented with 10% fetal bovine serum (Hyclone), 100 U/mL penicillin, and 100 μg/mL streptomycin (Invitrogen, Carlsbad, CA, USA) and cultured in a humidified atmosphere of 5% $CO_2$ at 37°C.

### Chemical treatment

HCT116 cells were seeded at $1 \times 10^6$ cells per well in 6-well culture plates. After 24 h, the culture medium was changed to contain medium free of bovine serum. EGF and 5-fluorouracil (5-FU) were added to the cell culture at concentrations shown in Table 1. The cells were harvested after 24 h and 48 h and prepared for analysis.

### CD133 expression analysis by flow cytometry and cell sorting

CD133 expression was evaluated by direct immunofluorescent staining using the AC133 mouse monoclonal antibody (anti-CD133-PE, AC133, Miltenyi Biotec, Bergisch Gladbach, Germany) directly conjugated with phycoerythrin. Mouse IgG1-phycoerythrin was used as the isotype control antibody. All cells were stained according to the manufacturer's recommendations. Briefly, $2 \times 10^5$ live cells were suspended in 100 μL of buffer (0.5% fetal calf serum and 2 mM EDTA) and stained for 10 min at 4 °C with 10 μL of the AC133 antibody (1:11). Cells were washed to remove excess unbound antibodies and analyzed for phycoerythrin expression by flow cytometry on a FACSort cytometer (BD Biosciences, Franklin Lakes, NJ, USA). Ten thousand events were acquired and analyzed using Cellquest (BD Biosciences) software. To sort cells expressing CD133, the cells were stained as described above and resuspended in the same buffer at $10^6$ cells/mL. Sorting was performed on a FACSVantage flow cytometer (BD Biosciences). The CD133+ cells were collected.

### Ki-67/DNA multiparameter assay

Harvested cells were fixed in ice-cold 80% ethanol at –20°C for at least 24 h. Next, they were washed in phosphate-buffered saline (PBS) and permeabilized with 0.5% Triton X-100 in PBS for 5 min on ice. After centrifugation, the cells were incubated overnight in the presence of primary antibody against Ki-67 (BD Pharmingen, Franklin Lakes, NJ, USA; diluted in PBS containing 1% bovine serum albumin) and then rinsed and incubated with secondary fluorescein isothiocyanate (FITC)-conjugated antibody (DAKO, Santa Clara, CA, USA; diluted in PBS containing 1% BSA) for 30 min. Cells were then re-suspended in propidium iodide solution (50 μg/mL propidium iodide, 500 μg/mL RNase) and incubated at room temperature for 30 min. Cell fluorescence was measured using a FACSort flow cytometer and Ki-67 level and DNA profile were analyzed using Cellquest software.

**Table 1** Chemical treatment for different groups of HCT116 cells

| Treatment | Con | EGF | 5-FU | EGF + 5-FU |
|---|---|---|---|---|
| EGF (ng/mL) | 0 | 25 | 0 | 25 |
| 5-FU (mg/mL) | 0 | 0 | 0.025 | 0.025 |

### Apoptosis assay

After different treatments, cells were harvested, washed with cold PBS, and then suspended in 100 μL cold annexin V binding buffer, 5 μL annexin V- FITC, and propidium iodide (Jingmei Company, Beijing, China). After the samples were incubated for 15 min at room temperature in the dark, the cells were analyzed on a FACSort flow cytometer. Quadrants were set based on the analysis of single-stained samples. The percentage of apoptotic cells was analyzed with Cellquest software.

### Mouse xenograft model of HCT116 cells and chemical treatment

BALB/c-nu/nu 4-week-old athymic mice (nude mice) were purchased from the Slaccas Company (Shanghai, China). Each mouse was injected subcutaneously with $1 \times 10^6$ HCT116 cells. When the xenograft tumors reached 0.1 $cm^3$ in volume, the mice were randomized into two groups, with six mice in each group. The 5-FU group was administered by subcutaneous injection of saline, intraperitoneal injection of 5-FU at a dose of 1.25 g/kg/day and the EGF + 5-FU group was administered by subcutaneous injection of EGF at a dose of 25 μg/kg/day and intraperitoneal injection of 5-FU at a dose of 1.25 g/kg/day. Health was monitored and tumor size was measured every day using a caliper. Tumor volume was calculated as length × width × width/2.

### Statistical analysis

All statistical analyses were carried out using SPSS 17.0 statistical software (SPSS, Inc., Chicago, IL, USA). All *in vitro* experiments were conducted at least three times. Data were expressed as the mean ± SD. A *P*-value of <

0.05 was considered significant.

## Results

### FACS-sorted CD133+ cells from EGF-treated HCT116 cells showed higher Ki-67 expression and S + G2/M proportion than FACS-sorted CD133+ cells from untreated cells

HCT116 cells were divided into two groups, a control group and EGF group (final concentration of EGF was 25 ng/mL, treated for 24 h). We observed CD133 expression in HCT116 cells (Fig. 1a). Next, the CD133+ cells were sorted by FACS. We found that CD133+ cells in the EGF treated group showed higher Ki-67 expression (Fig. 1b and 1c, $P < 0.05$) and higher S + G2/M (Fig. 1d and 1e, $P < 0.05$) than those in the control group. These results indicate that EGF stimulated the CD133+ CSCs to proliferate by inducing entry into the cell cycle.

### EGF enhanced sensitivity of HCT116 cells to 5-FU *in vitro*

To determine whether EGF can change the chemotherapeutic effect of cytotoxic drugs, we designed the following experiment: four cell groups, a control group, EGF group, 5-FU group, and EGF + 5-FU group, were treated as listed in Table 1. The control group was treated with saline solution rather than EGF or 5-FU. The cells were treated for 24 h or 48 h and then harvested to analyze apoptosis. Apoptosis was analyzed by flow cytometry. After 24 h and 48 h, the apoptosis rate was determined (Fig. 2a and 2b, $P < 0.05$). These results demonstrate that EGF can increase the chemosensitivity of HCT116 cell to the cytotoxic drug 5-FU.

### EGF enhanced sensitivity of HCT116 cells to 5-FU *in vivo*

We next assessed the effect of EGF on chemotherapy *in vivo* in a mouse xenograft model. The 5-FU group was administered subcutaneous injection of saline and intraperitoneal injection of 5-FU at a dose of 1.25 g/kg/day; the EGF + 5-FU group was administered subcutaneous injection of EGF at a dose of 25 μg/kg/day and intraperitoneal injection of 5-FU at a dose of 1.25 g/kg/day. Tumor size was measured every day. The growth curve showed that in the EGF + 5-FU group, the tumor grew more slowly than in the 5-FU group (Fig. 3); there was significant difference between the groups ($P < 0.05$). However, in both groups, the tumors continued growing and growth did not slow as expected.

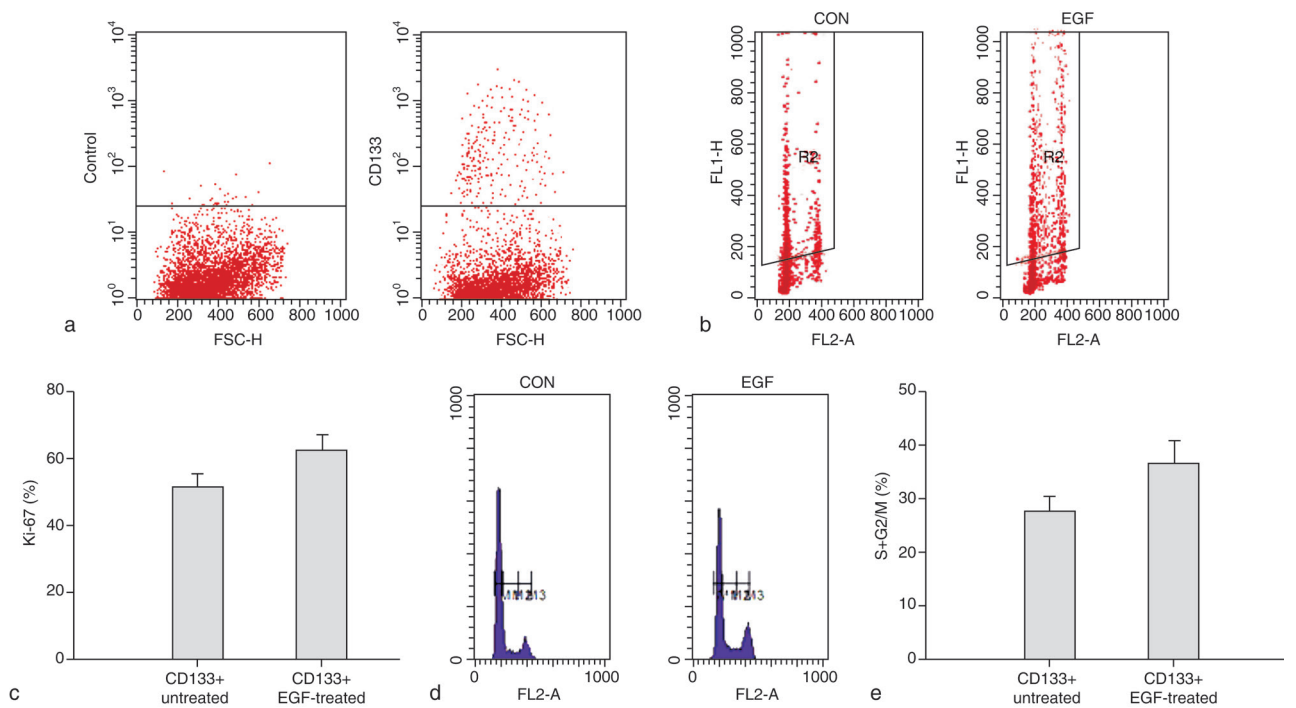


**Fig. 1** Comparison of Ki-67 expression and S + G2/M proportion between FACS sorted CD133+ cells from EGF treated HCT116 cells and untreated HCT116 cells. (a) Flow cytometric analysis of CD133 expression in HCT116 cells. The left was negative control. (b and c) CD133+ cells sorted from EGF treated group showed higher Ki-67 expression than the group not treated by EGF ($P < 0.05$). (d and e) CD133+ cells sorted from EGF treated group showed higher S + G2/M proportion than the group not treated by EGF ($P < 0.05$). Data were presented as mean ± SD.

## Discussion

Recurrence and metastasis are important issues in tumor treatment. The CSC theory states that CSCs have self-renewal capacity and undergo pluripotent differentiation into multiple cell types. Such cells are thought to persist in tumors as a distinct population and cause relapse and metastasis by giving rise to new tumors [2–3]. Therefore, the development of specific therapies targeted at CSCs shows promise for improving the survival and quality of life of patients with cancer. Despite developments in molecularly targeted therapies, cytotoxic chemotherapy remains one of the mainstays of cancer treatment. Many studies have shown that CSCs are chemoresistant. Current cancer therapies are designed to target highly proliferating tumor cells. The determination of tumor shrinkage concomitant with the mean disease-free survival of patients is commonly used as an indicator of treatment efficacy. While such strategies eliminate the visible portion of the tumor, namely the tumor mass, they mostly fail to eliminate the unseen root of cancer, namely CSCs, which possess an inherent resistance towards cytotoxic compounds and radiation and thus are capable of surviving therapy [5–8]. Therefore, it is necessary to develop new strategies to eliminate CSCs [14–16]. Ishikawa *et al* [13] demonstrated that the bone marrow endosteal region is enriched for quiescent human AML LSCs and *in vivo* cytokine treatment induces their entry into the cell cycle. Using an *in vivo* treatment strategy in a NOD/SCID/IL2rynull human AML xenotransplantation model, significantly enhanced elimination of human primary AML LSCs was achieved through *in vivo* cell cycle modification [13]. Studies of hematopoietic stem cells (HSCs) enabled evaluation of LSCs, which resemble normal HSCs in their ability to engraft, produce progeny long-term, and self-renew *in vivo* [17–19]. However, few studies have examined CSCs in solid tumors. It was recently reported that inhibition of Cdk2 kinase activity selectively targets the CD44+/CD24–/low stem-like subpopulation and restores the chemosensitivity of SUM149PT triple-negative breast cancer cells [20]. Because Cdk2 is an important kinase in cell cycle regulation, we evaluated whether changing the cell cycle status of cancer stem cells increased the chemosensitivity of the population.

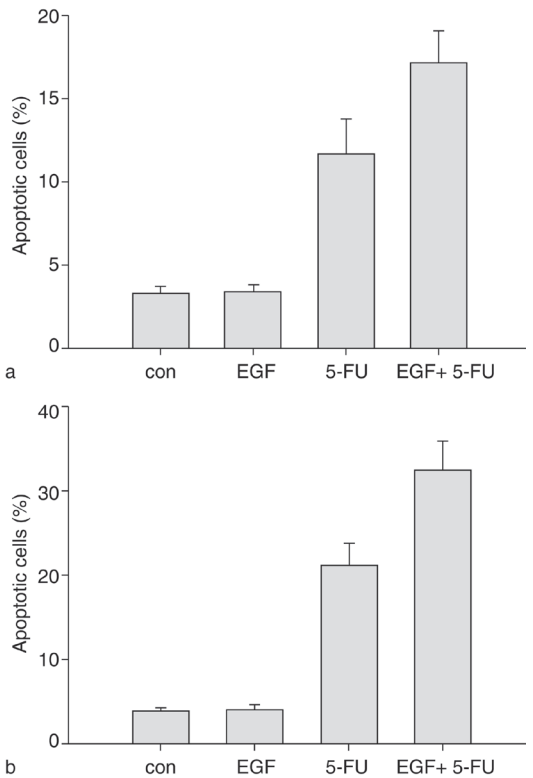


**Fig. 2** Analysis of chemical treatments induced apoptosis of HCT116 cells *in vitro*. Apoptosis were detected by flowcytometry. (a) After 24 hours, apoptosis rate was 11.67% ± 2.11% in 5-FU group versus 17.15% ± 1.89% in EGF + 5-FU group ($P < 0.05$). (b) After 48 hours, apoptosis rate was 20.97% ± 2.69% in 5-FU group, versus 32.42% ± 3.36% in EGF + 5-FU group ($P < 0.05$). Data were presented as mean ± SD.

Experiments confirmed that CD133 could be used as a CSC marker for prostate, lung, melanoma, and liver cancer, as well as other tumors [21–25]. O'Brien *et al* [26] isolated CD133+ cells from specimens of colorectal cancer, inoculated different concentrations of CD133+ cells into NOD/SCID mice under the renal capsule, detected tumors of CD133+ cells with the ability to self-renew and differentiate, and created heterogeneous tumor cell populations. Ricci-Vitani [27] also found enrichment of CD133+ cells in colon CSCs. In a serum-free medium, CD133+ cells, which stayed in the form of undifferentiated tumor balls for 1 year, retained tumorigenic ability, while CD133– cells did not. CD133 expression in tumor cells

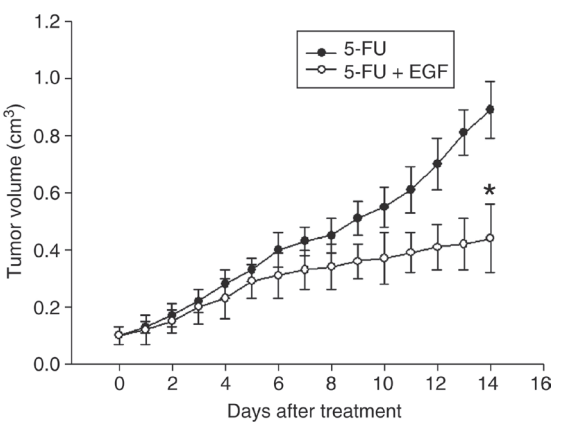


**Fig. 3** EGF enhanced sensitivity of HCT116 cells to 5-FU *in vivo*. Tumor size was measured every day. The growth curve showed that in EGF + 5-FU group, the tumor grew more slowly than 5-FU group. Error bars correspond to mean ± SD (*: $P < 0.05$).

significantly impacts the malignant progression of colon cancer and thus patient survival and tumor recurrence [28]. Thus, CD133 can be used to identify colorectal CSCs. In our study, we used CD133 as a colorectal CSC marker. Because EGF stimulates cell proliferation [29], we used this molecule to induce cells to enter the cell cycle. We found that CD133+ cells in the EGF-treated group showed higher Ki-67 expression than in the control group, as well as a higher proportion of cells in S + G2/M. The results indicated that EGF stimulated CD133+ CSCs to proliferate, thus inducing the cells to enter the cell cycle. The apoptosis rate of cancer cells increased *in vitro* and the tumor volume of xenografts decreased *in vivo* in the EGF + 5-FU group compared to that in the 5-FU alone group. These results clearly demonstrate that the chemotherapeutic effect was enhanced. In conclusion, EGF can enhance tumor sensitivity to chemotherapeutic drugs, likely by promoting tumor stem cells to enter the cell cycle. However, the specific and detailed mechanisms will be examined in our future studies.

### Conflicts of interest

The authors indicated no potential conflicts of interest.

## References


1. Ailles LE, Weissman IL. Cancer stem cells in solid tumors. Curr Opin Biotechnol, 2007, 18: 460–466.
2. Pece S, Tosoni D, Confalonieri S, *et al*. Biological and molecular heterogeneity of breast cancers correlates with their cancer stem cell content. Cell, 2010, 140: 62–73.
3. Jordan CT. Cancer stem cells: controversial or just misunderstood? Cell Stem Cell, 2009, 4: 203–205.
4. Horst D, Kriegl L, Engel J, *et al*. CD133 expression is an independent prognostic marker for low survival in colorectal cancer. Br J Cancer, 2008, 99: 1285–1289.
5. Nagler C, Zänker KS, Dittmar T. Cell fusion, drug resistance and recurrence CSCs. Adv Exp Med Biol, 2011, 714: 173–182.
6. Rich JN, Bao S. Chemotherapy and cancer stem cells. Cell Stem Cell, 2007, 1: 353–355.
7. Kiuchi S, Ikeshita S, Miyatake Y, *et al*. Pancreatic cancer cells express CD44 variant 9 and multidrug resistance protein 1 during mitosis. Exp Mol Pathol, 2015, 98: 41–46.
8. Merlos-Suárez A, Barriga FM, Jung P, *et al*. The intestinal stem cell signature identifies colorectal cancer stem cells and predicts disease relapse. Cell Stem Cell, 2011, 8: 511–524.
9. Chen MS, Woodward WA, Behbod F, *et al*. Wnt/beta-catenin mediates radiation resistance of Sca1+ progenitors in an immortalized mammary gland cell line. J Cell Sci, 2007, 120: 468–477.
10. Costello RT, Mallet F, Gaugler B, *et al*. Human acute myeloid leukemia CD34+/CD38– progenitor cells have decreased sensitivity to chemotherapy and Fas-induced apoptosis, reduced immunogenicity, and impaired dendritic cell transformation capacities. Cancer Res, 2000, 60: 4403–4411.
11. Campos B, Gal Z, Baader A, *et al*. Aberrant self-renewal and quiescence contribute to the aggressiveness of glioblastoma. J Pathol, 2014, 234: 23–33.
12. Holyoake T, Jiang X, Eaves C, *et al*. Isolation of a highly quiescent subpopulation of primitive leukemic cells in chronic myeloid leukemia. Blood, 1999, 94: 2056–2064.
13. Saito Y, Uchida N, Tanaka S, *et al*. Induction of cell cycle entry eliminates human leukemia stem cells in a mouse model of AML. Nat Biotechnol, 2010, 28: 275–280.
14. Gupta R, Vyas P, Enver T. Molecular targeting of cancer stem cells. Cell Stem Cell, 2009, 5: 125–126.
15. Pal A, Valdez KE, Carletti MZ, *et al*. Targeting the perpetrator: breast cancer stem cell therapeutics. Curr Drug Targets, 2010, 11: 1147–1156.
16. Allegra A, Alonci A, Penna G, *et al*. The cancer stem cell hypothesis: a guide to potential molecular targets. Cancer Invest, 2014, 32: 470–495.
17. Warr MR, Pietras EM, Passegué E. Mechanisms controlling hematopoietic stem cell functions during normal hematopoiesis and hematological malignancies. Wiley Interdiscip Rev Syst Biol Med, 2011, 3: 681–701.
18. Jordan CT. Unique molecular and cellular features of acute myelogenous leukemia stem cells. Leukemia, 2002, 16: 559–562.
19. Krause A, Luciana M, Krause F, *et al*. Targeting the acute myeloid leukemia stem cells. Anticancer Agents Med Chem, 2010, 10: 104–110.
20. Opyrchal M, Salisbury JL, Iankov I, *et al*. Inhibition of Cdk2 kinase activity selectively targets the CD44+/CD24–/Low stem-like subpopulation and restores chemosensitivity of SUM149PT triple-negative breast cancer cells. Int J Oncol, 2014, 45: 1193–1199.
21. Collins AT, Berry PA, Hyde C, *et al*. Prospective identification of tumorigenic prostate cancer stem cells. Cancer Res, 2005, 65: 10946–10951.
22. Tang DG, Patrawala L, Calhoun T, *et al*. Prostate cancer stem/progenitor cells: identification, characterization, and implications. Mol Carcinog, 2007, 46: 1–14.
23. Eramo A, Lotti F, Sette G, *et al*. Identification and expansion of the tumorigenic lung cancer stem cell population. Cell Death Differ, 2008, 15: 504–514.
24. Monzani E, Facchetti F, Galmozzi E, *et al*. Melanoma contains CD133 and ABCG2 positive cells with enhanced tumourigenic potential. Eur J Cancer, 2007, 43: 935–946.
25. Suetsugu A, Nagaki M, Aoki H, *et al*. Characterization of CD133+ hepatocellular carcinoma cells as cancer stem/progenitor cells. Biochem Biophys Res Commun, 2006, 351: 820–824.
26. O'Brien CA, Pollett A, Gallinger S, *et al*. A human colon cancer cell capable of initiating tumour growth in immunodeficient mice. Nature, 2007, 445: 106–110.
27. Ricci-Vitiani L, Lombardi DG, Pilozzi E, *et al*. Identification and expansion of human colon-cancer-initiating cells. Nature, 2007, 445: 111–115.
28. Abdelbary EH, Rashed HE, Ismail EI, *et al*. Prognostic value of cancer stem cell markers CD133, ALDH1 and nuclear β-catenin in colon cancer. Chinese-German J Clin Oncol, 2014, 13: 379–385.
29. Santiskulvong C, Sinnett-Smith J, Rozengurt E. EGF receptor function is required in late G(1) for cell cycle progression induced by bombesin and bradykinin. Am J Physiol Cell Physiol, 2001, 281: C886–C898.


**DOI 10.1007/s10330-015-0093-3**
**Cite this article as:** Zou Y, Li XL, Tao DD, *et al*. Epidermal growth factor enhances chemosensitivity of colon cancer by inducing cancer stem cells to enter the cell cycle. Oncol Transl Med, 2017, 3: 86–90.

# Oncology and Translational Medicine

## Aims & Scope

***Oncology and Translational Medicine*** is an international professional academic periodical. The Journal is designed to report progress in research and the latest findings in domestic and international oncology and translational medicine, to facilitate international academic exchanges, and to promote research in oncology and translational medicine as well as levels of service in clinical practice. The entire journal is published in English for a domestic and international readership.

## Copyright



## Supervised by

Ministry of Education of the People's Republic of China.

## Administered by

Tongji Medical College, Huazhong University of Science and Technology.

## Submission information

Manuscripts should be submitted to:
**http://otm.tjh.com.cn**
**dmedizin@sina.com**

## Subscription information

ISSN edition: 2095-9621
CN: 42-1865/R

■ Subscription rates
Subscription may begin at any time. Remittances made by check, draft or express money order should be made payable to this journal. The price for 2017 is as follows: US $ 30 per issue; RMB ￥28.00 per issue.

## Database

***Oncology and Translational Medicine*** is abstracted and indexed in EMBASE, Index Copernicus, Chinese Science and Technology Paper Citation Database (CSTPCD), Chinese Core Journals Database, Chinese Journal Full-text Database (CJFD), Wanfang Data; Weipu Data; Chinese Academic Journal Comprehensive Evaluation Database.

## Business correspondence

All matters relating to orders, subscriptions, back issues, offprints, advertisement booking and general enquiries should be addressed to the editorial office.

***Mailing address***
Editorial office of
*Oncology and Translational Medicine*
Tongji Hospital
Tongji Medical College
Huazhong University of Science and Technology
Jie Fang Da Dao 1095
430030 Wuhan, China
Tel.: +86-27-83662630
Fax: +86-27-83662645
Email: dmedizin@tjh.tjmu.edu.cn

**Printer**
Changjiang Spatial Information Technology Engineering Co., Ltd. (Wuhan)
Hangce Information Cartorgraphy Printing Filial, Wuhan, China
Printed in People's Republic of China

## Managing director



## Executive editors

# Call For Papers
# Oncology and Translational Medicine

(CN 42-1865/R, ISSN 2095-9621)

Dear Authors,

*Oncology and Translational Medicine* (OTM), a peer-reviewed open-access journal, is very interested in your study. If you have unpublished papers in hand and have the idea of making our journal a vehicle for your research interests, please feel free to submit your manuscripts to us via the Paper Submission System.

Aims & Scope

- Lung Cancer
- Liver Cancer
- Pancreatic Cancer
- Gastrointestinal Tumors
- Breast Cancer
- Thyroid Cancer
- Bone Tumors
- Genitourinary Tumors
- Brain Tumor
- Blood Diseases
- Gynecologic Oncology
- ENT Tumors
- Skin Cancer
- Cancer Translational Medicine
- Cancer Imageology
- Cancer Chemotherapy
- Radiotherapy
- Tumors Psychology
- Other Tumor-related Contents

Contact Us
Editorial office of Oncology and Translational Medicine
Tongji Hospital
Tongji Medical College
Huazhong University of Science and Technology
Jie Fang Da Dao 1095
430030 Wuhan, China
Tel.: 86-27-83662630
Email: dmedizin@tjh.tjmu.edu.cn;
dmedizin@sina.com

*Oncology and Translational Medicine* (OTM) is sponsored by Tongji Hospital, Tongji Medical College, Huazhong University of Science and Technology, China (English, bimonthly).

OTM mainly publishes original and review articles on oncology and translational medicine. We are working with the commitment to bring the highest quality research to the widest possible audience and share the research work in a timely fashion.

Manuscripts considered for publication include regular scientific papers, original research, brief reports and case reports. Review articles, commentaries and letters are welcome.

About Us

- Peer-reviewed
- Rapid publication
- Online first
- Open access
- Both print and online versions

For more information about us, please visit:
http://otm.tjh.com.cn